E.O. Paton Electric Welding Institute of the National Academy of Science of Ukraine
International Association “Welding”

The Paton Welding Journal

09
2025

International Scientific-Technical and Production Journal ♦ Founded in January 2000 (12 Issues Per Year)

Address of Editorial Office:
E.O. Paton Electric Welding Institute, 11 Kazymyr Malevych Str., 03150, Kyiv, Ukraine
E-mail: office@paton.kiev.ua; https://paton.org.ua/en/

Address of Publisher:
International Association “Welding”, 11 Kazymyr Malevych Str., 03150, Kyiv, Ukraine
Tel.: (38044) 205 23 90, E-mail: patonpublishinghouse@gmail.com; journal@paton.kiev.ua
https://patonpublishinghouse.com/eng/journals/tpwj

The Journal was registered by the National Council of Ukraine on Television and Radio Broadcasting on 09.05.2024, carrier identifier R30-04569
ISSN 0957-798X (Print), ISSN 3041-2293 (Online)
DOI: https://doi.org/10.37434/tpwj, from #01, 2020 to now; DOI: https: //doi.org/10.15407/tpwj from #01, 2014 to #12, 2019.

Subscriptions, 12 issues per year:
348 Euro — annual subscription for the printed (hard copy) version, air postage and packaging included;
288 Euro — annual subscription for the electronic version (sending issues in pdf format or providing access to IP addresses).

Representative Offices of “The Paton Welding Journal”:

BRAZIL, Arc Dynamics
Address: Nova Iguacu, Rio de Janeiro, Brazil
Daniel Adolpho, Tel.: +55 21 9 6419 5703,
E-mail: dadolpho@arcdynamics.com.br

CHINA, China-Ukraine Institute of Welding, Guangdong Academy of Sciences
Address: Room 210, No. 363 Changxing Road, Tianhe, Guangzhou, 510650, China
Zhang Yupeng, Tel.: +86-20-61086791,
E-mail: patonjournal@gwi.gd.cn

BULGARIA, Bulgarian Welding Society
Address: Blvd. Asen Yordanov No.10, Sofia 1592, Bulgaria
Pavel Popgeorgiev, Tel.: +359 899 96 22 20,
E-mail: office@bws-bg.org

POLAND, PATON EUROPE Sp. z o. o.
Address: ul. Kapitałowa 4, 35-213, Rzeszów, Poland
Anton Stepakhno, Tel.: +38067 509 95 67,
E-mail: Anton.Stepakhno@paton.ua

The content of the Journal includes articles received from authors from around the world in the field of welding, cutting, cladding, soldering, brazing, coating, 3D additive technologies, electrometallurgy, material science, NDT and selectively includes translations into English of articles from the following journals, published in Ukrainian:

- «Avtomatychne Zvaryuvannya» (Automatic Welding), https://patonpublishinghouse.com/eng/journals/as;
- «Suchasna Elektrometalurhiya» (Electrometallurgy Today), https://patonpublishinghouse.com/eng/journals/sem;
- «Tekhnichna Diahnostyka ta Neruinivnyi Kontrol» (Technical Diagnostics & Nondestructive Testing), https://patonpublishinghouse.com/eng/journals/tdnk.

CONTENTS

ORIGINAL ARTICLES

*Translated Article(s) from “Avtomatychne Zvaryuvannya” (Automatic Welding), No. 4, 2025.

**Translated Article(s) from “Suchasna Elektrometalurhiya” (Electrometallurgy Today), No. 3, 2025.

Indexing: The electronic edition of the Journal is stored in the V.I. Vernadsky National Library of Ukraine (eVerLib), included in the OPEN UKRAINIAN CITATION INDEX database and international databases: CROSSREF, EBSCO, Google Scholar, INDEX COPERNICUS, ULRICHSWEB.

DOI: https://doi.org/10.37434/tpwj2025.09.01

NARROW GAP WELDING OF PT-3V TITANIUM ALLOY WITH A CONTROLLED MAGNETIC FIELD

S.V. Akhonin, V.Yu. Bilous, R.V. Selin, I.K. Petrichenko, L.M. Radchenko, S.B. Rukhansky

E.O. Paton Electric Welding Institute of the NASU
11 Kazymyr Malevych Str., 03150, Kyiv, Ukraine

ABSTRACT

Tungsten inert gas (TIG) narrow-gap welding of titanium alloys is a cost-effective and efficient method for joining thick titanium alloy structures. The technology of narrow-gap welding of titanium alloys with a magnetically-controlled arc enables a wide range of welding parameter adjustments. This study considers the application of narrow-gap welding with a tungsten electrode and a controlled magnetic field for producing joints of PT-3V titanium alloy plates with thicknesses of 45 and 64 mm. The strength of the welded joints of PT-3V titanium alloy produced by narrow-gap welding with a controlled magnetic field reaches 636 MPa, which is 85 % of the base metal strength, and it is comparable to the properties of welded joints made using the conventional gas tungsten arc welding technology. Application of the obtained results allowed welding joints of titanium alloys with variable thicknesses ranging from 45 to 65 mm while maintaining the same number of passes.

KEYWORDS: narrow-gap welding, titanium, titanium alloy, TIG welding, tungsten electrode, controlled magnetic field, heat input, structure, microstructure, mechanical properties, metallography

INTRODUCTION

Narrow-gap welding is an economical and effective way to join thick metal [1, 2]. Reducing the consumption of filler wire, inert gas, and other welding consumables, as well as the labour intensity of preparing the edges of the parts to be welded, are factors that are particularly important when welding titanium and titanium-based alloys [3]. A well-known method of welding titanium is the Gas Tungsten Arc Narrow-Gap Welding (GTAW-NG) using a magnetically-controlled arc, developed at the E.O. Paton Electric Welding Institute of the NAS of Ukraine [4]. This welding method has the following advantages: small width of the produced weld and small volume of the deposited metal. Another advantage is the simple shape of the edges to be welded.

As is known, GTAW-NG can be performed within a wide range of welding current values, welding speeds, and filler wire feed rates [5, 6]. At the same time, it is possible to deposit a metal layer with a thickness from 3 to 8 mm or more in a single pass. The increased thickness of the metal layer deposited in a single pass allows reducing the number of passes required to fill the gap, which in turn improves the efficiency of the welding process. However, the main condition when choosing a welding mode for titanium alloys is producing a defect-free joint [7, 8]. An excessive increase in the thickness of the metal layer deposited in a single pass can cause defects in the weld [9, 10]. A characteristic defect of multilayer narrow-gap welding of titanium alloys is the lack of fusion between the weld metal and the base metal, as well as interlayer lacks of fusion in the weld [11, 12].

The technology of narrow-gap welding of titanium alloys with a magnetically-controlled arc allows changing not only the heat input of the welding process [13–15], but also the parameters of the controlled magnetic field, such as the magnetic induction in the arc zone and the reversal frequency of the controlled magnetic field [16].

Thus, it is advisable to conduct research to determine the influence of such parameters of the process of narrow-gap welding of titanium alloys with a magnetically-controlled arc, such as the magnitude of the magnetic induction of the controlled magnetic field, as well as the value of the heat input, on the properties of welded joints of PT-3V titanium alloy.

THE AIM

of the work is to investigate the influence of the induction value of the controlled magnetic field and the heat input value of the narrow-gap welding process with a tungsten electrode of PT-3V titanium alloy on the structure and mechanical properties of welded joints.

MATERIALS USED IN THE STUDY

To achieve the set aim, multilayer welding was performed on specimens of 45 and 65 mm thick, made of PT-3V titanium alloy in accordance with GOST 1050–88. The length of the test specimens for welding was 600 mm.

A 3 mm titanium filler wire diameter of 2V grade, recommended for PT-3V titanium alloy, was used as an additive. Welding was performed with application of external controlled magnetic field to deviate the

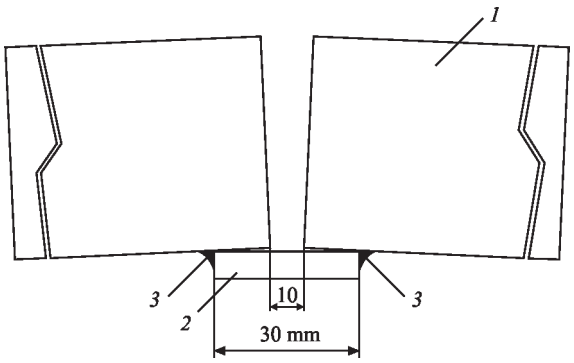

Figure 1. Scheme of assembling specimens for welding: *1* — side walls of a narrow gap; *2* — remaining backing plate; *3* — welds for welding-on the backing plate to the side walls

arc. The work used EVI-2 tungsten electrodes with a diameter of 5 mm. Welding was performed at direct current with straight polarity. A VDU-501 welding current source was used. The welding current was selected within the range of 420–480 A, and the arc voltage was maintained at 12 V by an automatic arc voltage control system. The feed rate of the 2V filler wire of 3 mm diameter into the weld pool varied between 64 and 82 m/h.

The parts were assembled for welding using a remaining backing plate, which was manually welded-on to the back side of the part [17] (Figure 1). This backing plate serves as the bottom wall of a narrow gap when performing the first pass. After completing the root pass, filling passes were performed. To weld a butt with a thickness of 65 mm, 13 passes are required, i.e., a 5 mm thick layer of metal is deposited when welding using the existing technology. If the thickness of the metal layer deposited in a single pass is increased, the overall efficiency of the welded joint production process will be improved.

The scheme of multilayer welding process is shown in Figure 2. Welding is performed with a tungsten electrode that is lowered into a narrow gap. At the same time, the filler wire is fed perpendicular to the electrode into the head part of the weld pool. The controlled magnetic field is created by a special

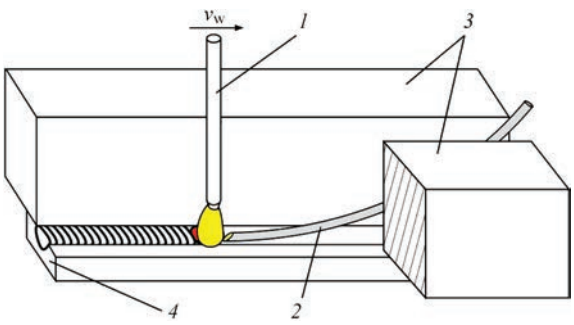

Figure 2. Scheme of the process of multilayer narrow-gap welding with a tungsten electrode: *1* — tungsten electrode; *2* — filler wire; *3* — plates to be welded; *4* — remaining welded-on backing plate

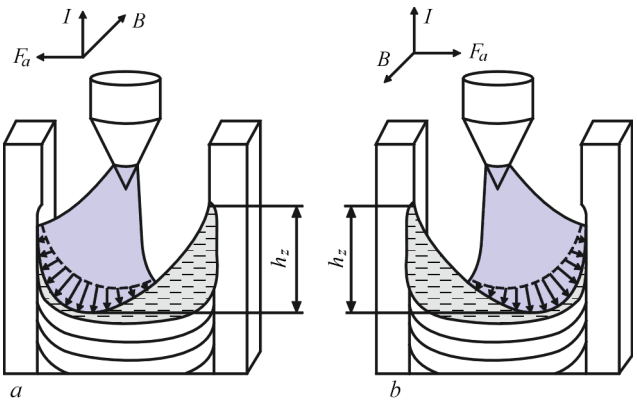

Figure 3. Scheme of melting the side walls of a narrow gap and location of the welding arc: *a*, *b* — extreme positions; h_z — height of the weld metal layer being deposited

electromagnet with a narrow core located in a narrow gap [17]. As a result of the interaction of the magnetic field with the arc current, a Lorentz force arises, which deviates the arc and causes displacement of the anode spot to the side wall.

The scheme of melting the side walls of a narrow gap during narrow-gap welding with a tungsten electrode with an external controlled magnetic field is shown in Figure 3. The value of the anode spot displacement to the side wall is proportional to the magnetic induction value of the controlled magnetic field. From the presented scheme, it can be concluded that in order to ensure guaranteed fusion of the weld metal layer with a height h_z with the side wall, it is necessary to deviate the welding arc so that the anode spot rises along the side wall to the corresponding height h_z and melts the metal.

Welding modes with different values of heat input and magnetic induction of the controlled magnetic field, which ensure high-quality formation of the deposited bead surface and the absence of lacks of fusion of the deposited metal of the weld with the side walls of welded joints of PT-3V titanium alloy are given in Table 1. Macrosections of welded joints are shown in Figure 4.

Welding according to parameters of modes No. 1 and No. 3 ensures high-quality formation of the deposited bead surface of the PT-3V titanium alloy specimen. Moreover, GTAW-NG with a controlled magnetic field and the highest feed rate of the filler wire at 82 m/h (mode No. 3, Table 1) provides the highest height of the deposited metal layer of 7 mm thick in a single pass. It should be noted that when the feed rate of the filler wire grows without increasing the magnetic induction values of the controlled magnetic field at mode No. 2, the formation of lacks of fusion is observed in the weld metal. In order to improve the efficiency of a single pass and deposit a 7 mm thick layer of metal in a single pass, it is necessary to reduce the welding speed and increase the welding current to 480 A. This corresponds to mode No. 2 (Table 1),

Table 1. Modes of narrow-gap welding with a tungsten electrode of PT-3V titanium alloy with an external controlled magnetic field

Mode number	Welding speed V_w, m/h	Induction of the controlled magnetic field, mT	Welding current I_w, A	Heat input (total), kJ/m	Filler wire feed rate, m/h
1	8	8	420	2268	64
2	5	8	480	4147	64
3	8	11	450	2430	82

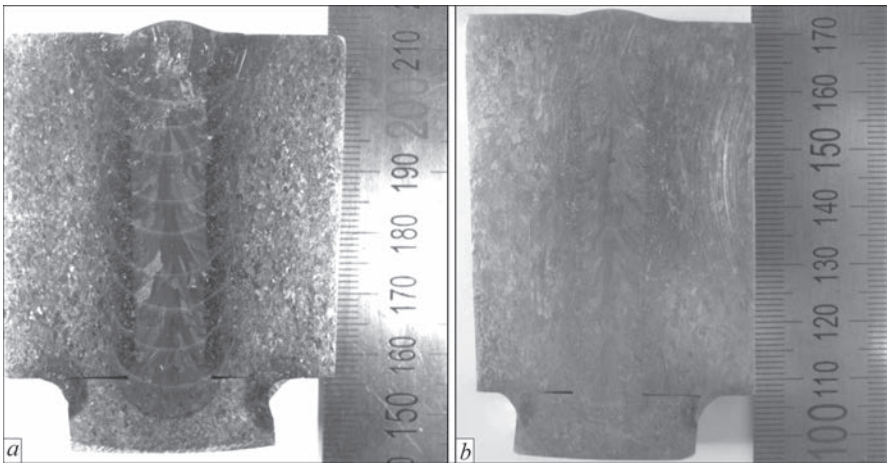

Figure 4. Cross-macrosections of welded joints of PT-3V titanium alloy made by GTAW-NG with a controlled magnetic field: *a* — welded joint of 45 mm thickness, mode No. 1; *b* — welded joint of 65 mm thickness, mode No. 3

which is characterized by a high heat input of the welding process (4147 kJ/m).

If the magnetic induction value of the controlled magnetic field is increased from 8 to 11 mT, the height of the anode spot displacement to the side wall of the narrow gap and the height of the weld metal layer being deposited h_z grows (see Figure 4). In this case, it is possible to increase the feed rate of the filler wire and deposit a 7 mm thick metal layer probably without reducing the welding speed and with a slight increase in the heat input of the welding process, mode No. 3 (Table 1).

STUDY OF THE MICROSTRUCTURE OF WELDED JOINTS OF PT-3V TITANIUM ALLOY PRODUCED BY GTAW-NG WITH A CONTROLLED MAGNETIC FIELD

PT-3V titanium alloy and filler welding wire of 2 V grade belong to the group of pseudo-α alloys. PT-3V alloy contains, by wt.%: Fe — up to 0.25; C — up to 0.1; Si — up to 0.12; V — 1.2–2.5; N — up to 0.04; Ti — 91.39–95; Al — 3.5–5.0; Zr — up to 0.3; O — up to 0.15; N — up to 0.006, other impurities — 0.3. At GTAW-NG with a controlled magnetic field, no more than 10 % of the base metal enters the weld metal [4].

The microstructure of the base metal of the PT-3V alloy is shown in Figure 5. The structure of the base metal consists of equilibrium primary β-grains of various sizes, framed by a continuous or intermittent α-phase band (Figure 5, *a*) of up to 15 μm thick. The intragranular structure consists of lamellar α-phase (Figure 5, *b*) of up to 1.5 μm thick (Figure 5, *b*). A small amount of β-phase may be present in the spaces between the α-plates, which is not always detectable under an optical microscope.

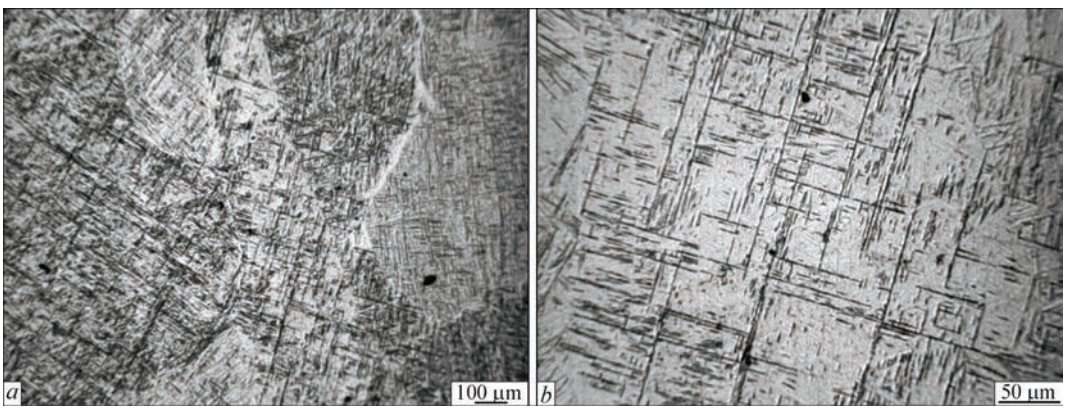

Figure 5. Microstructure of the base metal of PT-3V titanium alloy

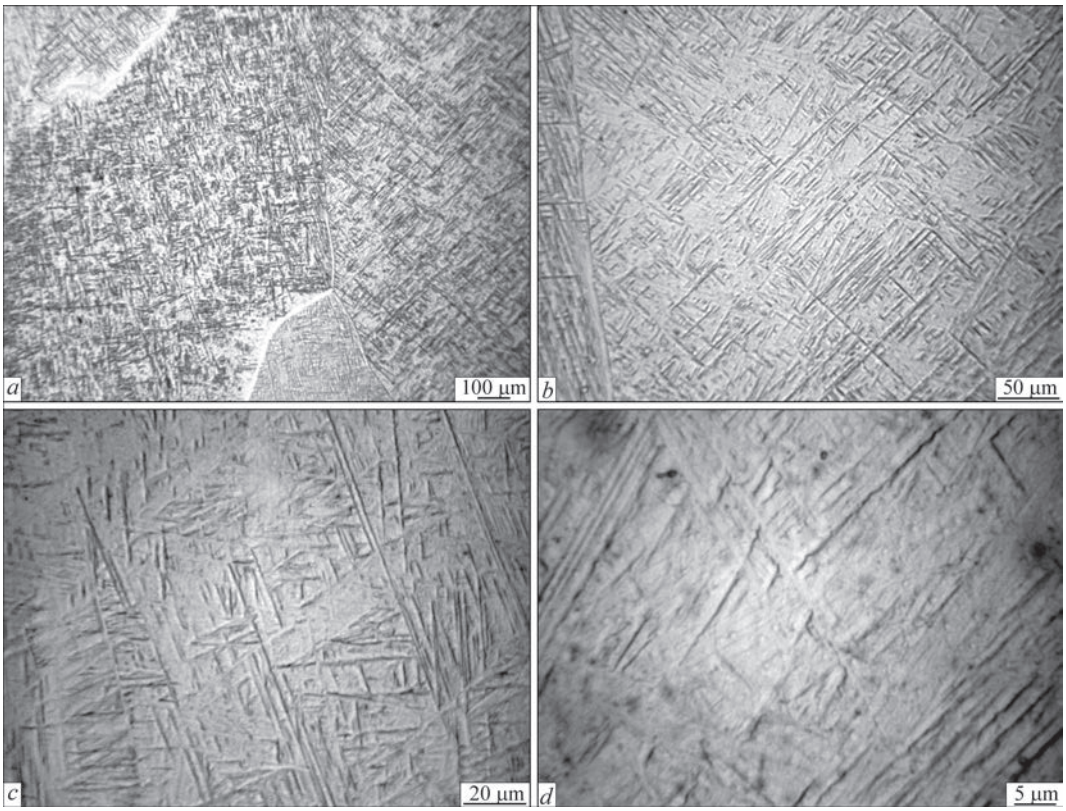

Figure 6. Microstructure of the weld metal of PT-3V titanium alloy made by GTAW-NG with a controlled magnetic field

The microstructure of the PT-3V alloy weld metal produced by GTAW-NG at mode No. 3 in its middle part is shown in Figure 6. Equilibrium and elongated primary grains of various sizes are formed in the weld metal. Despite the differences in the configuration and size of the primary grains, the intragranular microstructure of the weld metal produced by GTAW-NG using 2V wire (Figure 6, *a*, *b*) of the lamellar type is very similar to the microstructure of the base metal. The microstructures of the weld metal produced at modes Nos 1 and 2 are similar (Figure 6, *d*).

The microstructure of the PT-3V alloy weld metal produced by GTAW-NG at mode No. 3 in the fusion zone is shown in Figure 7. In the fusion zone, the formation of fine primary grains is observed (Figure 7, *a*), while the intragranular structure is similar to that of the base metal (Figure 7, *b*).

The microstructure of the metal in the heat-affected zone (HAZ) immediately behind the fusion zone, namely the coarse-grain region of the PT-3V alloy produced by GTAW-NG at mode No. 3, is shown in Figure 8. The metal in this zone consists of equilibrium primary grains (Figure 8, *a*) with a microstructure similar to the internal microstructure in the grain volume of the weld metal (Figure 8, *b*, *c*). In Figure 8, *d*, the distribution of dispersed particles of the second phase, most probably the β-phase, along the boundaries of the α-plates can be observed. The sizes of such particles are 0.5 μm and less (Figure 8, *d*).

The microstructure of the HAZ metal near the base metal of the PT-3V alloy, produced by GTAW-NG at mode No. 3, is shown in Figure 9. The microstructure of the HAZ metal near the base metal (Figure 9, *a*, *b*) is also very similar to other areas of the welded joint

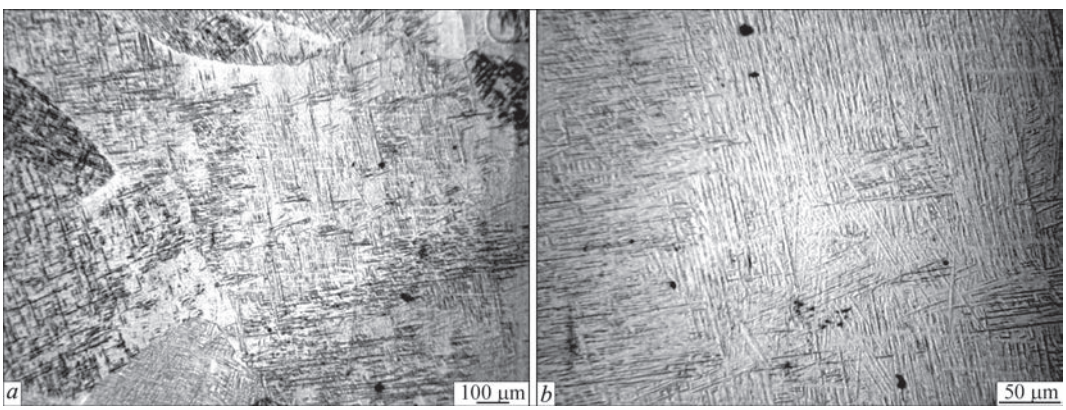

Figure 7. Microstructure of the fusion zone metal of PT-3V titanium alloy produced by GTAW-NG with a controlled magnetic field

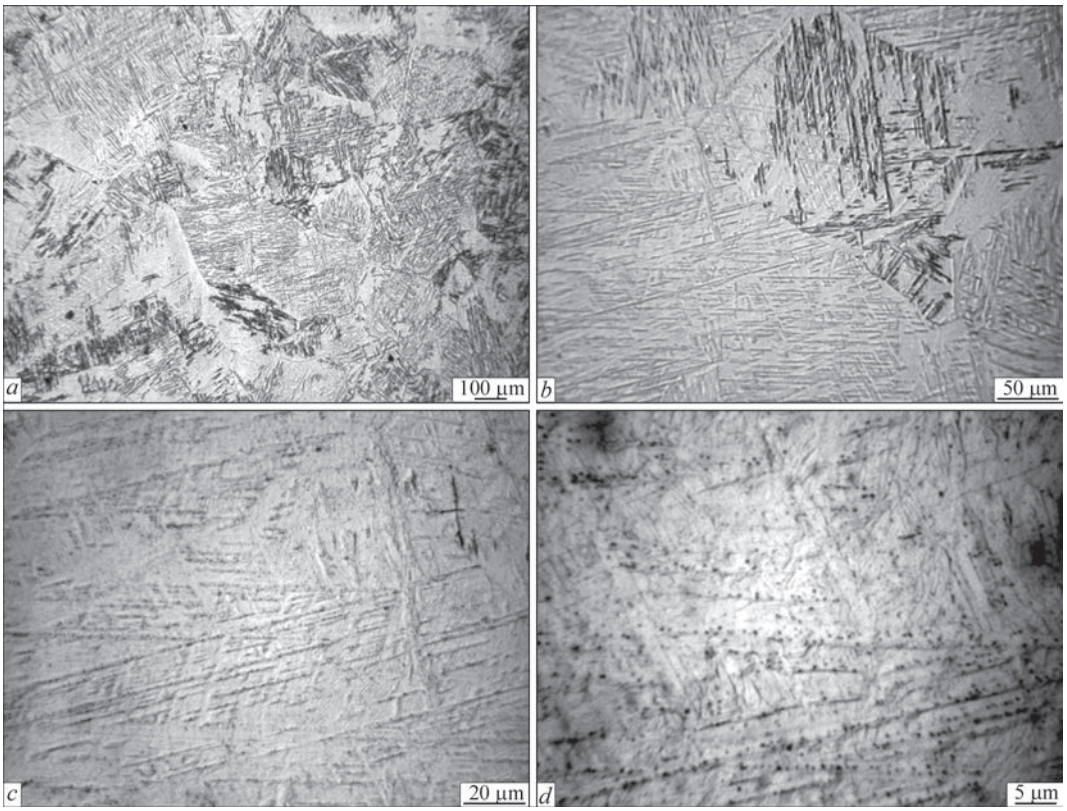

Figure 8. Microstructure of the HAZ metal of PT-3V alloy, produced by GTAW-NG with a controlled magnetic field

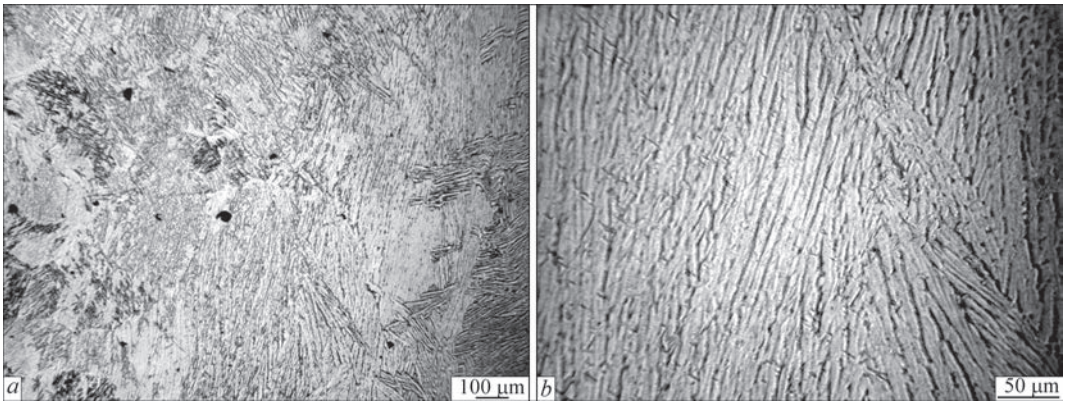

Figure 9. Microstructure of the HAZ metal near the base metal of PT-3V alloy, produced by GTAW-NG with a controlled magnetic field

of the PT-3V alloy, produced by GTAW-NG using 2V filler wire.

Thus, the microstructure of the metal in the welds produced at modes Nos 1, 2, and 3 is similar. The microstructure of the HAZ metal produced at modes Nos 1, 2, and 3 is also similar. However, the dimensions of the HAZ of joints produced at mode No. 2 (Table 2) are the largest, which is associated with the highest value of the heat input of the welding process at mode No. 2.

DISCUSSION OF RESULTS

The determination of the mechanical properties of welded joints of PT-3V titanium pseudo-α alloy, produced by GTAW-NG with an external controlled magnetic field, allowed concluding that the lowest strength values in the post-weld state at a level of 617 MPa are found in joints made at mode No. 2, with values of welding heat input of 4147 kJ/m (Table 3), which is 82 % of the strength of the base metal. The highest strength values in the post-weld state at a level of 643 MPa were found in welded joints

Table 2. Dimensions of the weld and HAZ of welded joints of PT-3V titanium alloy made by narrow-gap welding with a tungsten electrode under an external controlled magnetic field

Mode number	Height of the layer deposited in a single pass, mm	Weld width, mm	HAZ width, mm
1	5	11.6	2.85
2	7.1	12.4	4.95
3	7.0	11.5	2.75

Table 3. Mechanical properties of the base metal and welded joints of PT-3V titanium alloy, produced by GTAW-NG with an external controlled magnetic field*

Specimen type, mode No.	σ_t, MPa	$\sigma_{0.2}$, MPa	δ, %	ψ, %	*KCV*, J/cm^2	
					Weld	HAZ
Base metal of PT-3V δ = 65 mm	746.6	677.5	12.7	30.8	95.3	
Welded joint, mode No. 1	643.2	603.5	12.7	41.2	107.4	77.9
Welded joint, mode No. 2	617.4	559.7	9.0	38.7	112.2	77.7
Welded joint, mode No. 3	636.5	583.4	14.0	46.2	104.7	79.0

*2V filler wire.

made at mode No. 1, with the lowest values of welding heat input of 2268 kJ/m (Table 3), which is 86 % of the strength of the base metal. The strength values of welded joints made at mode No. 3 with the highest values of magnetic induction of the controlled magnetic field (11 mT, see Table 1) are at a level of 636 MPa, which is 85 % of the strength of the base metal. The mechanical properties of welded joints made at modes Nos 1 and 3 are similar. To find the reasons for the decrease in the strength of welded joints made at modes No. 2 with the highest values of welding heat input and weld and HAZ sizes, additional studies of the microstructure of welded joints are necessary [17, 18].

The impact toughness values of specimens with a sharp notch in the weld metal for welded joints made at modes Nos 1, 2, and 3 exceed the impact toughness values for the base metal. This is associated with a lower content of alloying elements in the weld metal, which consists of 90 % filler metal of 2V welding wire. The impact toughness values of the HAZ for welded joints made at modes Nos 1, 2, and 3 are lower than the impact toughness values for the base metal.

Thus, it was found that it is possible to increase the thickness of the weld metal layer deposited in a single pass from 5 to 7 mm and to increase the overall efficiency of the welding process in a narrow gap of PT-3V titanium alloy by increasing the magnetic induction of the controlled magnetic field to 11 mT. This made it possible to ensure reliable melting of the side walls of the narrow gap and produce a high-quality welded joint. The mechanical properties of welded joints made at a mode with magnetic induction values of the controlled magnetic field of 11 mT are similar to the properties of welded joints made using the existing argon arc welding technology.

The application of the obtained results made it possible to propose a technology for welding PT-3V titanium alloy of variable thickness, namely of 45–65 mm thick, with the same number of passes.

CONCLUSIONS

1. The parameters of the GTAW-NG mode with an external controlled magnetic field of PT-3V titanium alloy were determined, allowing a 7 mm thick layer of metal to be deposited in a narrow gap of 10 mm wide in a single pass.

2. The strength of welded joints made of PT-3V alloy, produced by GTAW-NG with 2V filler wire at a magnetic induction values of the controlled magnetic field of 11 mT, is 636 MPa or 85 % of the strength of the base metal and is similar to the properties of welded joints made using the existing argon arc welding technology.

3. The microstructure of the metal in the welds and HAZ of PT-3V alloy, produced by GTAW-NG using 2V filler wire at modes with elevated magnetic field induction of the controlled magnetic field values, is similar to the microstructure of the metal in welds produced using existing argon arc welding technology.

4. The application of the obtained results made it possible to propose a technology for welding PT-3V titanium alloy of variable thickness, namely 45–65 mm thick, using the same number of passes.

REFERENCES

1. Hori, K., Haneda, M. (1999) Narrow gap arc welding. *J. of JWS*, **3**, 41–62.
2. Dak, G., Khanna, N., Pandey, C. (2023) Study on narrow gap welding of martensitic grade P92 and austenitic grade AISI 304L SS steel for ultra-supercritical power plant application. *Archiv. Civ. Mech. Eng*., 23(**14**). DOI: https://doi.org/10.1007/s43452-022-00540-3
3. Luo, Y., Zhang, Z.L., Zhou, C.F. et al. (2017) Effect of narrow groove MAG welding oscillation parameters on weld formation. *J. Hebei Univ. Sci. Technol*., 38(**1**), 7–12. DOI: https://doi.org/10.7535/hbkd.2017yx01002
4. Akhonin, S.V., Belous, V.Yu., Romanyuk, V.S. et al. (2010) Narrow-gap welding of up to 110 mm thick high-strength titanium alloys. *The Paton Welding J.*, **5**, 34–37.
5. Jae-Ho Jun, Sung-Ryul Kim, Sang-Myung Cho (2016) A study on productivity improvement in narrow gap TIG welding. *J. of Welding and Joining*, 34(**1**), 68–74. DOI: https://doi.org/10.5781/JWJ.2016.34.1.68
6. Nguyen, D.H. (2014) *Research on droplet transfer and welding process of oscillation arc narrow gap GMAW*: Master's Thesis, Harbin Institute of Technology, Harbin, China.
7. Sun, Qing Jie, Hai Feng Hu, Xin Yuan, Ji Cai Feng (2011) Research status and development trend of narrow-gap TIG welding. *Advanced Materials Research*, **308**, 1170–1176. DOI: https://doi.org/10.4028/www.scientific.net/AMR.308-310.1170
8. Dong, Z., Tian, Y., Zhang, L. et al. (2024) Research status of high efficiency deep penetration welding of medium-thick

plate titanium alloy: A review. *Defence Technology*, **45**, 178–202. DOI: https://doi.org/10.1016/j.dt.2024.08.004
9. Fang, D.S. (2017) *Study on the characteristics of three-wire indirect arc and its thick-wall narrow gap welding process under gas protection*: Ph.D. Thesis, Dalian University of Technology, Dalian, China.
10. Belous, V.Yu., Akhonin, S.V. (2011) Formation of narrow-gap welded joints on titanium using the controlling magnetic field. *The Paton Welding J.*, **4**, 19–22.
11. Shoichi, M., Yukio, M., Koki, T. et al. (2013) Study on the application for electromagnetic controlled molten pool welding process in overhead and flat position welding. *Sci. Technol. Weld. Join.*, **18**, 38–44. DOI: https://doi.org/10.1179/1362171812Y.0000000070
12. Ding, L., Qin, B., Ge, K. et al. (2023) Microstructures and mechanical properties of thick Ti–6Al–3Nb–2Zr–1Mo joint by magnetron-controlled narrow gap TIG welding. *Metals and Materials Inter.*, 29(**8**), 2304–2315. DOI: http://dx.doi.org/10.1007/s12540-022-01367-6
13. Wang, J., Sun, Q., Feng, J. et al. (2017) Characteristics of welding and arc pressure in TIG narrow gap welding using novel magnetic arc oscillation. *The Inter. J. of Advanced Manufacturing Technology*, **90**, 413–420. DOI: https://doi.org/10.1007/s00170-016-9407-5
14. Wan, L., Huang, Y., Lv, S. et al. (2016) Narrow-gap tungsten inert gas welding of 78-mm-thick Ti–6Al–4V alloy. *Materials Sci. and Technology*, 32(**15**), 1545–1552. DOI: https://doi.org/10.1080/02670836.2015.1131941
15. Fang, N., Guo, E., Huang, R. et al. (2021) Effect of welding heat input on microstructure and properties of TC4 titanium alloy ultra-narrow gap welded joint by laser welding with filler wire. *Materials Research Express*, 8(**1**), 016511. DOI: http://dx.doi.org/10.1088/2053-1591/abd4b3
16. Xinyu Bao Yonglin Ma, Shuqing Xing, Yongzhen Liu, Weiwei Shi (2022) Effects of pulsed magnetic field melt treatment on grain refinement of Al–Si–Mg–Cu–Ni alloy direct-chill casting billet. *Metals,* 12(**7**), 1080. DOI: https://doi.org/10.3390/met12071080
17. Akhonin, S.V., Bilous, V.Yu., Selin, R.V. et al. (2023) Narrow-gap TIG welding of thick steel 20. *The Paton Welding J.*, **6**, 18–23. DOI: https://doi.org/10.37434/tpwj2023.06.03
18. Yujun Hu, Hongjin Zhao, Xuede Yu et al. (2022) Research progress of magnetic field regulated mechanical property of solid metal materials. *Metals,* **12**, 1988. DOI: https://doi.org/10.3390/met12111988

ORCID
S.V. Akhonin: 0000-0002-7746-2946,
V.Yu. Bilous: 0000-0002-0082-8030,
R.V. Selin: 0000-0002-2990-1131,
I.K. Petrichenko: 0000-0002-0476-3983,
L.M. Radchenko: 0009-0008-1097-7137,
S.B. Rukhansky: 0009-0002-1260-3688

CONFLICT OF INTEREST
The Authors declare no conflict of interest

CORRESPONDING AUTHOR
V.Yu. Bilous
E.O. Paton Electric Welding Institute of the NASU
11 Kazymyr Malevych Str., 03150, Kyiv, Ukraine.
E-mail: belousvy@gmail.com

SUGGESTED CITATION
S.V. Akhonin, V.Yu. Bilous, R.V. Selin, I.K. Petrichenko, L.M. Radchenko, S.B. Rukhansky (2025) Narrow gap welding of PT-3V titanium alloy with a controlled magnetic field. *The Paton Welding J.*, **9**, 3–9.
DOI: https://doi.org/10.37434/tpwj2025.09.01

JOURNAL HOME PAGE
https://patonpublishinghouse.com/eng/journals/tpwj

Received: 25.02.2025
Received in revised form: 04.04.2025
Accepted: 15.09.2025

DOI: https://doi.org/10.37434/tpwj2025.09.02

MATHEMATICAL MODELLING OF THERMAL PROCESSES IN FRICTION STIR WELDING OF LIGHT ALLOYS BASED ON MAGNESIUM

O.O. Makhnenko, O.S. Kostenevych, O.V. Makhnenko

E.O. Paton Electric Welding Institute of the NASU
11 Kazymyr Malevych Str., 03150, Kyiv, Ukraine

ABSTRACT

Mathematical modelling of thermal processes in welding is one of the effective methods for predicting the quality of a welded joint depending on technological parameters. However, to develop an adequate mathematical model, it is necessary to take into account a number of factors that can significantly affect the accuracy of the results of the computational analysis. Using the example of the problem of mathematical modelling of temperature distributions in friction stir welding (FSW) of a butt joint of plates of magnesium MA2-1 (AZ31) alloy of different thicknesses (2 and 8 mm), a computational study of the distribution of maximum temperatures and thermal cycles at points at different distances from the welded joint axis was carried out. It was found that the results of mathematical modelling of heat conductivity processes during welding heating in FSW are influenced by several aspects. One of the significant among them is heat dissipation into the working tool and fixing tools. Also, to ensure the accuracy of calculation of temperature distributions during FSW, it is important to choose the optimal sizes of the butt joint model in order to avoid the effect of heat accumulation in a model of a limited size, and to take into account the dependence of the friction coefficient on the temperature of the material, since its value determines the power of heat generation in FSW. Based on the results obtained, recommendations are formulated for conducting mathematical modelling of thermal processes in FSW of light alloys.

KEYWORDS: friction stir welding, temperature distributions, thermal cycles, heat dissipation, work tool, backing plate, mathematical modelling, finite element analysis

INTRODUCTION

Today, mathematical modelling of various physical processes is becoming a powerful tool in the development of new technologies for the manufacture and treatment of materials, including welding and related technologies. The procedure for mathematical modelling of temperature distributions, mechanical properties, and the stress-strain state of welded joints is regulated by the acting ISO standard [1], which formulates in sufficient detail the requirements for the preparation of input data, model development, model verification and validation, calculations, analysis, and presentation of modelling results. Although the acting standard concerns computer modelling of arc welding processes, the requirements formulated there can be effectively used for other welding processes, such as friction stir welding (FSW).

The adequacy of the mathematical finite element model and the accuracy of the results obtained from the analysis of thermal processes (temperature distributions) during FSW of magnesium alloy plates depend not only on the heating source model and the choice of finite element mesh size, but also on a number of other factors, such as: taking into account heat dissipation into the working tool and fixing tools (clamps, backing plate), the overall sizes of a welded joint specimen model, variations in the thermophysical properties of the base material, etc. It is clear that these factors can significantly affect the reliability of the results obtained from the finite element analysis, but determining the extent of their impact on the accuracy of the results of temperature distributions and thermal cycles during FSW is usually beyond the scope of the results presented in the articles or is not carried out at all. Taking into account heat dissipation into the working tool and fixing tools in the finite element model of a welded joint during FSW is found in a limited number of works [2–4]. Researchers mostly use a simplified heating source model without modelling the working tool or do not take into account heat dissipation into the fixing elements [3–6].

WITH THE AIM

of studying the impact of the above factors on the nature and magnitude of the distribution of maximum temperatures during FSW of light alloys, as well as on the parameters of thermal cycles in points at different distances from the welded joint axis, a computational study was carried out using the example of a mathematical modelling problem for temperature distributions during FSW of a butt joint of MA2-1 (AZ31) magnesium alloy plates of different thicknesses (2 and 8 mm) using FSW. Based on the results obtained, recommendations were formulated for math-

ematical modelling of thermal processes during FSW of light alloys.

MATHEMATICAL MODEL OF TEMPERATURE PROCESSES DURING FSW

For mathematical modelling of residual stresses during FSW of aluminium alloy, a previously developed model [7] was used, which was supplemented by taking into account heat dissipation into the working tool and backing plate.

Heat conductivity equation in the presence of bulk heat dissipation with a power of $W(x, y, z, t)$, W/m^3:

$$c\rho\frac{\partial T}{\partial t}=\frac{\partial}{\partial x}\left(\lambda\frac{\partial T}{\partial x}\right)+\frac{\partial}{\partial y}\left(\lambda\frac{\partial T}{\partial y}\right)+ +\frac{\partial}{\partial z}\left(\lambda\frac{\partial T}{\partial z}\right)+W(x,y,z,t), \quad (1)$$

where T is the temperature, °C; c is the specific heat capacity, J/kg·°C; ρ is the material density, kg/m^3; λ is the thermal conductivity coefficient, W/(m·°C).

A distinctive feature of the developed FSW heating source model is heat generation due to friction between the tool and the joint material. The tool rotates around a vertical axis at a certain angular velocity ω, rpm/s, and is pressed against the plates with an axial force P_n, Pa, which causes a heat flow into the joint material at the contact surface of the tool (Figure 1):

$$\lambda\frac{\partial T}{\partial n}=\mu\cdot P_n\cdot\omega\cdot r, \quad (2)$$

where μ is the coefficient of friction; $r=\sqrt{(x-x_0-v_w t)^2+(y-y_0)^2}$ is the distance of the considered contact point from the axis of rotation of the working tool ($x_0+ v_w t, y_0$); v_w is the linear velocity of the tool.

Then, the heat dissipation power Q, W, on the corresponding contact surfaces with an area S (Figure 1) is:

$$Q=\mu\cdot P_n\cdot\omega\cdot\pi\cdot\iint_s r dS, \quad (3)$$

arm ($z = \delta$, $R_1 < r < R_2$)

$$Q_1=\frac{2\pi}{3}\mu\cdot P_n\cdot\omega\cdot(R_2^3-R_1^3),$$

side surface of the pin ($\delta - h < z < \delta$, $r = R_1$)

$$Q_2=2\pi\cdot\mu\cdot P_n\cdot\omega\cdot R_1^2\cdot h,$$

lower end surface of the pin ($z = \delta - h$, $0 > r > R_1$)

$$Q_3=\frac{2\pi}{3}\cdot\mu\cdot P_n\cdot\omega\cdot R_1^3,$$

δ is the thickness of the plates being welded, m; h is the length of the pin entering the material, m.

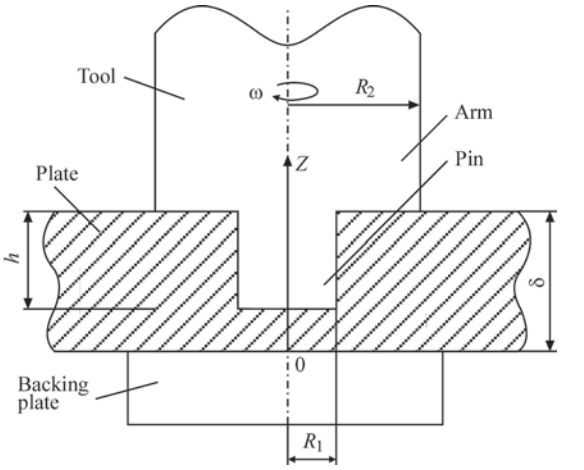

Figure 1. Schematic diagram of the working tool in FSW

In order to simplify the model, the bulk heat dissipation power $W(x, y, z, t)$, W/m^3, can be modelled from two components. The first one is related to heat dissipation in volume V_1 on the upper surface of the joint plates under the tool arm ($\delta - dz < z < \delta$, $R_1 < r < R_2$); dz is the size of the finite element, and the second one is in the volume of the pin V_2 ($\delta - h < z < \delta$, $0 > r > R_1$):

$$W(x,y,z,t)=W_1+W_2,$$

$$W_1=\frac{Q_1}{V_1}=\frac{\frac{2\pi}{3}\mu P_n\omega(R_2^3-R_1^3)}{\pi(R_2^2-R_1^2)dz}= =\frac{2\mu P_n\omega(R_2^2+R_2R_1+R_1^2)}{3(R_2+R_1)dz}, \quad (4)$$

$$W_2=\frac{Q_2+Q_3}{V_2}=\frac{2\pi\mu P_n\omega R_1^2h+\frac{2\pi}{3}\mu P_n\omega R_1^3}{\pi R_1^2h}= =2\mu P_n\omega\left(1+\frac{R_1}{3h}\right).$$

The boundary conditions on the contact surfaces between the elements of the joint and the working tool, as well as with the backing plate due to contact heat dissipation, were set in the form (Figure 2):

$$q_i=\lambda\frac{\partial T(x,y,z,t)}{\partial n}=-k_i(T_i-T), \quad (i=1,2) \quad (5)$$

where q_i is the heat flow at the contact surface of the tool and the welded joint ($i = 1$) and on the contact surface of the welded joint and backing plate ($i = 2$); T_i is the surface temperature of the tool or backing plate, respectively; k_i is the contact heat dissipation coefficient, W/(m^2·°C).

The boundary conditions on the surfaces of the elements of the joint and the working tool, taking into account the convective heat exchange with the environment, were defined as follows:

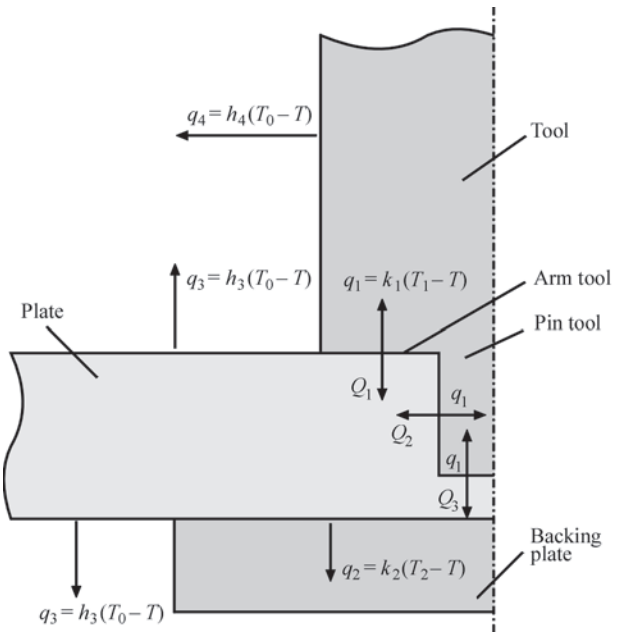

Figure 2. Schematic diagram of heat flows in FSW

$$q_i = \lambda \frac{\partial T(x,y,z,t)}{\partial n} = -h_i(T_0 - T) \quad (i = 3,4) \qquad (6)$$

where q_i is the heat flow on the surface of the welded joint elements (i = 3) and on the surface of the tool (i = 4); T_0 is the ambient temperature; h_i is the heat dissipation coefficient from the surface during convective heat exchange with the environment (usually, under conditions of natural convection in air T_0 = 20 °C, h = 10–20 W/(m²·°C)).

To perform mathematical modelling of heat dissipation processes during welding heating, data on the thermophysical properties of the base material of the joint depending on temperature are required (Table 1).

The melting temperature range [8, 9] is T_{sol} = 605 °C, T_{liq} = 630 °C, the specific heat of melting Q_{liq} = 357 kJ/kg. The friction coefficient for magnesium alloys is taken at a level μ = 0.3–0.4 [3, 6, 9].

The material of the plate (size is 300×300 mm) is MA2-1 (AZ31) magnesium alloy. The material of the FSW working tool (diameter of the arm in contact with the plate is 10 mm; diameter in the other part of the tool is 20 mm; total height of the tool is 50 mm) is stainless steel. The material of the backing plate (10 mm thick and 150 mm wide) is stainless steel.

Table 1. Thermophysical properties of MA2-1 (AZ31) alloy [8]

T, °C	α·10⁶, 1/°C	λ, W/(m·°C)	c_p, J/(kg·°C)	ρ, kg/м³
20	24.92	102	1008	1785
100	25.56	107	1042	1775
200	26.48	112	1076	1761
300	27.40	118	1109	1746
400	28.32	123	1143	1730
500	29.25	125	1193	1714

Based on the results of experimental studies [10], the technological parameters of the FSW process were set to ensure high-quality formation of a welded joint of plates with a thickness δ = 2 and 8 mm. The angular velocity of the working tool was ω = 1420 rpm, and the linear velocity of the tool was v_w = 133 mm/min.

Based on the experimental thermogram of the welding process recorded by a thermal imager, it was determined that the temperature on the outer surfaces of the welded joint plates and the tool during FSW did not exceed 355 °C. According to the results of mathematical modelling, the temperature in the contact zone between the tool and the plate material will be higher (approximately at a level of 450–600 °C).

For a plate with a thickness of 2 mm, the vertical pressure on the tool is P_n = 28 MPa. If the friction coefficient is taken as μ = 0.4, then the total power of the heating source according to (4) is $W = 1.8 \cdot 10^6$ W/m³. For a plate with a thickness of 8 mm, the vertical pressure on the tool was set higher, namely P_n = 55 MPa. The total power of the heating source is $W = 3.5 \cdot 10^6$ W/m³ to ensure a maximum heating temperature of the material not lower than 450 °C.

To account for heat dissipation in the welded joint model, it was necessary not only to create additional models of the working tool and backing plate, but also to set boundary conditions for heat dissipation and heat exchange with the environment.

The heat dissipation coefficient between the tool and the plate was taken as k_1 = 5000 W/(m²·°C). The heat dissipation coefficient between the plate and the backing plate was assumed to be k_2 = 1000 W/(m²·°C). The convective heat dissipation coefficient from the surface of the tool rotating at high velocity was taken as h_1 = 50 W/(m²·°C), and the convective heat dissipation coefficient from the surface of the plate was taken as h_2 = 20 W/(m²·°C).

The total calculation time for the FSW process is 37 s, of which the first 13 s the working tool rotates to heat the plate material to 450 °C.

The procedure for selecting the size of the finite element mesh for the model for determining the temperature distribution during FSW for plates with a thickness of 2 and 8 mm was carried out, provided that when the size of the finite element is reduced twice, the relative maximum error of the results should not exceed 5 %. From the data presented in Figure 4, it can be concluded that a finite element mesh size of 1 mm is optimal in terms of ensuring the necessary accuracy of results and efficient use of computer resources.

IMPACT OF HEAT DISSIPATION INTO THE WORKING TOOL AND FIXING TOOLS (BACKING PLATE)

Using a developed finite element model (Figures 3, 4), which contains a magnesium alloy plate, a working tool, and a stainless steel backing plate, a numerical study of the heat conductivity problem was performed during the movement of the working tool (heat source) in FSW, taking into account the heat dissipation process into the working tool and backing plate. The nature and values of the distribution of maximum temperatures during FSW of the plates were determined, as well as the parameters of thermal cycles in points at different distances from the welded joint axis (Figure 5).

Figure 6 shows the temperature distribution during FSW of 2 mm thick plates with and without account for heat dissipation into the tool and backing plate. It is seen that when heat dissipation is taken into account, the lower part of the working tool heats up quite strongly (to approximately 300 °C), and the backing plate also heats up, but noticeably less (to approximately 100 °C).

The calculation results based on thermal cycles during FSW in points at some distance from the weld axis $y = 0$; 15 and 30 mm for different variants of ac-

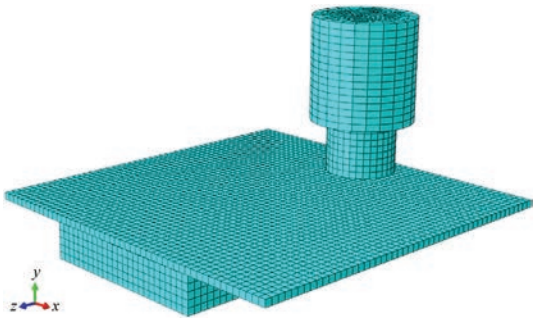

Figure 3. Finite element model of FSW, which includes a working tool, a magnesium alloy plate, and a backing plate

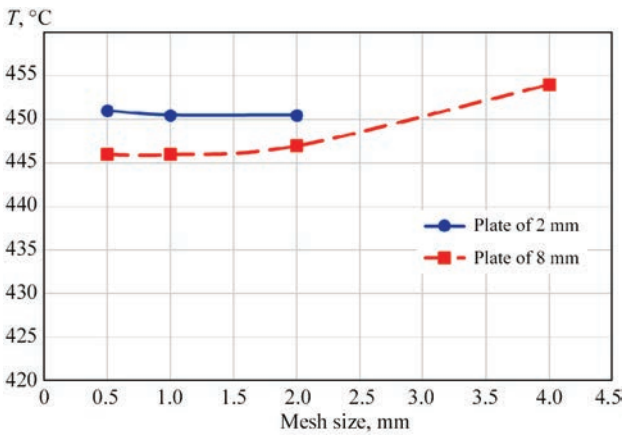

Figure 4. Dependence of the maximum values of temperature distribution in FSW on the size of the finite element mesh for plates with a thickness δ = 2 and 8 mm

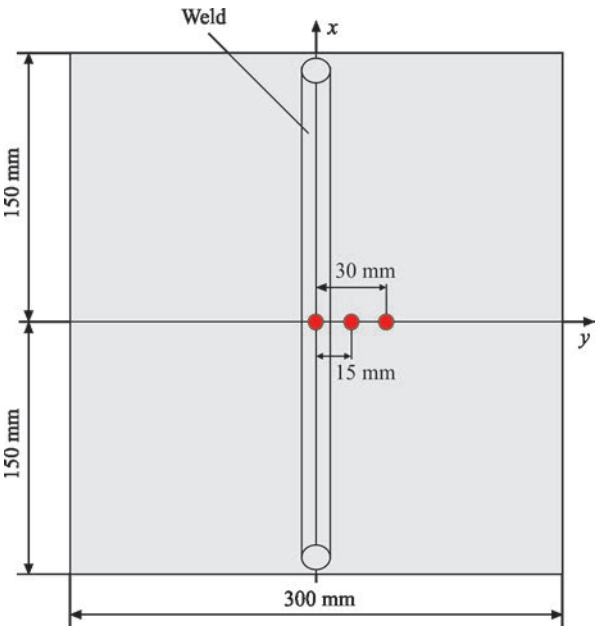

Figure 5. Layout of points on the FSW joint specimen at which thermal cycles were determined

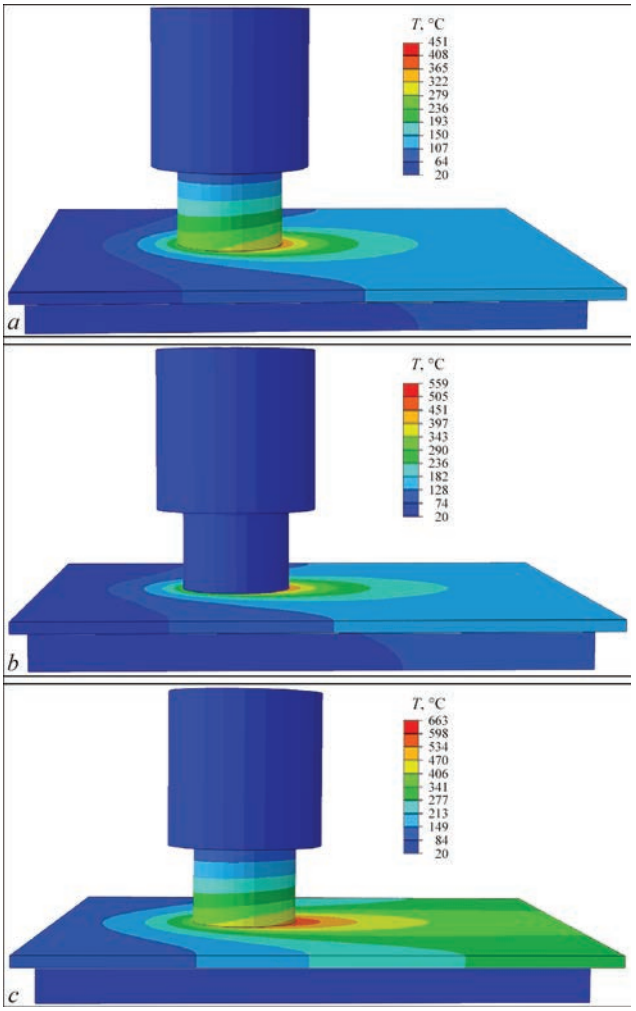

Figure 6. Temperature distribution during FSW of plates with a thickness δ = 2 mm made of MA2-1 magnesium alloy: *a* — with heat dissipation into the tool and backing plate; *b* — without heat dissipation into the tool; *c* — without heat dissipation into the backing plate

Table 2. Maximum calculated temperatures during FSW of MA2-1 magnesium alloy plates depending on heat dissipation into the working tool and backing plate

Plate thickness, mm	Heat dissipation into the tool and backing plate	Without heat dissipation into the tool		Without heat dissipation into the backing plate		Without heat dissipation into the tool and backing plate	
	T_{max}, °C	T_{max}, °C	Relative deviation (error), %	T_{max}, °C	Relative deviation (error), %	T_{max}, °C	Relative deviation (error), %
2	451	559	24	663	47	890	97
8	446	498	12	512	15	540	21

count for heat dissipation showed that this factor is very important and its neglecting can lead to significant errors in the results of temperature kinetics at all stages — heating and cooling.

In the finite element analysis of the heat conductivity problem in FSW of magnesium alloy plates, neglecting of heat dissipation into the working tool and backing plate leads to significant errors (24 and 47 %, respectively) in terms of maximum temperatures for thin plates of 2 mm thick (Table 2, Figure 7, *a*).

In the case of welding thick plates of 8 mm thick, neglecting of heat dissipation into the working tool and backing plate is not so critical and is associated with errors that are 2–3 times smaller (12 and 15 %, respectively) in terms of maximum temperatures (Table 2, Figure 7, *b*). A calculation error of 10–15 % is acceptable, considering the possible discrepancies in the input data for the calculation.

IMPACT OF THE SIZES OF THE WELDED JOINT SPECIMEN MODEL

Another very important aspect of the numerical determination of the kinetics of temperature distributions during welding is the overall sizes (width and length) of a welded joint model, since mathematical modelling requires determining the optimal model sizes to reduce calculation time while maintaining sufficient accuracy of the results.

To determine the impact of variations in the sizes of a welded joint model, a comparison was made for

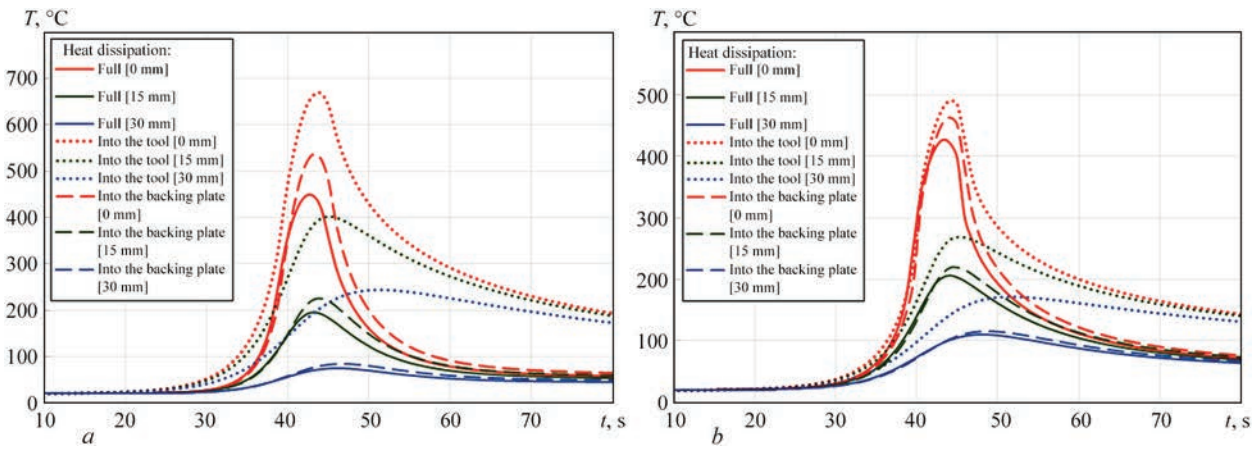

Figure 7. Effect of heat dissipation on thermal cycles during FSW in points at some distance from the weld axis y = 0; 15 and 30 mm (plate size 300×300 mm): *a* — thickness 2; *b* — 8 mm

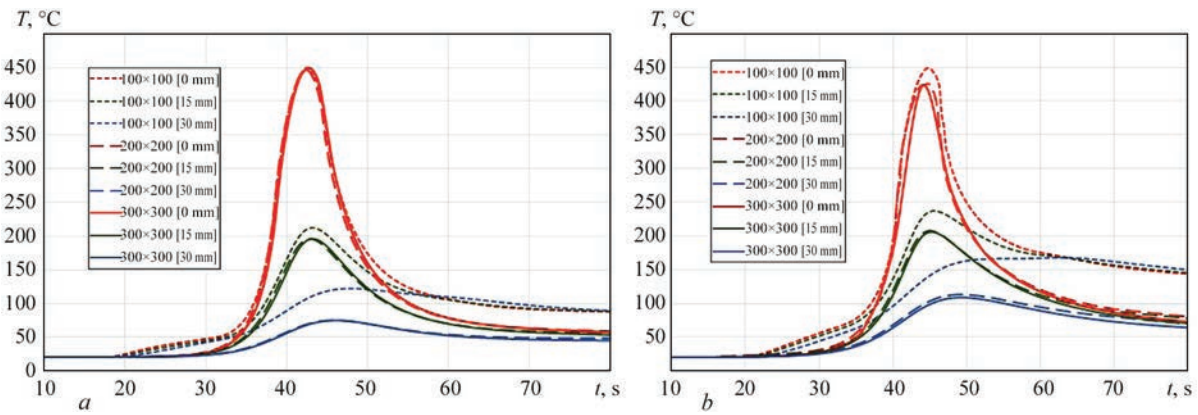

Figure 8. Thermal cycles during FSW in points at some distance from the weld axis y = 0; 15 and 30 mm for plates of different sizes: 100×100, 200×200, 300×300 mm: *a* — thickness 2; *b* — 8 mm

Table 3. Thermophysical properties of MA2-1 (AZ31) alloy [5, 8, 11]

T, °C	λ, W/(m·°C) [5]	c_p, J/(kg·C°) [5]	λ, W/(m·°C) [11]	c_p, J/(kg·°C) [11]	λ, W/(m·°C) [8]	c_p, J/(kg·°C) [8]	ρ, kg/m³ [8]
20	96,4	1050	156	1025	102	1008	1785
100	101	1130	153	1072	107	1042	1775
200	105	1170	151	1118	112	1076	1761
300	109	1210	149	1164	118	1109	1746
400	113	1300	147	1209	123	1143	1730
500	120	1360	146	1255	125	1193	1714

the results of mathematical modelling of heat conductivity processes during welding heating in FSW for three variants of model sizes: 100×100, 200×200, and 300×300 mm. The size of the finite element mesh for all variants was maintained in accordance with the previously selected parameters.

The calculation results based on thermal cycles during FSW in points at some distance from the weld axis y = 0; 15 and 30 mm for plates of different sizes shown in Figure 8 indicated that at a butt joint model size of 100×100 mm, heat accumulation and, accordingly, excessive heating of the entire model occur, which leads to a significant error in the results of the thermal cycle at all its stages — heating and cooling, especially for points located at some distance from the weld axis. This effect is also enhanced for thicker plates (8 mm). The results obtained for model sizes 200×200 and 300×300 mm are very close — the error is at a level of 1–2 %. Thus, for the considered case of FSW parameters, it is possible to use a model with sizes of 200×200 mm. However, in the case of welding with higher values of heating power in FSW, as well as for arc welding, the model size of 300×300 mm is more optimal in terms of ensuring the accuracy of the temperature field results.

IMPACT OF VARIATION OF VALUES IN THE THERMOPHYSICAL PROPERTIES OF THE MATERIAL

As shown by the analysis of literature data, there is a noticeable difference in the values of these properties (Table 3, Figure 9) with regard to data on the thermophysical properties depending on the temperature of the base material of the welded joint of AZ31 (MA2-1) magnesium alloy [5, 8, 11].

To determine the effect of variations in the values of the thermophysical properties of the material, a comparison was made for the results of mathematical modelling of heat dissipation (thermal conductivity) processes during welding heating in FSW for three variants of these properties. Two variants of properties were taken from literature sources specifically for the AZ31 (MA2-1) alloy, and the third variant corresponds to pure Mg, since this chemical element constitutes approximately 95 % of the alloy under consideration.

Figure 10 shows the results of calculating thermal cycles during FSW in points at some distance from the weld axis y = 0; 15 and 30 mm for a 300×300 mm plate and based on different thermophysical properties. It is seen that if the values of the properties differ within 5 %, as for the data [5, 8], then the error of the thermal cycle results does not exceed a few percent. In the case of a significant (from 20 to 50 %) deviation in the thermal conductivity coefficient of pure Mg [11], the results for the maximum temperatures of thermal cycles already have an error of more than 20 %. I.e., the variation in the values of the thermophysical properties of the material can lead to an error in the results of mathematical modelling of heat conductivity processes during welding heating in FSW,

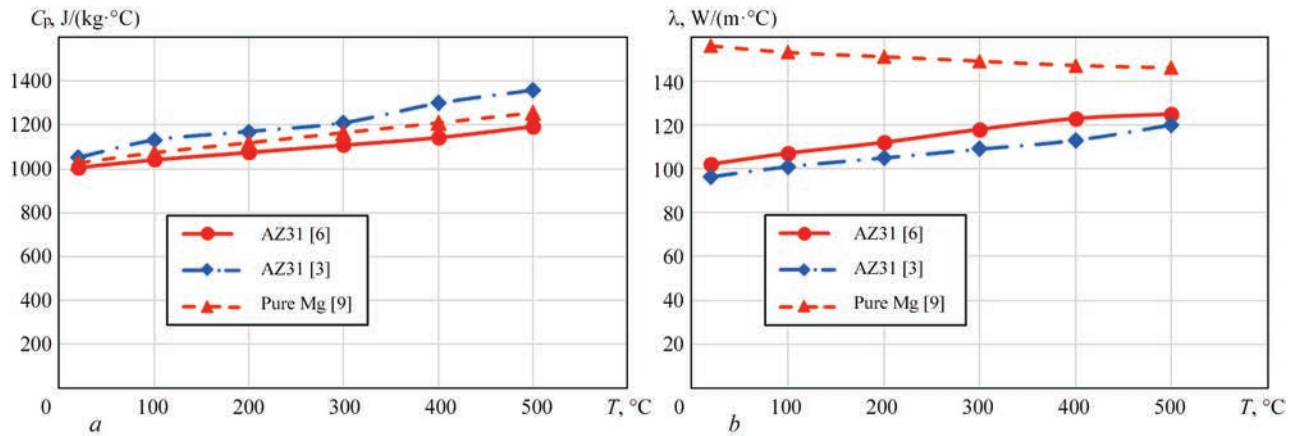

Figure 9. Dependence of the specific heat capacity and thermal conductivity of AZ31 magnesium alloy on temperature according to various data [5, 8, 11]

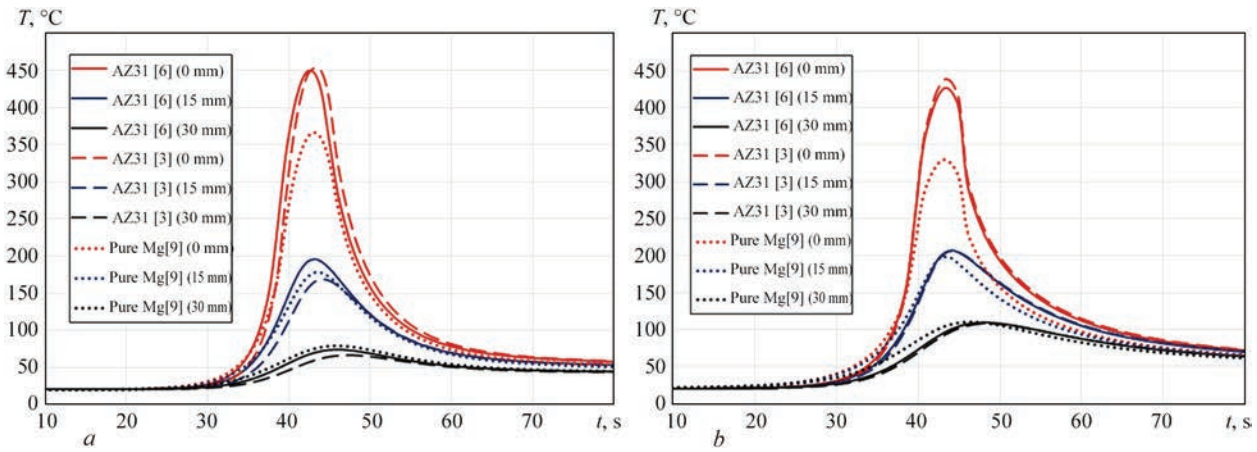

Figure 10. Thermal cycles during FSW in points at some distance from the weld axis y = 0; 15 and 30 mm and according to various data on thermophysical properties (300×300 mm plates): *a* — thickness of 2; *b* — 8 mm

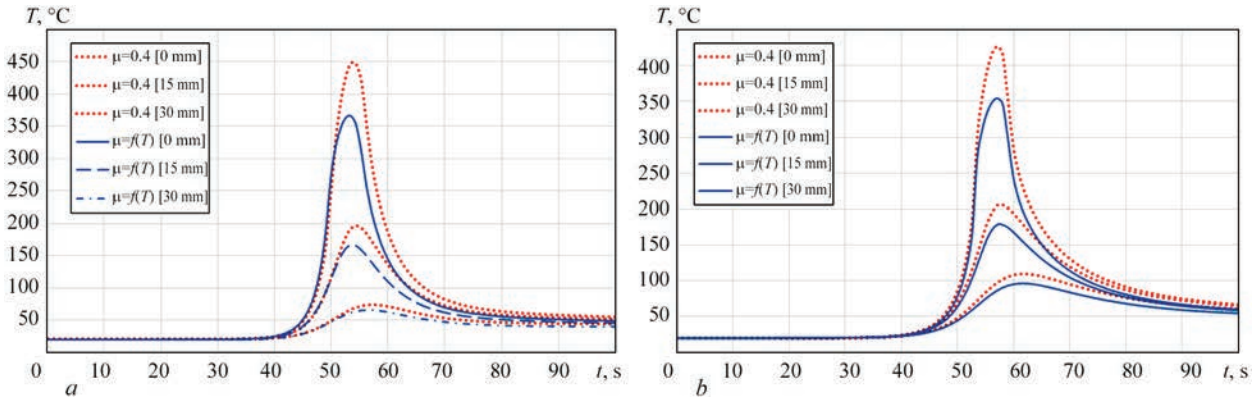

Figure 11. Thermal cycles during FSW in points at some distance from the weld axis *y* = 0; 15 and 30 mm according to various data on the dependence of friction coefficient on temperature (300×300 mm plate): *a* — thickness of 2; *b* — 8 mm

Table 4. Dependence of friction coefficient on temperature [12]

T, °C	μ
20	0.4
100	0.4
200	0.4
250	0.4
300	0.35
400	0.25
500	0.09

but this error corresponds to the deviation in the values of the properties themselves.

The influence of the dependence of friction coefficient on temperature on the results of modelling temperature distributions during FSW of magnesium alloy plates was also investigated. Figure 11 shows the thermal cycles during FSW of plates of 300×300 mm and with a thickness δ = 2 and 8 mm in points at some distance from the weld axis *y* = 0; 15 and 30 mm according to different data on the dependence of the friction coefficient on temperature, namely at a constant value μ = 0.4 and at a dependence of μ = *f*(*T*) (Table 4) [12]. According to the thermal cycles presented in Figure 11, at a constant value of the friction coefficient, higher values of maximum temperatures were obtained.

CONCLUSIONS

1. In finite element analysis of heat conductivity problem during FSW of thin 2 mm thick magnesium alloy plates, neglecting of heat dissipation into the working tool and fixing tools leads to significant errors in the maximum temperature values (above 40 %) and for thick plates with a thickness of 8 mm, this error is no longer so critical (up to 15 %).

2. With a limited size of a butt joint model of 100×100 mm, heat accumulation and excessive heating of the entire model are observed, which leads to a significant error in the results of the thermal cycle at all its stages — heating and cooling, especially for points at some distance from the weld axis. This effect is also enhanced for thicker plates (8 mm). For the considered case of FSW parameters, it is possible to use a model with sizes of 200×200 mm to determine the temperature distributions, but in the case of welding with higher heating power values, a model size of 300×300 mm will be more optimal in terms of ensuring the accuracy of the temperature field results.

3. Variations in the values of thermophysical properties of the material can lead to errors in the results of mathematical modelling of heat conductivity processes during welding heating in FSW, but this error, as a rule, does not exceed the deviation of the properties themselves. The dependence of the friction coefficient on the material temperature is important for ensuring the accuracy of calculating temperature distributions during FSW, since its value determines heat generation power during FSW.

REFERENCES

1. ISO/TS 18166:2016: *Numerical welding simulation — Execution and documentation*.
2. Zhenzhen, Yu, Wei Zhang, Hahn Choo, Zhili Feng (2012) Transient heat and material flow modeling of friction stir processing of magnesium alloy using threaded tool. *Metallurgical and Materials Transact. A*, **43**, 724–737. DOI: https://doi.org/10.1007/s11661-011-0862-1
3. Song, M., Kovacevic, R. (2004) Heat transfer modelling for both workpiece and tool in the friction stir welding process: A coupled model. *Proc. Inst. Mech. Eng., Pt B: J. of Engineering Manufacture*, 218(**1**), 17–33. DOI: https://doi.org/10.1243/095440504772830174
4. Majstrenko, A.L., Nesterenkov, V.M., Dutka, V.A. et al. (2015) Modeling of heat processes for improvement of structure of metals and alloys by friction stir method. *The Paton Welding J.*, **1**, **2**–10. DOI: https:// doi.org/10.15407/tpwj2015.01.01
5. Gok, A., Aydin, M. (2013) Investigations of friction stir welding process using finite element method. *The Inter. J. of Advanced Manufacturing Technology*, **68**, 775–780. DOI: https://doi.org/10.1007/s00170-013-4798-z
6. Serindag, H.T., Kiral, B.G. (2017) Friction stir welding of AZ31 magnesium alloys — A numerical and experimental study. *Latin American J. of Solids and Structures*, 14(**1**), 113–130. DOI: https://doi.org/10.1590/1679-78253162
7. Tsaryk, B.R., Muzhychenko, O.F., Makhnenko, O.V. (2022) Mathematical model of determination of residual stresses and strains in friction stir welding of aluminium alloy. *The Paton Welding J.*, **9**, 33–40. DOI: https://doi.org/10.37434/tpwj2022.09.06
8. JMatPro® — Practical Software for Materials Properties. https://www.sentesoftware.co.uk
9. He Yang, Liang Huang, Mei Zhan (2011) Hot forming characteristics of magnesium alloy AZ31 and three-dimensional FE modeling and simulation of the hot splitting spinning process. In: *Magnesium alloys — Design, processing and properties*. Ed. by F. Czerwinski, 367–388. DOI: https://doi.org/10.5772/13778
10. Khokhlov, M.A., Makhnenko, O.O., Kostin, V.A. et al. (2024) Thermomechanical processes in friction stir welding of magnesium alloy sheets. *Avtomatychne Zvaryuvannya*, **3**, 3–10 [in Ukrainian]. DOI: https://doi.org/10.37434/as2024.03.01
11. Larikov, L.N., Yurchenko, Yu.F. (1985) *Structure and properties of metals and alloys: Thermal properties of metals and alloys:* Handbook. Kyiv, Naukova Dumka [in Russian].
12. Khairuddin, J. (2013) *Development of multicomponent loads, torque and temperature measurement device for friction stir welding process*. School of Mechanical Engineering University Sains Malaysia. DOI: https://doi.org/10.13140/RG.2.1.2165.0085

ORCID

O.O. Makhnenko: 0000-0003-2319-2976,
O.S. Kostenevych: 0000-0002-7427-2805,
O.V. Makhnenko: 0000-0002-8583-0163

CONFLICT OF INTEREST

The Authors declare no conflict of interest

CORRESPONDING AUTHOR

O.O. Makhnenko
E.O. Paton Electric Welding Institute of the NASU
11 Kazymyr Malevych Str., 03150, Kyiv, Ukraine.
E-mail: makhnenko@paton.kiev.ua

SUGGESTED CITATION

O.O. Makhnenko, O.S. Kostenevych, O.V. Makhnenko (2025) Mathematical modelling of thermal processes in friction stir welding of light alloys based on magnesium. *The Paton Welding J.*, **9**, 10–17.
DOI: https://doi.org/10.37434/tpwj2025.09.02

JOURNAL HOME PAGE

https://patonpublishinghouse.com/eng/journals/tpwj

Received: 08.04.2025
Received in revised form: 30.06.2025
Accepted: 15.09.2025

DOI: https://doi.org/10.37434/tpwj2025.09.03

MATHEMATICAL MODELING OF HEAT AND MASS TRANSFER PROCESSES DURING ELECTRON BEAM MELTING OF Ti–6Al–Nb TITANIUM ALLOY INGOTS

I.V. Krivtsun, S.V. Rymar, R.S. Gubatyuk, V.O. Berezos, D.S. Akhonin, R.V. Selin

E.O. Paton Electric Welding Institute of the NASU
11 Kazymyr Malevych Str., 03150, Kyiv, Ukraine

ABSTRACT

The results of mathematical modeling of temperature fields and hydrodynamic laminar flows of the liquid metal during electron beam melting of titanium alloy ingots are presented. The calculations were performed using the developed three-dimensional mathematical model based on the finite element method taking into account a number of simplifications and assumptions. The model allows determining the regularities of thermal and hydrodynamic processes occurring in a continuous water-cooled mould during ingot melting, and the geometry of the liquidus-solidus interphase transition zone, and accordingly, of the metal crystallization front, which significantly affects the quality of the metal during ingot formation. We calculated the parameters of the melting process for ingots of a small diameter of 110 mm from the medical Ti–6Al–7Nb titanium alloy with such a crystallization front, for which the production of high-quality metal with a homogeneous structure and a homogeneous distribution of alloying elements in the ingot volume is ensured. It was found that the heat and mass transfer in the liquid metal is significantly affected by the power of the electron beam and its distribution over the pool surface, and the heat transfer is mainly predetermined by the movement of the melt.

KEYWORDS: electron beam melting, titanium alloys, mathematical modeling, heat and mass transfer, metal crystallization front

INTRODUCTION

Light, strong, biocompatible, and non-toxic implants and endoprostheses made of metals and special alloys for medical long-term use are widely used in surgery. About 60 % of the market is occupied by implants made of metal, and titanium and its alloys are the leaders among these products [1], since their strength is equal to that of cobalt alloys, exceeds that of stainless steels, and has a modulus of elasticity that is twice lower (55–112 GPa), while that of chromium-cobalt alloy is 240 GPa and that of chromium-nickel stainless steels is 210 GPa. Such a low elasticity index is extremely important for joint and bone endoprostheses and implants, as it is closer to the indices of human bones, where it is 27.8–30.0 GPa in the longitudinal direction and 11.0–11.5 GPa in the radial and azimuthal directions.

The corrosion-resistant low-toxicity [2] Ti–6Al–4V alloy is widely used in medicine, as it surpasses stainless steels and cobalt alloys in terms of biological compatibility. Ti–6Al–4V alloy contains an order of magnitude less hazardous vanadium (4 % by weight) compared to stainless steels, in which the mass concentration of toxic nickel and chromium exceeds 30 %.

In modern metallurgy, there is a task to improve the technology for melting the latest medical titanium alloys without toxic alloying elements. At present, these are the latest titanium alloys with niobium, niobium and zirconium, and molybdenum and zirconium, which are close in their mechanical properties to Ti–6Al–4V alloy [3]. The alloys are non-toxic to the human body and have excellent biological compatibility, corrosion resistance, and ductility. Thus, the elastic modulus of Ti–6Al–7Nb alloy is less than 40 GPa.

In the future, titanium alloys may replace stainless steel and cobalt alloys in prosthetics, and surface modification of products, such as mechanical, thermal, cryogenic, electroerosion, chemical treatment, spraying, etc., further improve the modulus of elasticity, corrosion and wear resistance, reduce ion release to prevent inflammation, enhance antibacterial properties, biocompatibility, and adhesion [4–11].

The E.O. Paton Electric Welding Institute of the NAS of Ukraine (PWI) has developed electron beam melting (EBM) technology for the production of defect-free, high-quality titanium alloy ingots with a guaranteed chemical composition, including those for medical use.

One of the key factors affecting the quality of melting titanium alloy ingots is metal crystallization. The transformation of metal from a liquid to a solid state is accompanied by complex heat and mass transfer processes and rapid physical and chemical processes. The uneven temperature field in the volume of the metal ingot affects the formation of the crystallization front profile and leads to differences in the structure and chemical composition of the metal at the center and periphery of the ingot, the presence of shrinkage and liquation phenomena, etc. This significantly affects the quality of the final structure of the metal ingots.

Conducting full-scale experiments of metallurgical processes is associated with significant material

costs, which determines the prospects for using CFD modeling (CFD — Computational Fluid Dynamics) of high-temperature heat and mass transfer processes. Based on a small amount of experimental data, numerical modeling with significantly lower material costs allows calculating and obtaining, with sufficient accuracy for practical use, predicted qualitative and quantitative pictures of the phenomena occurring during metallurgical processes.

Numerical calculation methods and modern computer packages for mathematical modeling allow using thermophysical indices in the form of approximation functions of temperature, which significantly brings calculations closer to real processes.

Knowledge of heat and mass transfer processes in high-temperature melts of titanium alloys during their EBM and ingot formation is a relevant task in modern metallurgy. Knowledge of the shape of the metal crystallization front is one of the key factors in selecting technological modes for melting high-quality ingots. A homogeneous structure and uniform distribution of alloying elements in the ingot is ensured in the case of a flatter crystallization front, resulting in a more uniform temperature distribution in the ingot, which is a prerequisite for obtaining a homogeneous metal structure.

The aim of the work is to perform mathematical modeling of thermal and hydrodynamic processes of EBM of a cylindrical ingot with a diameter of 110 mm made of titanium Ti–6Al–7Nb alloy with a mass withdrawal rate of 20 kg/h, identifying the main regularities of heat and mass transfer processes during melting and determining the necessary melting modes. For this purpose, the following tasks must be solved: develop a mathematical model for calculating thermal and hydrodynamic processes in the ingot in the case of laminar flow of the liquid metal; take into account the thermophysical characteristics of the metal with their change in interphase transition zones; calculate the distribution of temperature fields in the ingot and laminar hydrodynamic flows in the melt pool, and, accordingly, the shape of the metal crystallization profile.

Achieving this aim will make it possible to determine the key technological parameters for melting ingots, which is a relevant issue in the computational search for the necessary melting process modes, excluding extremely costly full-scale experiments.

RESEARCH MATERIALS AND METHODS

The object of study in the work is a mathematical model of heat and mass transfer processes in EBM of titanium alloy ingot. The subject of study is the characteristics of hydrodynamic flows in the melt and temperature fields in the ingot.

The main hypotheses of the research are as follows: representation of the nature of moving hydrodynamic flows of the liquid metal as laminar will provide a result closer to the actual metal crystallization profile than its turbulent representation [12]; the position of the electron beam on the surface of the melt pool, its power, and the rate of ingot withdrawal are the factors that mainly influence the shape of the metal crystallization front and, accordingly, the quality of the metal in the ingot.

The following assumptions were made during the work: the liquid and solid phases of the metal ingot are considered as a single region with a liquid phase, while the solid metal corresponds to the volume in which movement is artificially suppressed by the Darcy braking force (except for the ingot's withdrawal rate) and a fixed calculation mesh is used in the finite element method; the liquidus-solidus (L–S) interphase boundary of the alloy represents a viscous transition zone in which the boundaries are determined by the liquidus and solidus temperatures, and the metal parameters change according to the proposed law relative to the volume fraction of these phases; the volume fraction of the metal in the transition zone as a function of temperature is a smoothed $F_{L–S}$ function that smoothly changes from 0 to 1, using the mathematical error function erf; approximate dependencies of the thermophysical parameters of Ti–6Al–4V and Ti–6Al–7Nb titanium alloys with smoothed stepwise phase transitions are used, applying the erf function with artificially extended temperature limits in phase transitions [13]; the distribution of the electron beam thermal power across the surface of the pool mirror varies according to the Gaussian law; since the lines of metal crystallization profiles are not visually traceable in the melt of the studied Ti–6Al–7Nb alloy, the experimental determination of these profiles was carried out on an experimental titanium alloy with similar physical properties, in which the crystallization profiles are clearly expressed.

The following simplifications are accepted: liquid metal is poured into the mould continuously at the constant rate and a constant rate of ingot withdrawal is ensured, which allows the problem to be considered as a stationary process; the mirror of the melt pool is a flat surface; the molten metal is assumed to be an incompressible viscous liquid; the heat capacity in the α–β and *L–S* phase transition zones of the alloy takes into account the equivalent heat capacity and the heat capacity from the latent heat of phase transitions; evaporation losses from the melt surface take into account only the evaporation of titanium.

The mathematical model uses the fundamental laws of conservation of energy, momentum, and mass, as well as the corresponding heat and mass transfer equations based on the Fourier and Navier–Stokes equations. The finite element numerical method was used for calculations. The ingots were melted using research equipment at the PWI [14–16].

The article is a continuation of research published by the authors in their work [12].

The originality of the work lies in the fact that, for the first time, research has been conducted on the laminar nature of melt flow for a selected mould diameter and the rate of Ti–6Al–7Nb alloy ingot withdrawal in the EBM process.

The practical significance of the work lies in the melting of high-quality titanium alloy ingots with a homogeneous metal structure.

RESEARCH RESULTS

MATHEMATICAL MODEL OF THERMAL AND HYDRODYNAMIC PROCESSES IN A CYLINDRICAL INGOT IN THE CASE OF LAMINAR METAL MELT FLOW

Let us write down the basic equations [12, 17–19] used in the model. The Fourier heat transfer equation in the case of laminar flow of the liquid metal for a stationary process is written as [18, 20, 21]:

$$\rho C_p \mathbf{u} \cdot \nabla T + \nabla \cdot \mathbf{q} = 0; \; \mathbf{q} = -\lambda \nabla T,$$

where ρ is the density of the metal, kg/m^3; C_p is the specific heat capacity of the metal, J/(kg·K); **u** is the velocity vector of the metal, m/s; ∇ is the nabla operator, m^{-1}; T is the temperature, K; **q** is the vector of specific heat flow due to heat conduction (heat flow density), W/m^2; λ is the coefficient of molecular heat conduction, W/(m·K).

In the mathematical model, heat input from the electron beam and the poured melt is balanced by heat removal from: radiation and evaporation from the mirror of the metal pool; heat transfer from the side surface of the ingot into the mould; radiation from the side surface of the ingot wall to the mould wall below the boundary of separation of their surfaces and the appearance of a gap between them (associated with shrinkage of the metal ingot with a decrease in its temperature); radiation from the ingot surface outside the mould. These factors are taken into account by the boundary conditions [12, 17] listed in Table 1.

Mathematical modeling of hydrodynamic processes during continuous feeding of incompressible titanium melt into the mould was performed using the Navier–Stokes equations for laminar flow. For a stationary process, the model has the form [12, 17, 20, 22]:

$$\rho(\mathbf{u} \cdot \nabla)\mathbf{u} = \nabla \cdot (-p\mathbf{I} + \mathbf{K}) + \mathbf{F}_d + \rho\mathbf{g};$$

$$\mathbf{K} = \mu[\nabla \cdot \mathbf{u} + (\nabla \cdot \mathbf{u})^T]; \; \rho \nabla \cdot \mathbf{u} = 0.$$

Here p is the averaged pressure value, Pa; **I** is the unit tensor; **K** is the viscous stress tensor, Pa; $\mathbf{F}_d$ is the vector of the Darcy braking force, which is artificially introduced to reduce and suppress the velocities in the viscous and solid zones, Pa/m; **g** is the vector of free-fall acceleration, m/s^2; μ is the coefficient of molecular viscosity of the liquid metal, Pa·s.

In the upper equation, in the last term, ρ is a function of temperature T. This involves the idea of he Boussinesq approximation, in which the product ρ**g** affects convection as T changes, since **g** is large enough for this product to be significant.

Darcy braking force, Pa/m, is calculated using the formula from the works [20, 23]:

$$\mathbf{F}_d = \frac{C\left(1 - F_{L-S}\right)^2}{q + F_{L-S}^3}\left(\mathbf{u} - \mathbf{u}_{cast}\right),$$

where $C \approx 10^2$–10^4 kg/(m^{3}s); $q \approx 10^{-2}$–10^{-4} are the values, whose ratio C/q must be sufficient to suppress the flow in a solid metal when $F_{L-S} = 0$ (except for the melting rate of the ingot $\mathbf{u}_{\text{cast}}$). In a liquid metal, when $F_{L-S} = 1$, the Darcy force $\mathbf{F}_d = 0$ and should not affect the flow [23]. In the transition zone, the flow corresponds to the Darcy force. Here F_{L-S} is an approximation function that determines the distribution of the volumes of liquid and solid metal in the two-phase liquidus-solidus zone in the temperature range T_L–T_S.

The hydrodynamic problem uses the boundary conditions [12, 17] from Table 1.

Figure 1 schematically shows a half of the ingot over its conditional cross-section along the vertical axis of symmetry in the middle of the conditional spot on the surface of the pool from the jet of the liquid metal poured into the pool, with the designation of geometric areas G_1–G_7. Therefore, a half of the model is considered, since in this cross-section its conditional parts are symmetrical and identical. The number of nodes in the finite element mesh is $3.1 \cdot 10^6$.

The *boundary* G_1, which is limited by the area of filling melt into the mould, is the entry to the system and can be determined either by an isothermal process with a type 1 condition (first equation), where T_{in} is the metal inlet temperature (temperature of the metal poured from the cold hearth [24]), or by an isobaric process with a type 2 condition for an open wall (second equation [12]), where **n** is the normal vector to the surface; $\mathbf{u}_{\text{in}}$ is the velocity vector of the melt jet at the inlet. Here, p_0 is the initial pressure value at the inlet point of the molten metal flow on the surface of the pool, Pa; **t** is the tangent vector to the surface.

The boundary conditions for the flow velocity in the mould are the absence of penetration through its walls $\mathbf{u} \cdot \mathbf{n} = 0$ and the presence of shear stresses. Therefore, the hydrodynamics problem is solved by assuming the presence of sliding along the boundary. The condition for the liquid metal flow to reach the pool surface, on the contrary, is the presence of penetration into the pool $\mathbf{u} \cdot \mathbf{t} = 0$, but only normal to the surface, with the absence of shear stresses — without sliding along the boundary in side directions.

Table 1. Boundary conditions of the mathematical model [12, 17]

Boundary	Heat flows	Hydrodynamic flows
G_1	$T = T_{in}$ or $-\mathbf{n}\cdot\mathbf{q} = \rho\int_{T_{in}}^{T} C_p dT\cdot\mathbf{u}_{in}\cdot\mathbf{n}$	$\mathbf{n}^T(-p\mathbf{I}+\mathbf{K})\cdot\mathbf{n} = -p_0$; $\mathbf{u}\cdot\mathbf{t} = 0$
G_2	$-\mathbf{n}\cdot\mathbf{q} = q_{eb} - q_{ev} - q_{rad2}$; $q_{eb}=P_{eb}/S_{dz}$; $q_{rad2} = \varepsilon_2\sigma(T_{vault}^4 - T^4)$	
G_3	$-\mathbf{n}\cdot\mathbf{q} = \begin{cases} -q_{conv3}, T_{in}\ge T > T_L; \\ -q_{conv3'} - q_{rad3'}, T_L \ge T \ge T_{sep}; \\ -q_{rad3}, T < T_{sep}; \end{cases}$ $q_{conv3} = h_3(T_{cryst} - T)$; $h_3 = h_L + (h_{in} - h_L)\frac{T - T_L}{T_{in} - T_L}$; $q'_{conv3} = h'_3(T_{cryst} - T)$; $h'_3 = h_L F_{L-sep} + h_{sep}(1 - F_{L-sep})$; $q'_{rad3} = \varepsilon'_3\sigma(T_{cryst}^4 - T^4)$; $\varepsilon'_3 = \varepsilon_3(1 - F_{L-sep})$; $q_{rad3} = \varepsilon_3\sigma(T_{cryst}^4 - T^4)$	$\mathbf{u}\cdot\mathbf{n} = 0$; $\mathbf{K} - (\mathbf{K}\cdot\mathbf{n})\cdot\mathbf{n} = 0$
G_4	$-\mathbf{n}\cdot\mathbf{q} = q_{rad4}$; $q_{rad4} = \varepsilon_4\sigma(T_{wall}^4 - T^4)$	
G_5	$-\mathbf{n}\cdot\mathbf{q} = 0$ or $-\mathbf{n}\cdot\mathbf{q} = \rho\int_{T_{out}}^{T} C_p dT\cdot\mathbf{u}_0\cdot\mathbf{n}$	
G_6		
G_7		$\mathbf{u} = \mathbf{u}_0$

At the *boundary* G_2, which is limited by the area of the molten metal surface in the mould, with the exception of the boundary G_1, there is heating of the melt from the electron beam (type 2 condition), its cooling due to evaporation (type 2 condition) and radiation (type 3 condition) for which: q_{eb} is the specific heat flow from the electron beam heating this surface, W/m^2; P_{eb} is the thermal power from the electron beam, W; S_{dz} is the surface area of the pool of the molten metal, m^2, $S_{dz} = \pi r^2$; r is the radius of the surface of the pool of the molten metal, m. The heat flow q_{eb} is distributed across the surface of the molten metal pool either uniformly or (and) according to a Gaussian distribution along the radius. In the latter case, the Gaussian distribution of the heat power from the electron beam on the surface of the pool and the radius of the spot from the beam are taken into account; q_{ev} is the specific heat flow caused by the evaporation of the liquid metal from the surface of the pool, W/m^2; q_{rad2} is the specific heat flow of radiation from the surface of the liquid metal pool, W/m^2 [25]; ε_2 is the dimensionless emissivity coefficient of the system of surfaces of the following bodies: liquid metal of the pool surface — vault of the vacuum chamber, between which the process of radiant heat exchange takes place; $\sigma = 5.67\cdot10^{-8}$ W/(m$^2\cdot$K^4) — Stefan–Boltzmann constant; T_{vault} is the temperature of the vacuum chamber vault above the pool surface. The emissivity coefficient for the system of surfaces of two bodies a and b at the i-th boundary is calculated using the formula [26]:

$$\varepsilon_i = (\varepsilon_a^{-1} + \varepsilon_b^{-1} - 1)^{-1};$$

ε_a and ε_b are the emissivity coefficients for the corresponding surfaces.

At the *boundary* G_3, which is limited by the walls of the mould, both conductive and radiant heat transfer occur (type 3 conditions), where: q_{conv3} is the specific heat flow in the case of conductive heat exchange, W/m^2, passing over the height of the mould wall area with a temperature T_{cryst}, which is in contact with the liquid metal having a temperature above the liquidus temperature T_L [25]; h_3 is the heat transfer coefficient from the surface of the liquid metal of the ingot, which integrally takes into account the heat transfer from it through the mould wall to the cooling water, W/(m$^2\cdot$K). In this area, it is assumed that with a decrease in the melt temperature, it linearly decreases

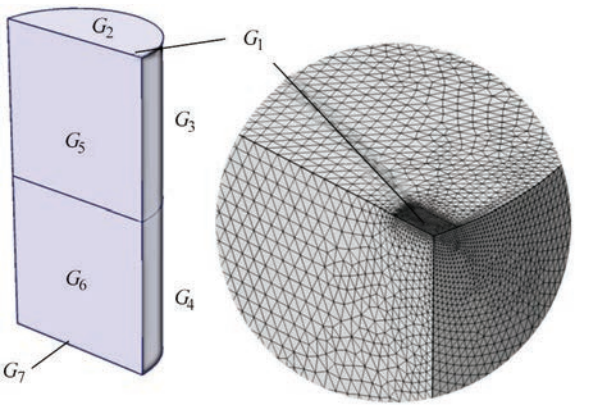

Figure 1. Geometric model and a fragment of the finite element mesh in the region of metal pouring

from the value h_{in} to the value h_L; q'_{conv3} is the specific heat flow in the case of conductive heat exchange, W/m^2, passing along the height of the mould wall area that is in contact with the metal ingot, which has a temperature lower than the liquidus temperature T_L and higher than the temperature at which the ingot is separated from the mould wall T_{sep} due to the shrinkage of the metal as a result of its cooling; h'_3 is the heat transfer coefficient from the surface of the metal ingot, which integrally takes into account the heat transfer from it through the mould wall to the cooling water, W/(m^2·K). In this area, it is assumed that with a decrease in the metal temperature, h'_3 decreases according to the approximation function $F_{L–\text{sep}}$ (by analogy with the function $F_{L–S}$) from the value h_L to the value h_{sep}; q'_{rad3} is the specific heat flow caused by radiation from the metal ingot surface, W/m^2, which falls on the area of the mould wall with the temperature of the metal ingot below the liquidus temperature T_L and above the temperature of the ingot separation from the mould wall T_{sep}; ε'_3 is a dimensionless coefficient of the reduced emissivity for the system of surfaces of bodies in this area; ε_3 is a dimensionless coefficient of the reduced emissivity for the system of surfaces of bodies of the metal ingot and the mould wall, between which the process of radiant heat exchange occurs; q_{rad3} is a specific heat flow caused by radiation from the surface of the metal ingot, W/m^2, falling on the area of the mould wall with a metal ingot temperature below the temperature of the ingot separation from the mould wall T_{sep}.

At the *boundary* G_4, which is limited by the vertical walls of the ingot yielded from the mould, only radiant heat exchange occurs (type 3 condition), where q_{rad4} is the specific heat flow of radiation from the side surface of the metal ingot, W/m^2, falling on the wall of the vacuum chamber with a temperature T_{wall}, ε_4 is a dimensionless emissivity coefficient for the system of surfaces of bodies metal ingot and wall of the vacuum chamber in this area.

At the *boundaries* G_5 *and* G_6, which are limited by the cross-sectional plane passing along the vertical axis of symmetry of the ingot along its height, type 2 condition is observed.

The *boundary* G_7 is limited by the cross-sectional plane of the of the lower part of the ingot at such a distance from its upper part where thermal processes no longer affect the thermal processes in its upper part in the region of the metal crystallization front. This boundary is a conditional exit from the system. The distance to it is determined by iterative calculation. At this boundary, one can choose either type 2 condition of an adiabatic process of a closed wall (thermal insulation) (first equation), or type 2 condition of isobaric process for an open wall (second equation [12]), where T_{out} is the approximate value of the temperature at the boundary G_7, which is specified during the calculations; $\mathbf{u}_0$ is the vector of ingot withdrawal rate, m/s.

The vault and walls of the vacuum chamber are water-cooled.

To calculate thermal and hydrodynamic processes with a present phase transition in metal, a finite element numerical method with a fixed calculation mesh was used, in which the liquid and solid phases are considered as a single region. The interphase region is located between temperatures T_L and T_S and is considered as a viscous transition zone, the parameters of which change relative to the volume fractions of the phases according to a certain law. The liquid phase is present at temperatures above the liquidus temperature T_L, and the solid phase is present at temperatures below the solidus temperature T_S.

The volume fraction of $F_{L–S}$ liquid in the two-phase zone as a function of temperature is described by a smoothed function using the erf error function, which is an internal function of many computer calculation software packages:

$$F_{L–S}(T) = \begin{cases} 0, T < T_S; \\ \dfrac{y_{\max} - y_{\min}}{2} \times \\ 1, T_L < T, \end{cases}$$

$$\times \left[1 + \operatorname{erf} \left(\frac{x - \dfrac{x_{\min} + x_{\max}}{2}}{\dfrac{x_{\max} - x_{\min}}{x_{\max,\text{erf}} - x_{\min,\text{erf}}}} \right) \right] +$$

$$+ y_{\min}, T_S \le T \le T_L;$$

where $y_{\min} = 0, y_{\max} = 1$; $x_{\min}, x_{\max}$ are the specified minimum and maximum values on the abscissa axis, at which the minimum and maximum values of the $F_{L–S}$ function approach 0 and 1 (here $x_{\min} = T_S$, $x_{\max} = T_L$); $x_{\min,erf}$, $x_{\max,erf}$ are the minimum and maximum values on the abscissa axis of the erf function itself, at which it approaches the values on the ordinate axis –1 and 1. Usually, if $x_{\min,erf} = –2$, the function $erf(–2) = –0.99532$, and if $x_{\max,erf} = 2$, the function $erf(2) = 0.99532$, which is a sufficient approximation to –1 and 1. But if a greater approximation is necessary, we can take the value $x_{\min,erf} = –e$, where the function $erf(–e) = –0.99988$, and if $x_{\max,erf} = e$, the function $erf(e) = 0.99988$.

In the two-phase liquidus-solidus transition zone, the $F_{L–S}$ curve has a growing dependence, and for $(1 – F_{L–S})$ — a falling dependence (Figure 2). By analogy with the $F_{L–S}$ function, the $F_{\alpha–\beta}$ function was also applied in the corresponding temperature range of the α–β phase transition.

For the alloy under consideration, the following temperatures are specified: at the artificially expanded boundaries of the α-β phase transition, $T_\alpha = 1253$ K, $T_\beta = 1283$ K for the actual temperature $T_{\alpha–\beta} = 1283$ K

[27]; at the boundaries of the *S–L* phase transition, T_S = 1873 K, T_L = 1923 K, with an actual temperature $T_{L–S}$ = 1923 K [27]; the temperature at which the ingot is separated from the mould wall T_{sep} = 1640 K; the temperature of the metal at the mould inlet T_{in} = 2061 K. Latent heat of phase transitions (change in system enthalpy) [27]: $H_\alpha - H_{25} = 6.36 \cdot 10^5$ J/kg, $H_\beta - H_{25} = 6.84 \cdot 10^5$ J/kg and $H_{\alpha–\beta} = H_\beta - H_\alpha = 4.8 \cdot 10^4$ J/kg; $H_S - H_{25} = 1.180 \cdot 10^6$ J/kg, $H_L - H_{25} = 1.466 \cdot 10^5$ J/kg and $H_{L–S} = H_L - H_S = 2.86 \cdot 10^5$ J/kg; H_{25} is the initial enthalpy of the system at 25 °C (298 K).

THERMOPHYSICAL PARAMETERS

take into account their changes from temperature and α–β and *L–S* phase transitions, while the specific heat capacity of metal also takes into account the latent heat of phase transitions, which were calculated using the methodology described in [18].

The finite element numerical method is sensitive to discontinuities and step jumps in function values, when the method cannot always find a solution and calculations fail. Step changes in the thermophysical characteristics of titanium alloys are present at α–β and *L–S* phase transitions. It is necessary to make such a mathematical description of the functions in order to achieve a smooth transition of values in the zone of step jumps. For this purpose, an approach known in modelling of thermal processes was used, involving a slight artificial expansion of the ranges of such zones [13] in which the values of characteristics change smoothly. In the case under consideration, this is conveniently implemented by the functions $F_{\alpha–\beta}$, $1 - F_{\alpha–\beta}$, $F_{L–S}$ and $1 - F_{L–S}$, taking into account the increase or decrease in values in phase transitions. The approximations of the thermophysical parameters are performed namely in this way (Figure 3) [12].

Figure 3 shows the approximation curves of the simulated thermophysical characteristics of Ti–6Al–4V titanium alloy as a function of temperature, obtained from the data in [27]. Similar dependencies for Ti–6Al–7Nb alloy have not been found in the literature. However, the characteristics of these related alloys are very similar, so the ratios for the first alloy can be applied to the second alloy with a sufficiently close approximation. Moreover, the specific heat capacity C_p for Ti–6Al–7Nb alloy can be specified using existing methods.

For an approximate calculation of the heat capacity of titanium alloys, the Neuman–Kopp rule (the rule of additive heat capacity) can be used. This is an empirical method for estimating the specific heat capacity of multicomponent alloys and complex materials based on the heat capacities of their constituent elements. The approach is based on the assumption that the total specific heat capacity of the alloy is the sum of the heat capacities of its individual components. For an

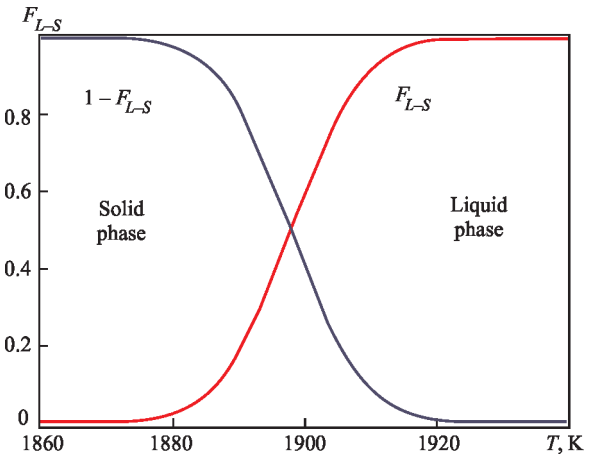

Figure 2. Dependence of the volume fraction of liquid on temperature in the two-phase zone when using the $F_{L–S}$ and $(1 - F_{L–S})$ functions

approximate estimate of the specific heat capacity of the alloy C_p, the following ratio is used:

$$C_p = \sum_{i=1}^{n} N_i C_{p,i},$$

where N_i is the mass fractions of the i-th component of the alloy, %; $C_{p,i}$ is the specific heat capacity of the *i*-th component of the alloy; *n* is the number of components of the alloy.

Based on this approach, the heat capacity values for Ti–6Al–4V and Ti–6Al–7Nb alloys were calculated. The C_p values obtained using the Neumann–Kopp rule for Ti–6Al–7Nb alloy are lower than the C_p values for Ti–6Al–4V alloy obtained using the same rule by an average of 3 % over the entire calculated temperature range of 300–2800 K. However, if we compare the calculated values of heat capacity C_p obtained using the Neumann–Kopp rule and the existing data for Ti–6Al–4V alloy [27], the discrepancy between them in the temperature range from 300 to 1800 K does not exceed 5 %, and from 1800 K to 2800 K it increases to 17 %, which indicates the insufficient accuracy of this approach at high temperatures.

The second, more accurate approach to calculating the specific heat capacity of Ti–6Al–7Nb alloy is based on the already known values of the dependence of C_p on the temperature of Ti–6Al–4V alloy [27]. Since Ti–6Al–4V and Ti–6Al–7Nb alloys differ only in V and Nb elements, and to a small extent, in the Ti content, it is worth applying the approach of additive contribution of elements to the heat capacity.

This approach is based on the use of the rule of total contributions, according to which the specific heat capacity of a multicomponent alloy can be expressed as a linear combination of the heat capacities of its constituent elements, which can be described as follows:

$$C_p(T)_{\text{Ti–6Al–7Nb}} = C_p(T)_{\text{Ti–6Al–4V}} + \Delta C_p.$$

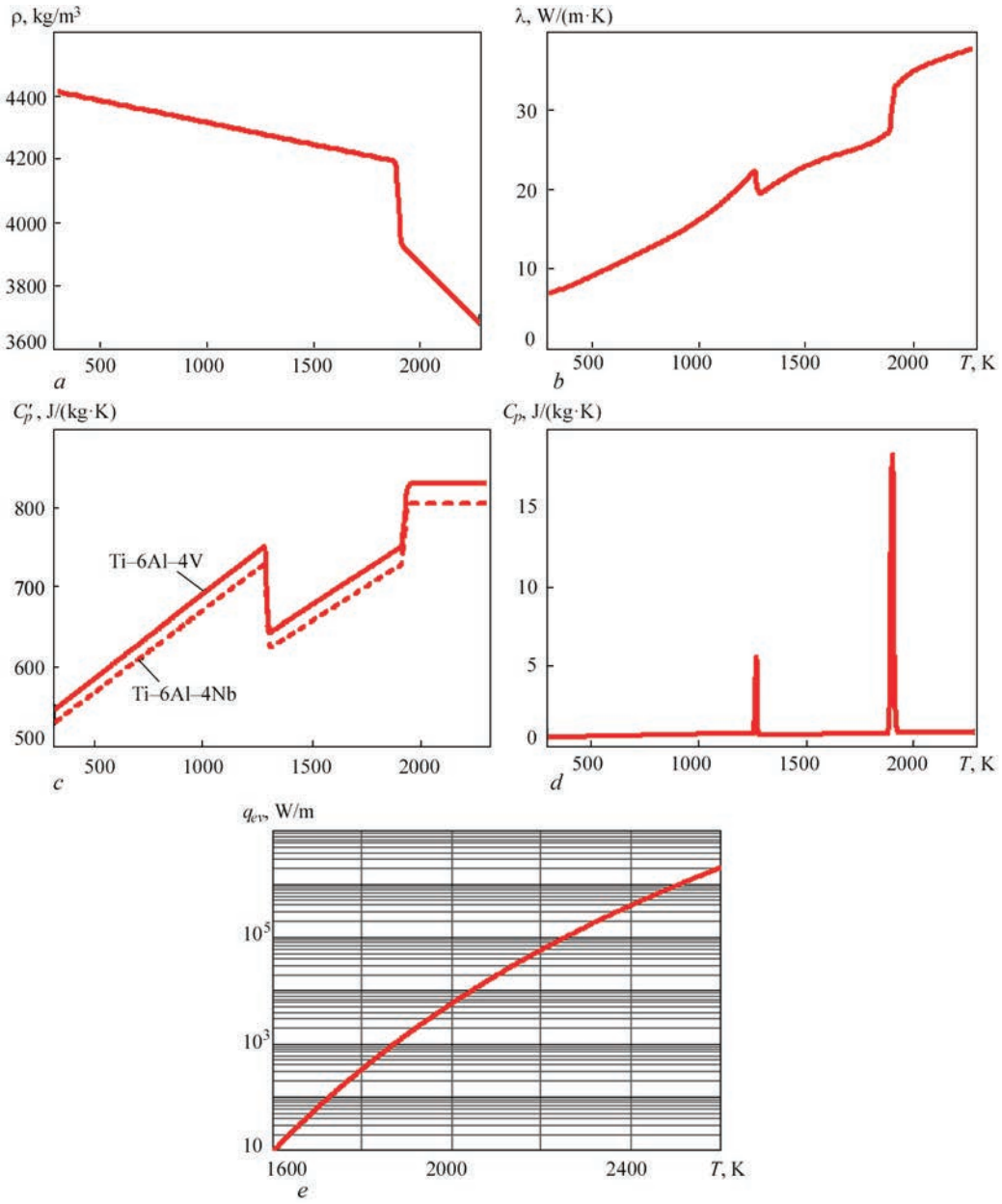

Figure 3. Approximation dependencies of the modelled thermophysical parameters of Ti–6A1–7Nb titanium alloy on temperature T: *a* — density ρ; *b* — thermal conductivity λ; *c* — specific heat capacity C'_p, *d* — specific heat capacity C_p taking into account the latent heat of α–β and *L*–*S* phase transitions; *e* — evaporation losses q_{ev} from the surface of the Ti melt

Here, ΔC_p is a correction that takes into account the difference in the heat capacities of V and Nb. The heat capacity of pure V and Nb is available from literature sources and can be used to calculate the contribution of substituted atoms:

$$\Delta C_p = (C_{p,\mathrm{Nb}} - C_{p,\mathrm{V}}) \cdot \Delta\omega,$$

where Δω is the difference in the content of substituted elements.

As a result, the calculated heat capacity values for Ti–6A1–7Nb alloy were found to be lower than the known data for Ti–6A1–4V alloy by an average of 3 % over the entire temperature range of 300–2800 K. This indicates the high accuracy of the used approach. Figure 3 shows the known dependence of $C_p(T)$ for Ti–6A1–4V alloy [27] and the calculated dependence for Ti–6A1–7Nb alloy, which was used for the calculations.

Regarding losses to evaporation from the melt surface (Figure 3, *d*). No such data has been found in the literature for Ti–6A1–4V and Ti–6A1–7Nb alloys. Therefore, it is necessary to use known data for pure titanium. This is acceptable since the alloying elements for these alloys constitute 10 and 13 % of the specific masses of the alloys, respectively.

In [28], an approximate formula is given that describes the dependence of the logarithm of the pressure P of saturated titanium vapour on temperature T, K:

$$\lg P(T) = -A \cdot T^{-1} + B - C \cdot \lg(T),$$

where the approximation coefficients for Ti are: $A = 22964$; $B = 10.581$ and $C = 0.373$.

The saturated vapour pressure is equal to $P(T) = 10^{\lg P(T)}$.

Using the Langmuir equation [30], the evaporation rate of titanium, kg/(m²·s), is determined

$$J_{ev}(T) = P(T)\sqrt{\frac{M_{mol}}{2 \cdot \pi \cdot R \cdot T}}.$$

Here, M_{mol} is the atomic (molar) mass of Ti, M_{mol} = = 0.047867 kg/mol; R is the universal gas constant, R = 8.31446261815324 J/(mol·K).

From the known value of the latent molar heat of evaporation of titanium $\Delta H_{ev,mol}$ = 410 kJ/mol [28], its latent heat of evaporation is calculated:

$$\Delta H_{ev} = \Delta H_{ev,mol}/M_{mol} = 8565.4 \text{ kJ/kg}.$$

The specific power of titanium evaporation losses depending on temperature is equal to

$$q_{ev}(T) = J_{ev}(T)\,\Delta H_{ev}$$

and is shown in Figure 3, *d*.

RESULTS AND ANALYSIS OF MATHEMATICAL MODELLING OF LAMINAR HYDRODYNAMIC PROCESSES AND TEMPERATURE FIELDS IN THE INGOT

Three-dimensional mathematical modelling was performed for a system of laminar hydrodynamic processes and temperature fields in the ingot in a continuous mould with an internal diameter of 110 mm and a height of 150 mm at a mass withdrawal rate of the ingot (melting rate) of 20 kg/h. The pouring of preliminary molten metal from a cold hearth onto the surface of the pool occurs near the mould wall into a conditionally square spot of 10×10 mm (equivalent diameter is 11.3 mm). The rate of metal pouring into the pool and its pressure on its surface are taken into account by the boundary conditions at the boundary G_1 (Table 1). The surface of the liquid metal pool is heated by a 16 kW power electron beam with an efficiency of 75 %, which moves in a circle around the periphery of the pool according to the Gaussian distribution of the electron beam thermal power (Figure 4).

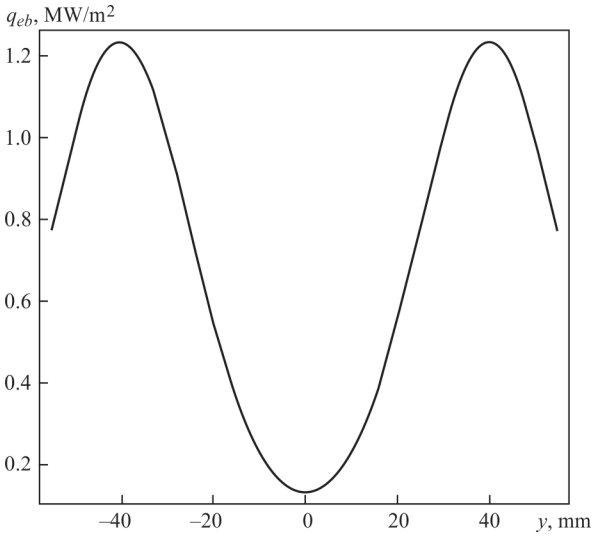

Figure 4. Distribution of the thermal power of the electron beam q_{eb} over the ingot surface (along the y coordinate)

Based on the developed mathematical model, temperature fields and hydrodynamic flows were calculated for the case of forming a Ti–6Al–7Nb titanium alloy ingot using the EBM method. Here, the temperature-dependent thermophysical characteristics of the metal were used, and interphase transition zones were taken into account. This allowed identifying the regularities of the distribution of hydrodynamic flows in the liquid metal and temperature fields, as well as the metal crystallization front during ingot formation.

Figure 5, *a* shows the directions of the velocity vectors of the liquid metal flows, excluding the withdrawal rate of the ingot towards the bottom in the axial direction. A cross-section along the vertical axis of symmetry of the ingot is considered in the middle of the conditional spot on the surface of the pool from the jet of the liquid metal poured into the pool. The size of the vectors is selected on a logarithmic scale proportional to the velocity of the melt.

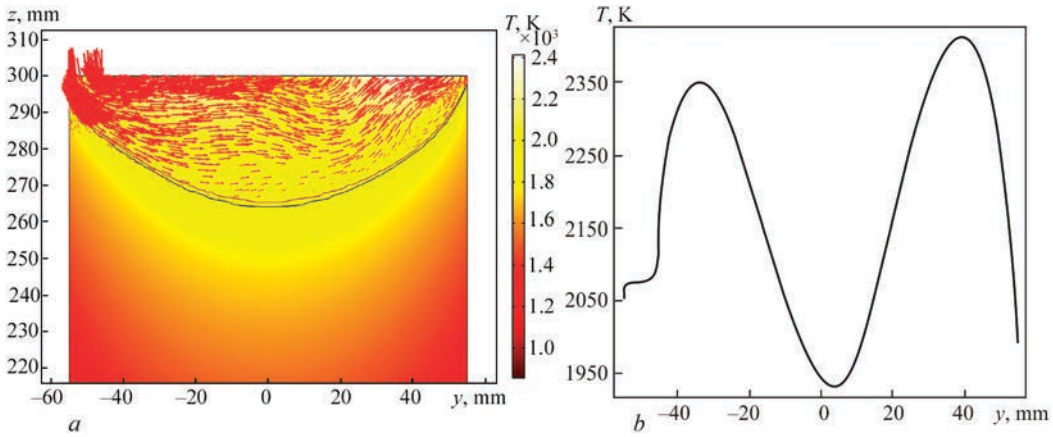

Figure 5. In the section (along the *y* coordinate) along the vertical axis of symmetry of the ingot (*z* coordinate) at the centre of the conditional spot on the surface of the pool from the jet of liquid metal poured into the pool, the following are presented: *a* — flows of the liquid metal in the pool; *b* — temperature on the surface of the pool

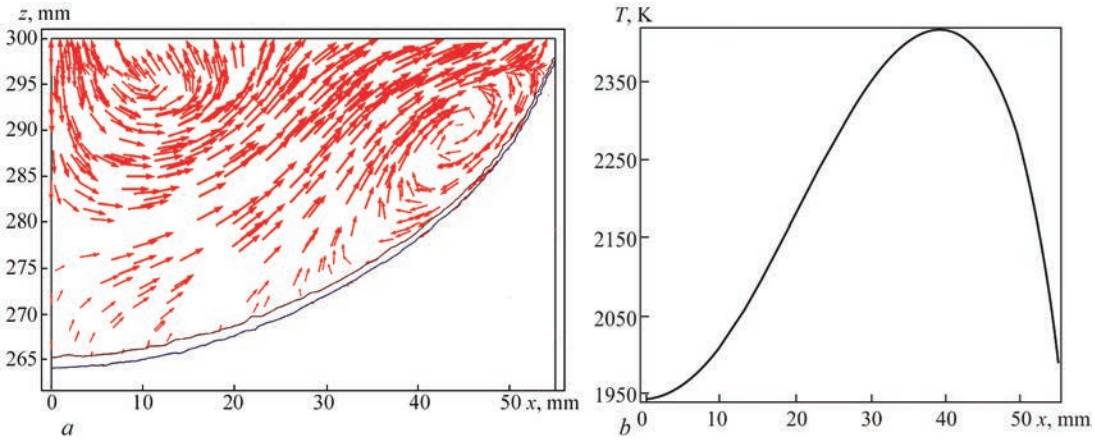

Figure 6. In the section at an angle of 90° (along the x coordinate) along the vertical axis of symmetry of the ingot (z coordinate), the following are presented: *a* — flows of the liquid metal in the pool; *b* — temperature on the surface of the pool

Figure 5, *b* shows a diagram of the temperature distribution on the pool surface of the liquid metal according to the Gaussian distribution of the thermal power of the electron beam around the periphery of the melt.

Figure 6, *a* shows the directions of the velocity vectors of the liquid metal flows, excluding the withdrawal rate of the ingot towards the bottom in the axial direction. A cross-section along the vertical axis of symmetry of the ingot at an angle of 90° from the centre of the conditional spot on the surface of the pool from the jet of the liquid metal poured into the pool is considered. This plane is perpendicular to the plane shown in Figure 5, *a*. Only half of the figure is shown, since the other half is symmetrical.

Figure 6, *b* shows a diagram of the temperature distribution on the surface of the molten metal pool.

Figure 7 shows the three-dimensional distribution of the temperature field and the directions of the velocity vectors of the metal flow in the mould, excluding the withdrawal rate of the ingot towards the bottom.

Flows of the liquid metal (Figure 5, *a*) spread from the point of its pouring on one side of the mould wall to the opposite side of the wall, forming a small vortex near the latter. The figure shows the isotherms of the liquidus T_L (upper curve) and solidus T_S (lower curve) at the boundary of the crystallization front. The position and geometry of this front (Figure 5, *a*, Figure 6, *a* and Figure 7) largely determine the quality of the ingot formation and the concentration of alloying elements in its volume. The flatter the front, the more homogeneous the structure of the solid metal ingot in the radial direction.

An important criterion for the quality of titanium alloy ingots is the smooth appearance of their side surfaces. Therefore, during melting, it is necessary to

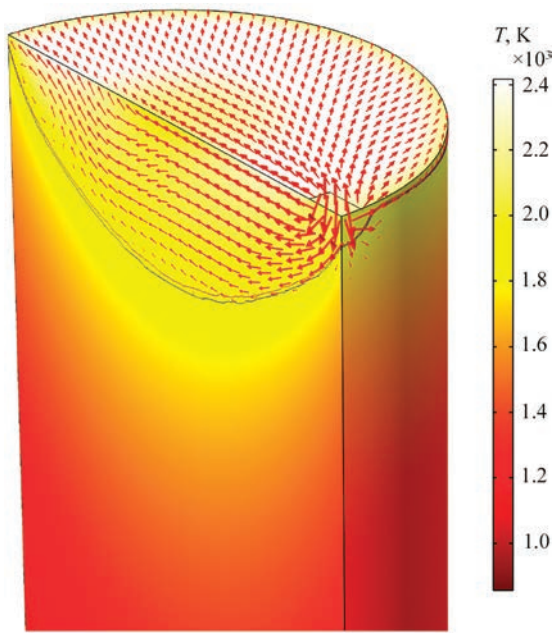

Figure 7. Three-dimensional distribution of the temperature field and metal flows in the mould, excluding the rate of ingot withdrawal to the bottom

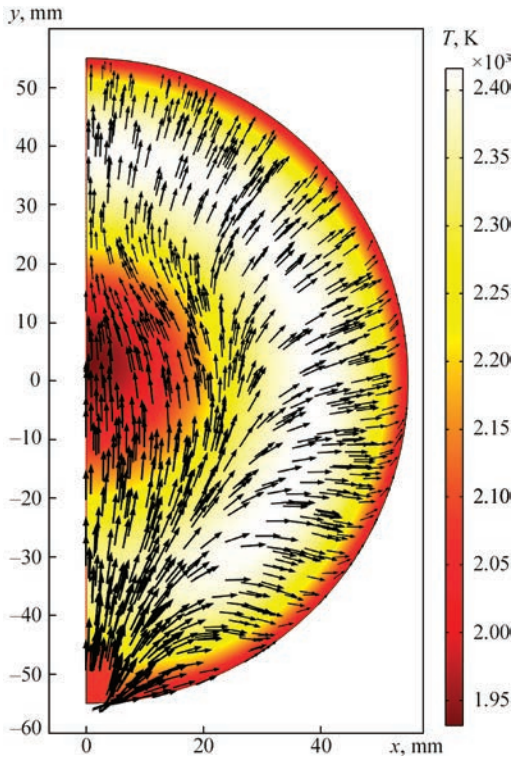

Figure 8. Distribution of the temperature field and metal flows in the mould (top view along the x and y coordinates)

minimize the contact of the liquid metal pool with the mould wall in order to avoid corrugations on the side surfaces of the ingots.

The correct choice of the electron beam position in the radial direction on the pool surface ensures the condition that the liquid metal in the pool has less contact with the mould wall, and the intensity of the beam provides the desired depth and geometry of the crystallization front. The diagram of the temperature distribution on the surface of the molten metal pool (Figure 5, *b*) shows that the maxima on the curve are predetermined by the concentrations of thermal power introduced by the electron gun beam. This temperature distribution ensures the required shape of the metal crystallization front in Figure 5, *a*.

In the cross-section of the ingot in Figure 5, *a*, a single vortex flow is observed.

Figure 8 shows the distribution of the temperature field and metal flows in the mould (top view), and Figure 9 shows the three-dimensional distribution of the molten metal flows in the ingot.

The flows of the molten metal for different vertical cross-sections of the ingot in Figures 5, *a* and 6, *a* are different, as they depend on the place where the liquid metal is poured into the mould. This is seen in the three-dimensional distribution of the temperature field and metal flows in the mould (Figures 7 and 8) and the melt flows in the ingot (Figure 9). In the top view (Figure 8), a pronounced diametrical distribution of metal flows is observed, which is caused by the action of flows from the liquid metal poured into the mould and the thermal power from the electron beam.

Analysis of the results obtained using the mathematical model showed that the velocity of the liquid metal in the mould at the point of pouring is $18 \cdot 10^{-3}$ m/s, and the velocity of a circumferential flow closer to the centre of the mould on the pool surface is ~$2 \cdot 10^{-3}$ m/s (Figure 9), which corresponds to Reynolds numbers Re ≈ 260 and 125, the value of which characterises the laminar flow of the melt in the pool.

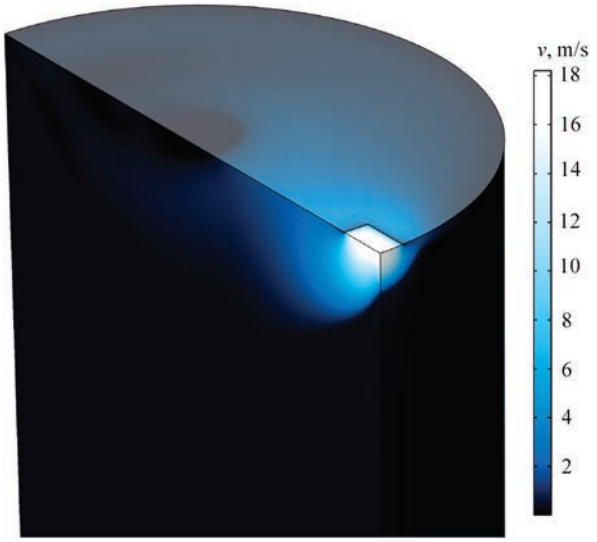

Figure 9. Three-dimensional distribution of the molten metal flows in the ingot with the scale of their velocity *v*

Figure 10 shows the directions of the liquid metal flows, taking into account the rate of ingot withdrawal downwards in the axial direction. A cross-section along its vertical axis of symmetry is considered in the middle of the conditional spot on the pool surface from the jet of the liquid metal poured into the pool.

The results of calculations of metal trajectories confirmed the adequate use of the Darcy function to suppress the metal movement in the solid phase.

ANALYSIS OF THE RESULTS OF MATHEMATICAL MODELLING OF THE INFLUENCE OF EBM TECHNOLOGICAL PARAMETERS ON LAMINAR HYDRODYNAMIC PROCESSES AND TEMPERATURE FIELDS IN THE INGOT

Mathematical modelling was performed for different positions of the electron beam centre relative to the vertical axis of symmetry of the ingot and different withdrawal rates.

In order to determine how the position of the electron beam, moving in the azimuthal direction along the surface of the ingot, affects the melt pool, Figure 11 shows the temperature distribution on the surface of the pool for different positions of the electron beam centre relative to the vertical axis of symmetry of the ingot at distances of 39, 41, 43 (operating mode), 45 and 47 mm. Figure 12 shows the temperature distribution and crystallization profiles of the metal and two-phase zones in the case of the electron beam position relative to the vertical axis of symmetry of the ingot: *a* — at a distance of 39; *b* — 43 (operating mode); *c* — 45 mm. It is seen that the position of the beam significantly affects the geometry of the pool. The closer the beam rotates to the centre (39 mm), the higher the temperature on the surface of the melt (Figure 11) and the deeper the pool becomes (Figure 12, *a*). When the beam is moved away from the centre of the mould (43 mm — operating mode), the

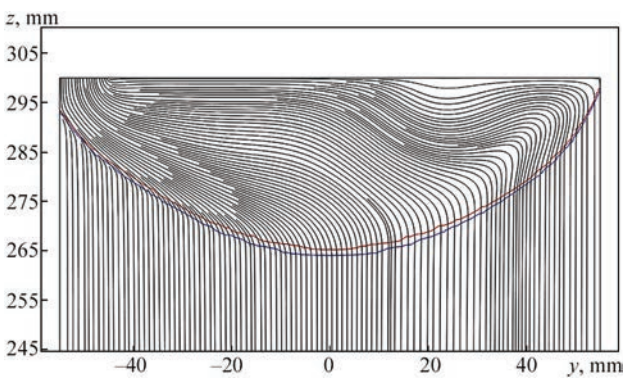

Figure 10. Directions of flows of the liquid metal taking into account the rate of ingot withdrawal to the bottom in the axial direction (along the *z* coordinate) in the cross-section (along the *y* coordinate) along its vertical axis of symmetry

temperature on the surface of the melt decreases and reaches the liquidus temperature T_L of the melt in the lower part of the curve (Figure 11), which is optimal, and the pool decreases in depth (Figure 12, *b*). In this case, the crystallization profile becomes flatter, which is the desired result. When the centre of the beam is moved by 45 mm from the vertical axis of symmetry of the mould, the temperature at the bottom of the curve becomes lower than the solidus temperature T_S (Figure 11) and an island of solidified metal appears on the surface of the pool (Figure 12, *c*), while the pool decreases in depth. However, this is an unacceptable mode due to the appearance of unmelted metal on the surface of the pool. If the centre of the beam is moved by 47 mm, the temperature on the surface of the pool becomes even lower (Figure 11), and the proportion of unmelted metal increases.

A significant cause for the decrease in temperature on the surface of the melt when the centre of the electron beam is moved from the vertical axis of symmetry of the mould towards its wall is that a significant part of the beam hits the upper end of the mould wall rather than the surface of the melt. This reduces the useful power for heating the melt.

Figure 13 shows how the temperature field distribution, flows of the liquid metal, its crystallization profiles and two-phase zones change at different rates of melt pouring into the mould and, accordingly, at different withdrawal rates of the ingot. It is seen that as the rate of pouring the melt increases, the depth of the pool increases significantly, and its profile becomes more concave.

A flatter metal crystallization front of the metal ingot, which is desired, is formed at lower rates of melt pouring into the mould and, accordingly, at lower rates of ingot withdrawal.

Figure 14, *a* and b shows the interpolation dependencies of the liquid metal pool depth *l* and the liquid metal pool shape coefficient k_f, which is equal to the ratio between the mould diameter d_{kr} and the pool depth *l*, $k_f = d_{kr}/l$, on the mass withdrawal rate of the ingot v_g, which pass through six calculation points corresponding to the pool depths in Figure 13.

With an increase in the mass withdrawal rate of the ingot above 10 kg/h, the pool depth grows linearly, and the coefficient k_f decreases.

In the case of a mass melting rate of 20 kg/h and an electron beam heating power of 16 kW in the mould, a crystallization front close to flat one is formed, and

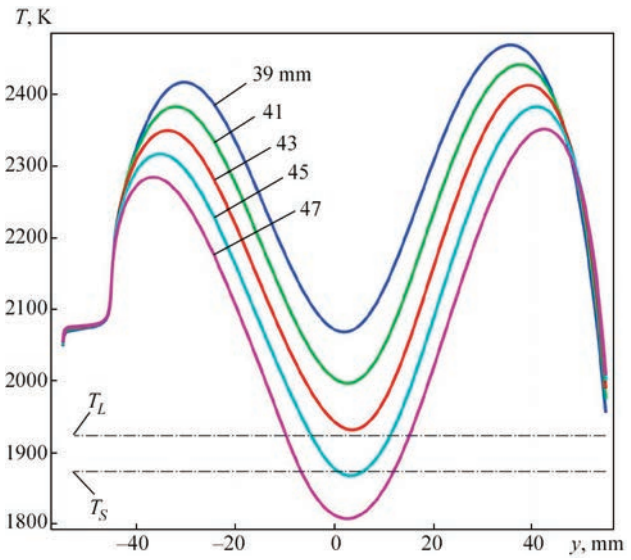

Figure 11. Temperature on the surface of the melt pool in the case of different position of the electron beam centre relative to the vertical axis of symmetry of the ingot (along the *z* coordinate) at distances (along the *y* coordinate) of 39, 41, 43 (operating mode), 45 and 47 mm

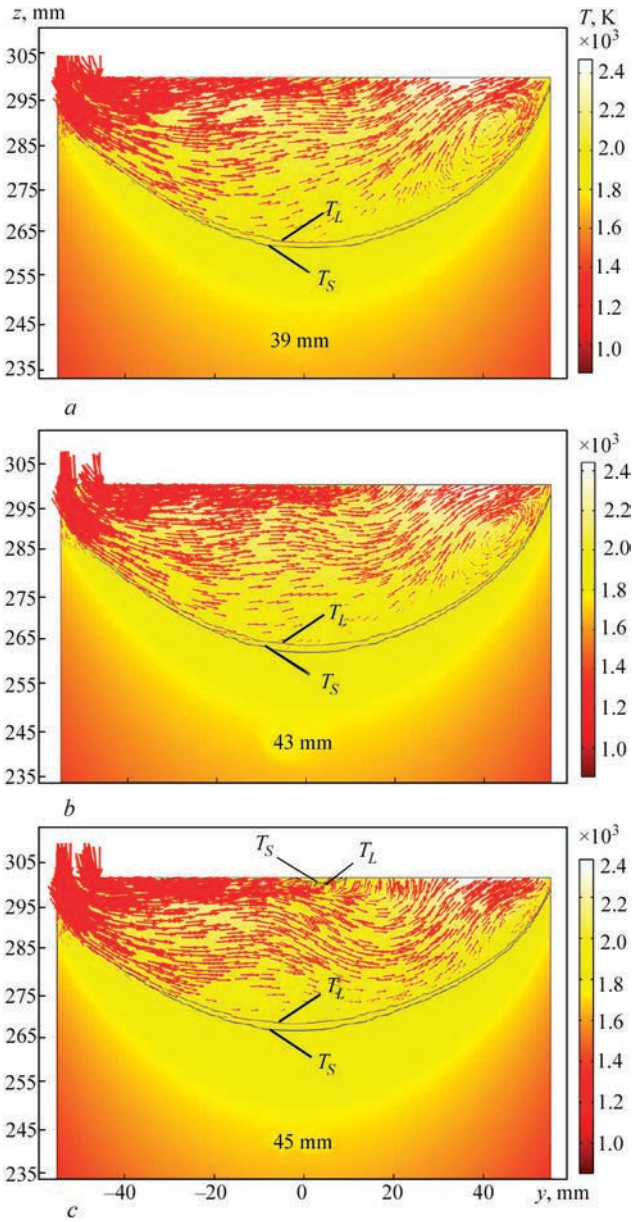

Figure 12. Temperature distribution and profiles of metal crystallization and two-phase zones (along the *y* coordinate) in the case of different position of the electron beam relative to the vertical axis of symmetry of the ingot along the *z* coordinate: *a* — at a distance of 39; *b* — 43 (operating mode); *c* — 45 mm

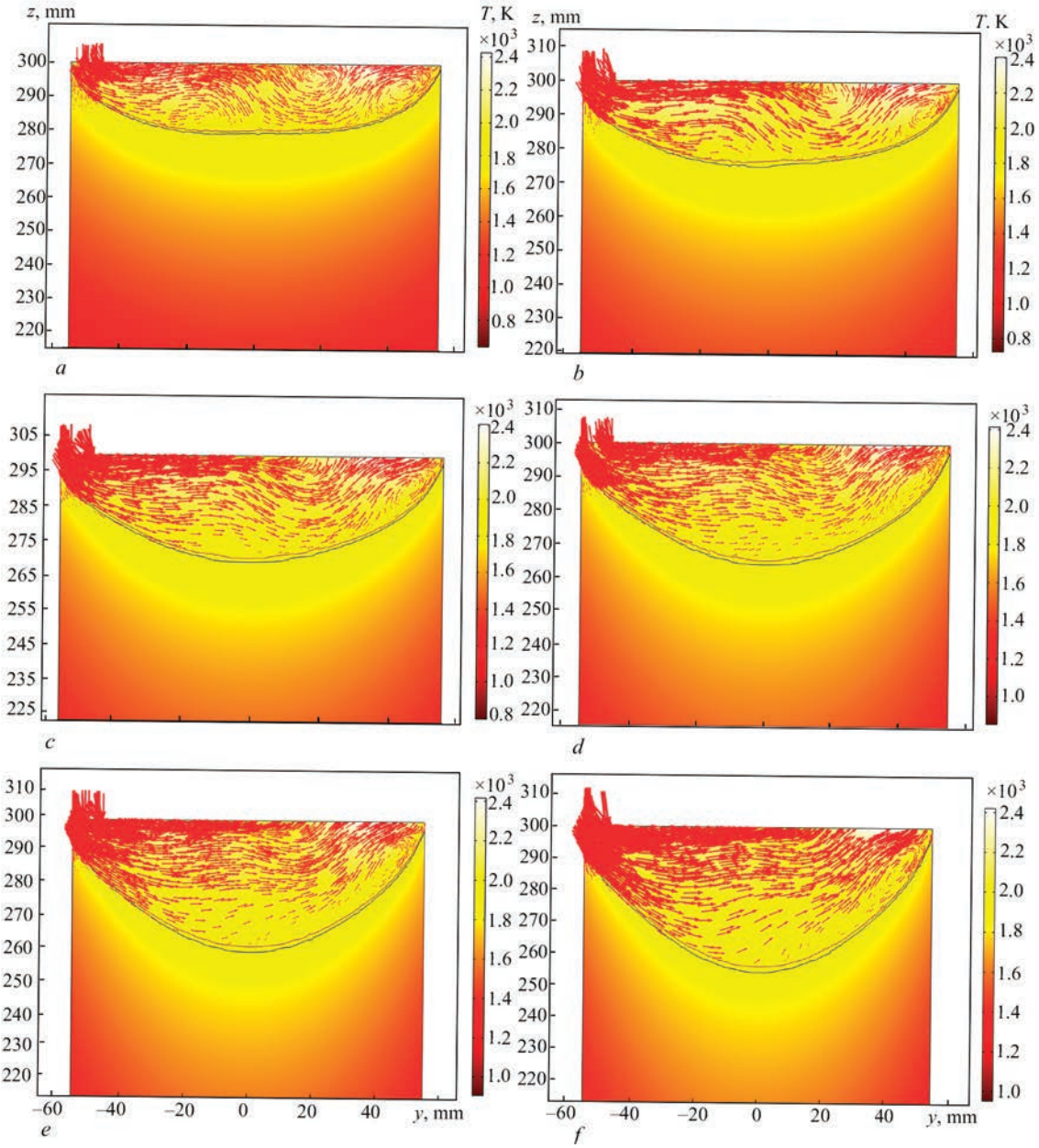

Figure 13. Distribution of the temperature field, flows of the liquid metal and profiles of its crystallization and two-phase zones (along the *y* and *z* coordinates) in the case of different mass rates of ingot withdrawal (along the z coordinate), kg/h: *a* — 5; *b* — 10; *c* — 15; *d* — 20 (operating mode); *e* — 25; *f* — 30

the pool shape coefficient is 3.24, i.e. the depth of the melt pool is 3.24 times less than its width.

Figure 15 shows the temperature distribution on the surface of the melt pool for different mass withdrawal rates of the ingot: 5, 10, 15, 20 (operating mode), 25 and 30 kg/h. For rates of ingot withdrawal of 10–30 kg/h, the position of the electron beam centre relative to the vertical axis of symmetry of the ingot was at a constant distance of 43 mm, which corresponds to the operating mode. For a mass rate of 5 kg/h, this distance was taken smaller — 41 mm in order to ensure a complete melting of the metal on the pool surface, since at a distance of 43 mm in this mode, an island with solidified metal is formed in the center of the pool surface, which is unacceptable. Reducing this distance to 41 mm led to an increase in the temperature on the pool surface, and accordingly to a rise in the temperature distribution curve (Figure 15) for a mass rate of 5 kg/h. This caused the appearance of a nonlinear region on the diagrams (Figure 14, *a*) for a mass rate of less than 10 kg/h.

In order to assess the adequacy of the plotted mathematical model, an ingot with a diameter of 110 mm was metled from an experimental complex-alloy titanium alloy, close in physical properties to Ti–6A1–7Nb alloy, in which the metal crystallization profiles are clearly displayed. A longitudinal template was cut out from the upper part of this ingot and its macrostructure was revealed by etching. A great number of alloying elements in the experimental alloy allowed a clear identification of the crystallization profiles at different melting rates. Figure 16 shows

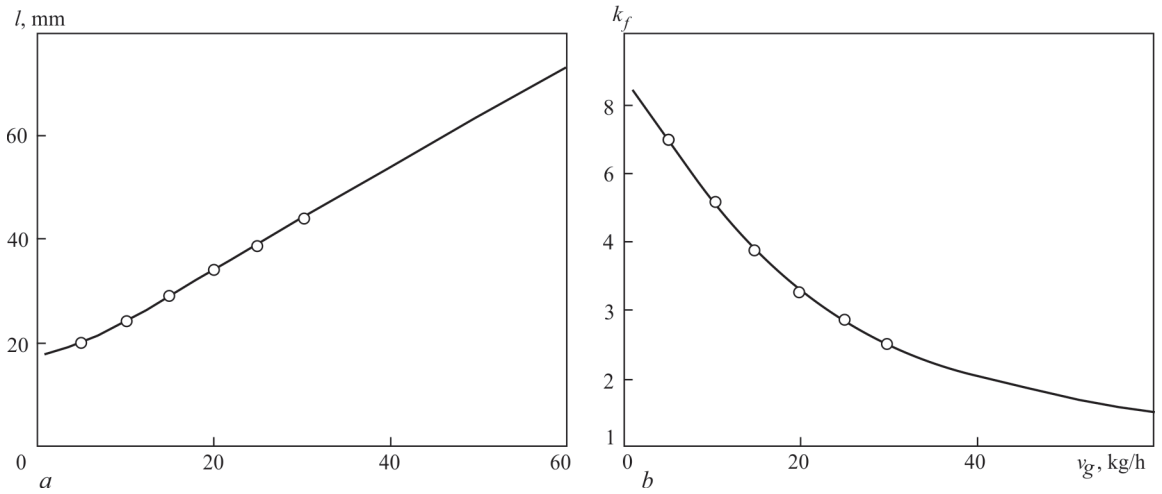

Figure 14. Interpolation dependences on the mass rate of ingot withdrawal v_g: *a* — depth of the liquid metal pool l; *b* — shape coefficient of the liquid metal pool k_f

a macrosection of the template of the upper part of the ingot, cut out in the axial plane and with marked contours of the ingot crystallization fronts on it: solid lines are real contours; dashed lines are calculated contours. In this Figure, the lower crystallization profile, marked with a light solid line, corresponds to the operating mass rate of ingot withdrawal of 20 kg/h.

At the final stage of ingot melting, the melting rate decreases. In Figure 16, two more crystallization profiles are marked with light solid lines, which correspond to the mass withdrawal rate of the ingot at the level of 15 and 10 kg/h. This Figure also shows the calculated light dashed lines of the crystallization profiles for mass rates of 10 kg/h from Figure 13, *b*; 15 from Figure 13, *c* and 20 from Figure 13, *d*. Comparison of the real contours of the ingot crystallization fronts, indicated by solid lines, and the calculated contours of the crystallization fronts, plotted on the figure by light dashed lines, indicates a good coincidence of the front profiles and acceptable accuracy of the results of mathematical modeling for the laminar nature of the melt flow movement.

The macrosection of the lower working area of the ingot (Figure 16) is characterized by the absence of cavities and discontinuities, and the macrostructure of the ingot has crystals close to equiaxed, which is an indice of a high ingot quality. The upper part of the ingot, formed at the final stage of melting and removal of the shrinkage cavity, is characterized by large non-equilibrium crystals, has a different composition of alloying elements due to their evaporation and is not considered to be one that provides an acceptable metal quality. Therefore, it is cut off and remelted during subsequent ingot melting.

Thus, for EBM of titanium alloys in a mould with a diameter of 110 mm, as a result of comparing the calculated profile of the crystallization front of the metal

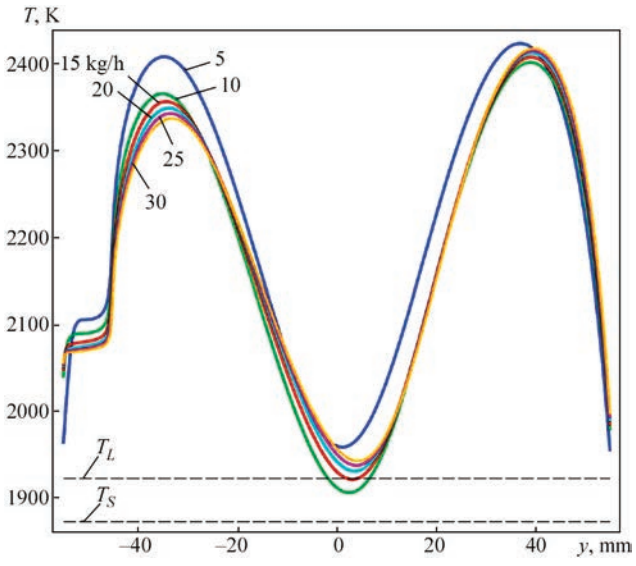

Figure 15. Temperature distribution on the surface of the melt pool (along the y coordinate) in the case of different mass rates of ingot withdrawal, kg/h: 5, 10, 15, 20 (operating mode), 25 and 30

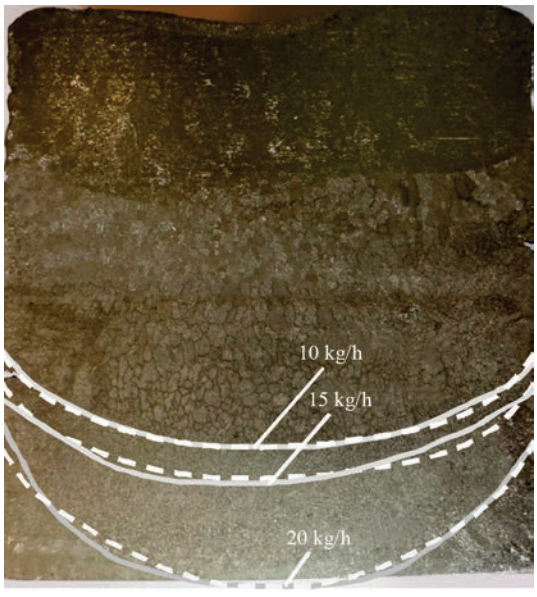

Figure 16. Macrosection of the template of the upper part of the ingot, cut out in the axial plane and with the contours of the ingot crystallization fronts marked on it: solid lines are real contours; dashed lines are calculated contours

in the ingot with the actual crystallization profile of the molten ingot, it was established that the laminar representation of hydrodynamic flows of the liquid metal in the ingot gives a result closer to the real profile than their turbulent representation from [12].

Analysis of the obtained results showed that heat transfer in the liquid phase of the ingot in the laminar mode is mainly predetermined by heat and mass transfer due to the movement of the molten metal, and the power of the electron beam and the type of its coverage of the surface of the pool have a very significant effect on the depth and shape coefficient of the melt pool in the mould.

According to the calculated modes, high-quality ingots with a diameter of 110 mm of medical titanium Ti–6A1–7Nb alloy alloy with a practically homogeneous metal structure were melted at the PWI [30].

Factors that affected the accuracy of the calculations include the simplifications and assumptions used in the development of the mathematical model, which did not significantly affect the overall trends in ingot formation during EBM. Further research should focus on improving the mathematical model with fewer simplifications and assumptions.

Mathematical modeling has made it possible to eliminate the very costly method of sampling to determine technological modes from the preparation for conducting a technological process and is useful and relevant for foundry engineers.

CONCLUSIONS

1. A three-dimensional mathematical model of thermal and stationary laminar hydrodynamic processes based on the Navier–Stokes equations in the melt of a cylindrical ingot has been developed. The ingot is melted by the method of electron beam melting, in which the beam moves along the circumference of the melt pool periphery according to the Gaussian distribution of thermal power from the beam.

2. According to the results of mathematical modeling, the temperature fields and laminar hydrodynamic flows of the molten metal in Ti–6Al–7Nb titanium alloy ingot with a diameter of 110 mm were obtained. The geometry of the two-phase liquidus–solidus zone, which determines the metal crystallization front, was determined. In the case of an electron beam heating power of 16 kW and a mass melting rate of 20 kg/h, such a crystallization front is formed, which provides a practically homogeneous structure of the metal ingot.

3. For the considered system of EBM process for Ti–6Al–7Nb titanium alloy, as a result of comparing the calculated metal crystallization profile in the ingot with a diameter of 110 mm with the crystallization profile of a molten ingot, it was proven that the laminar representation of hydrodynamic flows of the liquid metal in the ingot gives a result closer to the real profile than their turbulent representation.

4. Based on the calculated data, it was found that heat transfer in the liquid phase of the ingot is mainly predetermined by heat and mass transfer due to the movement of the molten metal, and the distribution of the electron beam power on the pool surface has a very significant effect on heat and mass transfer and on the depth of the melt pool.

5. It has been established that a flatter crystallization front of the metal ingot, which is desired, is formed at lower rates of pouring the melt into the mould and, accordingly, lower rates of ingot withdrawal.

REFERENCES

1. Tamayo José, A., Riascos Mateo, Vargas Carlos, A., Baena Libia, M. (2021) Additive manufacturing of Ti6Al4V alloy via electron beam melting for the development of implants for the biomedical industry. *Heliyon*, **7**, 1–26. DOI: DOI: https://doi.org/10.1016/j.heliyon.2021.e06892
2. Mahlobo Mandlenkosi, G.R., Chikosha Lethu, Olubambi Peter, A. (2022) Study of the corrosion properties of powder rolled Ti–6Al–4V alloy applied in the biomedical implants. *J. of Materials Research and Technology*, **18**, 3631–3639. DOI: https://doi.org/10.1016/j.jmrt.2022.04.004
3. Mamoun Fellah, Mohamed Labaïz, Omar Assala et al. (2014) Tribological behavior of Ti–6Al–4V and Ti–6Al–7Nb alloys for total hip prosthesis. *Advances in Tribology*, **July**, 1–13. DOI: https://doi.org/10.1155/2014/451387
4. Bartha, K., Zháňal, P., Stráský, J. et al. (2019) Lattice defects in severely deformed biomedical Ti–6Al–7Nb alloy and thermal stability of its ultra-fine grained microstructure. *J. of Alloys and Compounds*, **788**, 881–890. DOI: https://doi.org/10.1016/j.jallcom.2019.02.173
5. Bolzoni, L., Ruiz-Navas, E.M., Gordo, E. (2017) Evaluation of the mechanical properties of powder metallurgy Ti–6Al–7Nb alloy. *J. of the Mechanical Behavior of Biomedical Materials*, **67**, 110–116. DOI: https://doi.org/10.1016/j.jmbbm.2016.12.005
6. Sun, Y., Huang, B., Puleo, D.A. et al. (2016) Improved surface integrity from cryogenic machining of Ti–6Al–7Nb alloy for biomedical applications. *Procedia CIRP*, **45**, 63–66. DOI: https://doi.org/10.1016/j.procir.2016.02.362
7. Wei Guijiang, Tan Meiying, Attarilar Shokouh et al. (2023) An overview of surface modification, a way toward fabrication of nascent biomedical Ti–6Al–4V alloys. *J. of Materials Research and Technology*, **24**, 5896–5921. DOI: https://doi.org/10.1016/j.jmrt.2023.04.046
8. Oktikawati, A., Riastuti, R., Damisih, D. et al. (2024) Electrochemical characteristic and microstructure of Ti–6Al–7Nb alloy by centrifugal casting for orthopedic implant based on ageing time variations. *Eastern-European J. of Enterprise Technologies*, 2(**12**), 6–15. DOI: https://doi.org/10.15587/1729-4061.2024.302614
9. Hussain Syed Altaf, Manoj Panchal, Viswanath Allamraju K. et al. (2023) Optimization of wear behavior of heat-treated Ti–6Al–7Nb biomedical alloy by response surface methodology. *Environmental Research*, **231**, Pt 2, 116193. DOI: https://doi.org/10.1016/j.envres.2023.116193
10. Biswal, Smrutiranjan, Tripathy, S., Tripathy, D.K. (2024) Optimisation of PMEDM process parameters for Ti–6Al–7Nb biomedical material. *Materials Today: Proceedings*. DOI: https://doi.org/10.1016/j.matpr.2024.02.044

11. Cabrini, M., Carrozza, A., Lorenzi, S. et al. (2022) Influence of surface finishing and heat treatments on the corrosion resistance of LPBF-produced Ti–6Al–4V alloy for biomedical applications. *J. of Materials Processing Technology*, **308**, 117730. DOI: https://doi.org/10.1016/j.jmatprotec.2022.117730
12. Krivtsun, I., Rymar, S., Hubatiuk, R. et al. (2024) Construction of a mathematical model of turbulent heat and mass transfer processes for the case of electron beam melting of titanium alloy casts. *Eastern-European J. of Enterprise Technologies*, *Engineering Technological Systems*, 5(**1**). 110–126. DOI: https://doi.org/10.15587/1729-4061.2024.312561
13. Rubinetti, D., Weiss, D.A., Chaudhuri, A., Kraniotis, D. (2018) Modeling approach to facilitate thermal energy management in buildings with phase change materials. In: *Proc. of Conf. on Comsol 2018, Lausanne, Switzerland*, **7**. https://www.comsol.com/paper/modeling-approach-to-facilitate-thermal-energy-management-with-phase-change-mate-63481
14. Akhonin, S., Pikulin, O., Berezos, V. et al. (2022) Determining the structure and properties of heat-resistant titanium alloys VT3-1 and VT9 obtained by electron-beam melting. *Eastern-European J. of Enterprise Technologies*, 5(**12**), 6–12. DOI: https://doi.org/10.15587/1729-4061.2022.265014
15. Akhonin, S.V., Pikulin, O.M. (2019) Investigation of effect of electron beam surface treatment of titanium alloy ingots on structure and properties of melted metal. In: *Proc. of IOP Conf. on Series: Materials Science and Engineering*, 582 **(1)**, 012047. DOI: https://doi.org/10.1088/1757-899x/582/1/012047
16. Berezos, V.O., Akhonin, D.S. (2023) Electron beam melting of titanium alloys for medical purposes. *The Paton Welding J.*, **6**, 41–48. DOI: https://doi.org/10.37434/tpwj2023.06.06
17. Akhonin, S.V., Berezos, V.O., Bondar, O.I. et al. (2021) Mathematical modeling of hydrodynamic and thermal processes during the crystallization of titanium ingots EBM. *Suchasna Elektrometalurhiya*, **1**, 27–34 [in Ukrainian]. DOI: https://doi.org/10.37434/sem2021.01.03
18. Akhonin, S.V., Gorislavets, Yu.M., Gluhenkyi, A.I. et al. (2019) Modeling of hydrodynamic and thermal processes in the mould in cold-hearth electron beam melting. *Suchasna Elektrometalurhiya*, **4**, 9–17 [in Russian]. DOI: https://doi.org/10.15407/sem2019.04.02
19. Akhonin, S.V., Krivtsun, I.V., Berezos, V.O. et al. (2024) Mathematical modeling of heat and mass transfer processes of electron beam melting of ingots from high-strength titanium alloys. In: *Proc. of VII Inter. Conf. on Welding and Related Technologies, 7–10 October 2024, Yaremche, Ukraine. Kyiv*, 119–124, Kyiv, International Association «Welding». DOI: https://doi.org/10.1201/9781003518518-25
20. Ben-David, O., Levy, A., Mikhailovich, B., Azulay, A. (2013) 3D numerical and experimental study of gallium melting in a rectangular container. *Inter. J. of Heat Mass Transfer*, **67**, 260–271. DOI: http://dx.doi.org/10.1016/j.ijheatmasstransfer.2013.07.058
21. Heat Transfer Module User's Guide. Version: Comsol 5.4. http://www.comsol.com
22. Versteeg, H.K., Malalasekera, W. (2007) *An introduction to computational fluid dynamics. The finite volume method*. Harlow, Pearson Prentice Hall.
23. Avnaim, M.H., Levy, A., Mikhailovich, B. et al. (2016) Comparison of three-dimensional multidomain and single-domain models for the horizontal solidification problem. *J. of Heat Transfer*, 138(**11**), 112301-1–112301-11. DOI: https://doi.org/10.1115/1.4033700
24. Truong Van-Doi, Yong-Taek Hyun, Jong Woo Won et al. (2022) Numerical simulation of the effects of scanning strategies on the aluminum evaporation of titanium alloy in the electron beam cold hearth melting process. *Materials,* **15**. DOI: https://doi.org/10.3390/ma15030820
25. Yao Lu, Maijer Daan M., Cockcroft Steve L. et al. (2018) Quantification of heat transfer phenomena within the melt pool during the plasma arc remelting of titanium alloys. *Inter. J. of Heat and Mass Transfer*., **126**, 1123–1133. DOI: https://doi.org/10.1016/j.ijheatmasstransfer.2018.06.051
26. Belyaev, N.M. (1989) *Fundamentals of Heat Transfer*. Kyiv, Vyshcha Shkola [in Russian].
27. Mills, K. (2002) *Recommended values of thermophysical properties for selected commercial alloys*. Woodhead publishing Limited.
28. Efimov, A.I., Belorukova, L.P., Vasilkova, I.V., Chechev, V.P. (1983) *Properties of inorganic compounds. Directory*. Leningrad, Khimiya.
29. Langmuir, I. (1913) The vapor pressure of metallic tungsten. *Physical Review*, 2**(5)**, 329–342. DOI: https://doi.org/10.1103/physrev.2.329
30. Berezos, V.O., Akhonin, D.S. (2023) Electron beam melting of titanium alloys for medical purposes. *The Paton Welding J.*, **6**, 41–48. DOI: https://doi.org/10.37434/tpwj2023.06.06

ORCID
I.V. Krivtsun: 0000-0001-9818-3383,
S.V. Rymar: 0000-0003-0490-4608,
R.S. Gubatyuk: 0000-0002-0851-743X,
V.O. Berezos: 0000-0002-5026-7366,
D.S. Akhonin: 0009-0000-2054-4054,
R.V. Selin: 0000-0002-2990-1131

CONFLICT OF INTEREST
The Authors declare no conflict of interest

CORRESPONDING AUTHOR
S.V. Rymar
E.O. Paton Electric Welding Institute of the NASU
11 Kazymyr Malevych Str., 03150, Kyiv, Ukraine.
E-mail: elmag@paton.kiev.ua

SUGGESTED CITATION
I.V. Krivtsun, S.V. Rymar, R.S. Gubatyuk, V.O. Berezos, D.S. Akhonin, R.V. Selin (2025) Mathematical modeling of heat and mass transfer processes during electron beam melting of Ti–6Al–Nb titanium alloy ingots. *The Paton Welding J.*, **9**, 18–32.
DOI: https://doi.org/10.37434/tpwj2025.09.03

JOURNAL HOME PAGE
https://patonpublishinghouse.com/eng/journals/tpwj

Received: 24.06.2025
Received in revised form: 12.08.2025
Accepted: 18.09.2025

DOI: https://doi.org/10.37434/tpwj2025.09.04

EFFECT OF MODES OF ELECTRON BEAM TREATMENT OF POWDER BLANKS FROM HARD ALLOYS ON FORMATION OF THE MICROSTRUCTURE AND PROPERTIES OF SINTERED PRODUCTS

M.O. Sysoiev[1], **V.M. Nesterenkov**[1], **V.M. Bondar**[2], **H.P. Kysla**[3]

[1]E.O. Paton Electric Welding Institute of the NASU
11 Kazymyr Malevych Str., 03150, Kyiv, Ukraine
[2]East Ukrainian Volodymyr Dahl National University
17 John Paul II Str., 01042, Kyiv, Ukraine
[3]PlasmaTec LLC
18 Pravednykiv Svitu Str., 21036, Vinnytsia, Ukraine

ABSTRACT

The results of the study of the influence of the cooling rate on the structure and properties of the VK8 hard alloy produced by the electron beam sintering method are presented. The use of an electron beam provides high controllability of the heat treatment processes, which allows regulating the cooling rate of hard alloy specimens. The tungsten carbide powder produced by PlasmaTec LLC by a chemical method from secondary raw materials was used in the work. The presence of two phases — tungsten carbide and a cobalt-based β-solid solution was revealed by metallographic and X-ray analysis methods. There is no η-phase, free carbon or pores in the structure. It is shown that tungsten carbide crystals grow with an increase in cooling time. In terms of hardness and crack resistance, hard alloys produced by the electron beam sintering method are not inferior to hard alloys produced by the conventional technologies.

KEYWORDS: hard alloy, electron beam sintering, tungsten carbide, cooling rate, grain size

INTRODUCTION

Hard alloys are a group of materials that have high hardness, wear resistance and are indispensable in certain operating conditions. Among them, tungsten carbide-cobalt (WC–Co) alloys are most widely used in conditions of intensive wear. This is predetermined by a unique combination of mechanical properties, such as high hardness (82–92 *HRA*, which exceeds the hardness of high-speed steel), wear resistance, fracture toughness and compressive strength. In addition, WC–Co alloys provide high corrosion resistance. The binder content, size and distribution of tungsten carbide particles are critical factors affecting the mechanical properties of WC–Co cermet [1, 2].

Nowadays, hard alloys are significantly superior to other materials in terms of their use for the manufacture of various types of metal-cutting, deforming and drilling tools, as well as for the manufacture of parts of machines and equipment that are operated under conditions of intensive wear and under the influence of high temperatures and loads. The service properties of hard alloys depend both on the properties and ratio of the source powders and on the technology of manufacturing products.

There are many methods for producing hard alloys: sintering in a vacuum or gas environment [3–5]; vacuum compression sintering [6]; hot isostatic pressing [7]; electric discharge or spark plasma sintering (SPS) [8]; microwave sintering [9]; high-frequency induction heat sintering (HFIHS) [10]. The most widely used method for producing hard alloy parts is furnace sintering.

During conventional furnace sintering of hard alloys, when a liquid phase appears, intensive growth of carbide grains is observed [11], which is predetermined by the process of recrystallization of tungsten carbide through the liquid phase, as well as "coalescence" — the growth of neighbouring WC grains due to the coincidence of their crystallographic planes when these grains are displaced [12]. Electron beam technology, which is currently used in the additive manufacturing of WC–Co hard alloys [13, 14], can provide high sintering rates, and also, due to the controllability of the process itself, provides a sufficiently "fine" control of the alloy microstructure.

THE AIM

of this study is to determine the influence of electron beam modes of sintering powder hard alloy mixtures of the WC–Co system, namely their cooling rate, on the formation of the microstructure and properties of consolidated blanks.

MATERIALS AND RESEARCH METHODS

As the source materials, tungsten carbide was used produced by treatment of secondary raw materials

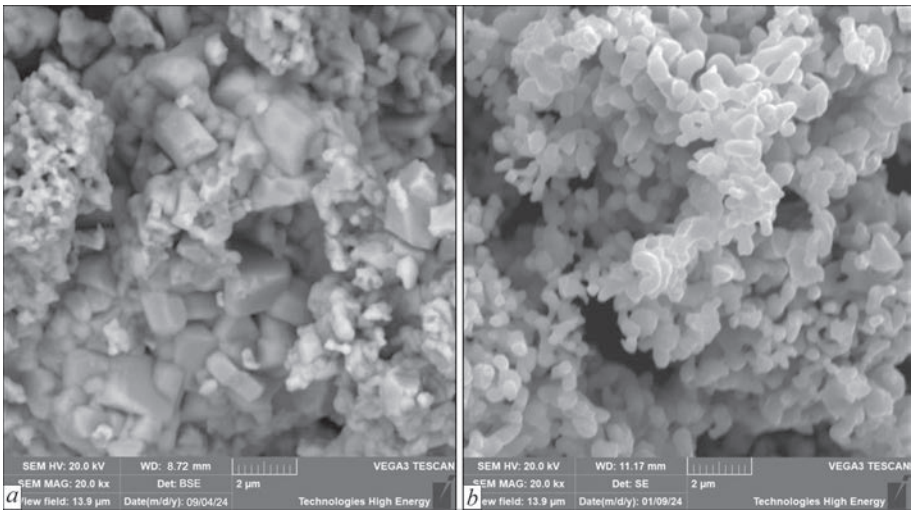

Figure 1. Source powders: *a* — tungsten carbide; *b* — cobalt

using chemical technology improved by PlasmaTec LLC; cobalt powder (8 wt.%) of China production. To study the morphology of the powders, the microstructure of the specimens and determine their chemical composition, a Tescan Vega 3 SBH EasyProbe scanning electron microscope with a Bruker Quantax 610 energy-dispersive X-ray microanalyzer was used. The carbon content of tungsten carbide powder was determined in a LECO C744 carbon determination device. Phase analysis was performed in an Inel EQUINOX 1000 diffractometer. Rockwell hardness (*HRA*) was measured in a NOVOTEST TC–P–C hardness tester, Vickers hardness and crack resistance were measured in an Innovatest hardness tester, and density was determined by hydrostatic weighing in an ANG220 analytical balance.

The morphology of the source tungsten carbide and cobalt powders is shown in Figure 1. The size of tungsten carbide powder particles is 0.5–3.0 μm and cobalt is 0.2–1.0 μm. The total carbon content in tungsten carbide is 6.2 %, the phase composition of the powder corresponds to tungsten monocarbide (WC).

Compacts with a diameter of 8 mm and a length of 30 mm were manufactured using conventional technology. Driving off the plasticizer and preliminary sintering took place in a hydrogen environment at a temperature of 1150 °C. Electron beam sintering was carried out using the modes shown in Figure 2. The

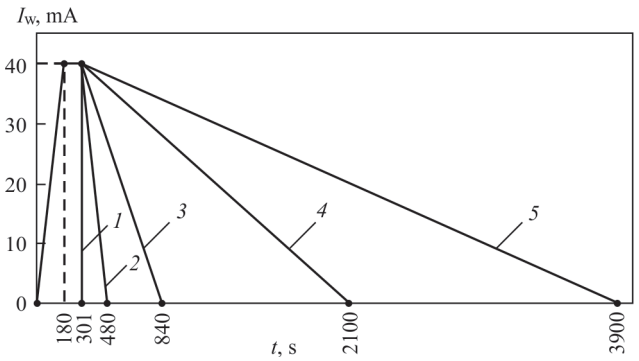

Figure 2. Modes of electron beam sintering of WC–Co specimens

specimens were heated to the sintering temperature (1400±20 °C) by a gradual increase in the beam current from 0 to 40 mA for 3 min, holding for 2 min, and cooling the specimens in five modes: *1* — switching off the electron beam; *2* — decreasing the electron beam current from 40 to 0 mA for 3 min; *3* — 9; *4* — 30; *5* — 60. In this case, the cooling rate from the sintering temperature (1400 °C) to 500 °C was: for mode *1* — 80–100 °C/s; *2* — 5–10; *3* — 2–5; *4* — 0.5–1.0; *5* — 0.2–0.5. Further cooling (from 500 °C to room temperature) occurred due to convection.

INSTALLATION FOR ELECTRON BEAM SINTERING

To study the influence of sintering modes on the formation of the microstructure and properties of VK8 alloys, industrial SV 229 installation was used, specially developed by order of PlasmaTec LLC at the PWI for electron beam treatment (EBT) of blanks from powder materials based on tungsten carbide and cobalt (WC–Co). The installation (Figure 3) is designed for electron beam sintering of blanks with a cylindrical outer surface, an initial diameter of 6–80 mm and a length of up to 30 mm. The basic configuration of the installation provides fixation for only three standard sizes of blanks (diameter and length, respectively): 30×30, 25×25 and 15×15 mm.

The vacuum chamber with a volume of about 0.5 m^3 of the installation (*1*, Figure 3) is made of stainless steel, the walls and door of the chamber are cooled by water. The thickness of the walls of the chamber and door provides both mechanical strength and biological protection of the operating personnel from X-ray radiation. The chamber is equipped with an inspection port-hole (*2*, Figure 3) for visual observation of sintering processes, as well as a high-temperature OPTRIS CTratio 2M pyrometer (temperature measurement range 550–3000 °C) and a video camera for general observation. An electron beam gun unit is installed on the upper wall of the chamber (*3*, Figure 3). The

triode-type welding gun is equipped with electronic optics, a cathode, an anode and a control electrode (venelt); the electron beam current is up to 200 mA. The gun design is compact and easy to maintain.

The rear wall of the chamber has a flange with an internal diameter of 400 mm for connecting a vacuum system. The vacuum system (*4*, Figure 3) of the installation is assembled from components of well-known manufacturers Leybold, Pfeiffer and Ebara. The performance of the vacuum system of the installation is sufficient to create a pressure in the vacuum chamber of $2 \cdot 10^{-4}$ mbar and, accordingly, $5 \cdot 10^{-5}$ mbar in the gun in about 15 min.

The operator's workplace is located to the right of the vacuum chamber in front of the control cabinet (*5*, Figure 3). To the right of the control cabinet is the power cabinet (*6*, Figure 3) with the vacuum system control equipment and the SIEMENS Sinamics S120 system control elements. Further to the right is the cabinet of the 15 kW/60 kV inverter type welding high-voltage power source (*7*, Figure 3).

The EBT technological cycle involves a feed drum for parts (*8*, Figure 3); a mechanism for working rotation of parts (rotator), on which EBT is directly performed; a mechanism for longitudinal feeding of parts when loading them onto and unloading them from the rotator, and a bottom-plate for treated parts. The main technical characteristics of the SV 229 installation are given below.

Characteristics of electron beam equipment

Overall dimensions of the welding installation, mm:
- length . . . 3500
- width . . . 5000
- height . . . 2300

Internal dimensions of the vacuum chamber, mm:
- length . . . 800
- width . . . 750
- height . . . 850

Weight of the installation, kg . . . 6000
Working vacuum in the vacuum chamber, mbar, not worse than . . . $2 \cdot 10^{-4}$
Pumping time of a clean, dry and empty vacuum chamber to working vacuum, min, not more than . . . 15
Working vacuum in the welding gun, mbar, not worse than . . . $5 \cdot 10^{-5}$
Inleakage into a clean, empty and dry vacuum chamber, mbar·l/s, not more than . . . $2 \cdot 10^{-3}$
Mechanism for rotation of parts:
- rotation frequency for a part with a diameter of 30 mm, rps . . . 0.5–3

Mechanism for feeding parts:
- maximum linear displacement of a part, mm . . . 300
- precision of linear displacement of a part, mm . . . ±0.25

Electron beam gun and inverter type high-voltage source:
- capacity of high-voltage power source, kW . . . 12
- rated accelerating voltage, kV . . . 60
- stability of accelerating voltage, % . . . ±0.15
- electron beam current (with a change step of 0.1 mA), mA . . . 0.5–200
- stability of beam current according to ISO 14744-1, % , max . . . ±1
- working range of adjustment of the focal length of the electron beam, mm . . . 500–600
- electron beam deflection angle, deg . . . ±3.5
- focusing lens current stability according to ISO 14744-1, % , max . . . ±0.5

Guaranteed cathode operating time, h . . . 50
Water cooling system:
- autonomous closed system based on a chiller . . . included

General technical requirements:
- power supply (according to German standard DIN EN 60 204, p. 4.3) . . . 380 V, 50/60 Hz
- power consumption, kV·A, max . . . 55
- separate grounding . . . <2 Ohm; 35 mm^2
- room temperature, °C . . . 15–25
- relative humidity (at 25 °C), %, max . . . 70
- compressed air pressure, kg/cm^2, min . . . 5
- compressed air cleanliness class (according to ISO 8573-1: 2010) . . . 7:4:4

Figure 3. SV 229 installation for electron beam treatment: *1* — vacuum chamber; *2* — inspection port-hole; *3* — electron beam gun; *4* — vacuum system; *5* — control cabinet; *6* — power cabinet; *7* — cabinet of high-voltage welding power source; *8* — loading device for feed drums of parts

The use of an electron beam makes it possible to regulate the heating and cooling rates, which ensures control over the sintering process and, as a result, control over the structure of the produced parts.

RESEARCH RESULTS

Cooling after sintering of hard alloys of the WC–Co system leads to the emergence of a stressed state, which is predetermined by the difference in the coefficients of thermal expansion of the phase components. The coefficient of thermal expansion of cobalt is almost three times higher than that of tungsten carbide, therefore, during cooling at the sintering process, compressive stresses arise in tungsten carbide, the magnitude of which can reach 1000 MPa, and in cobalt, respectively, tensile stresses arise up to 2000 MPa [15]. It is characteristic that the magnitude of these stresses is influenced by the ratio of phase components, and an increase in the cobalt content to 12 % leads to a decrease in tensile stresses in it by 3–4 times. An increase in the cooling rate after sintering leads to a significant increase in stresses and, accordingly, affects

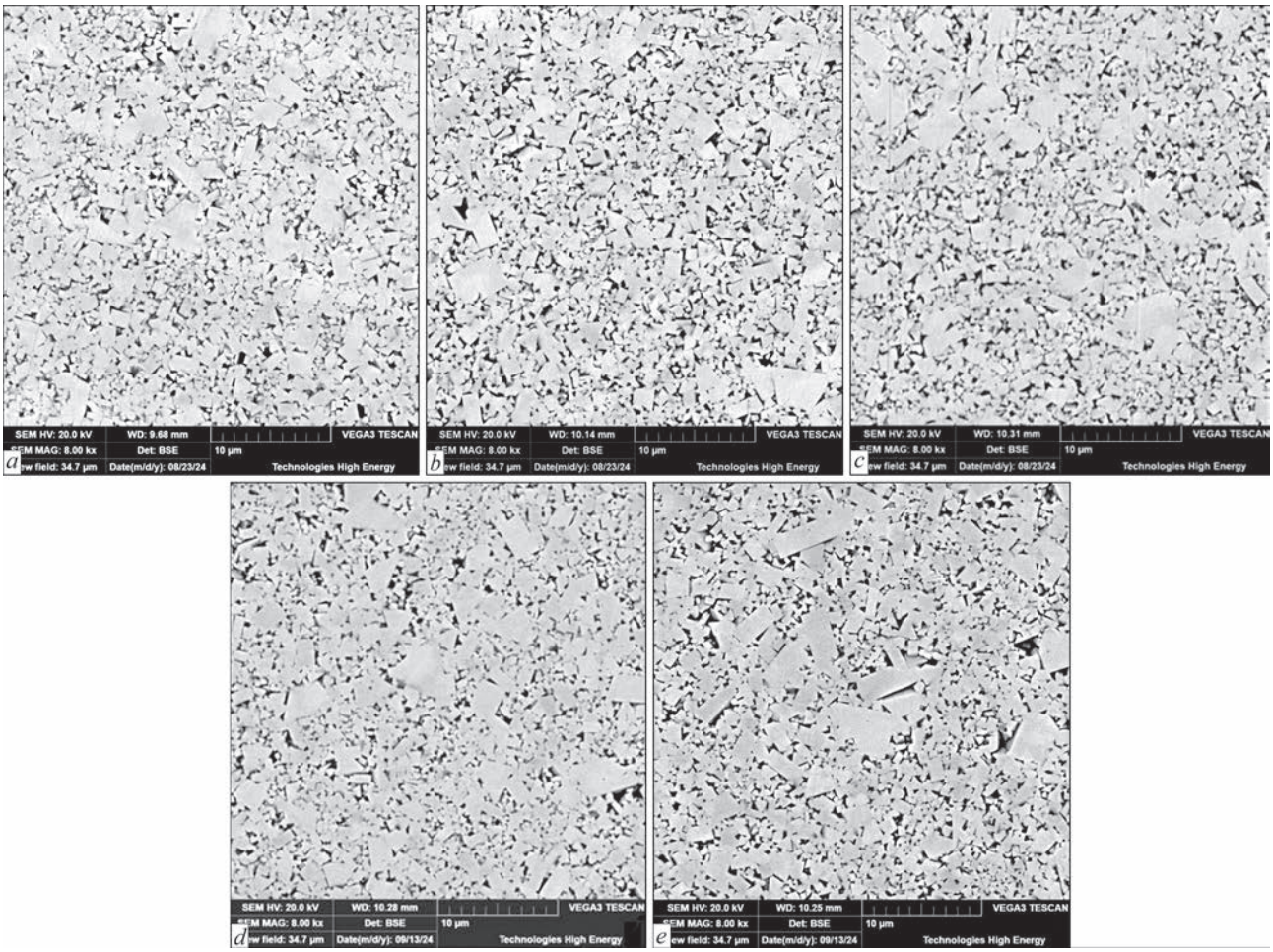

Figure 4. Microstructures of sintered specimens produced at different cooling rates: *a* — cooling time 1 s; *b* — 3 min; *c* — 9; *d* — 30; *e* — 60

the properties of hard alloys [15]. The density of the produced specimens was determined by hydrostatic weighing to be 14.75–14.8 g/cm^3. The sintered specimens were cut along the cylinder and examined using scanning electron microscopy (Figure 4).

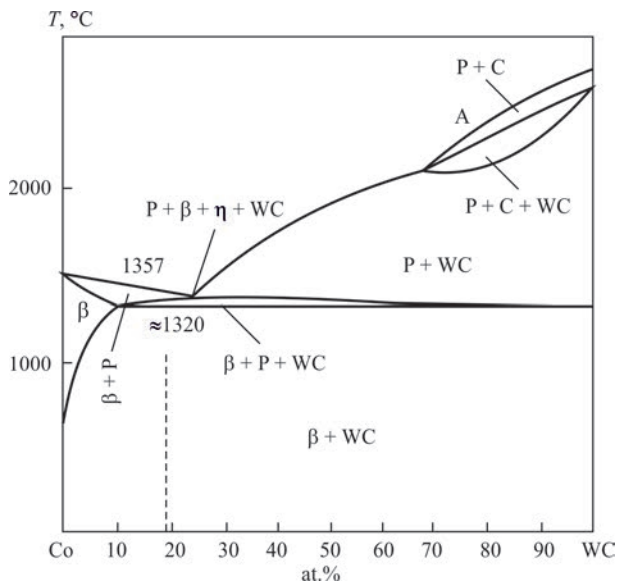

Figure 5. Vertical section of the W–C–Co ternary diagram [11]

According to the quasi-binary section (Figure 5) of the W–C–Co ternary state diagram, the liquid phase is formed at the melting point of the double eutectic, which is about 1320 °C.

At temperatures of electron beam treatment of specimens above 1340 °C, intensive shrinkage of the blanks is observed. Complete densification is achieved quite quickly within ≈ 1 min. Such rapid shrinkage is predetermined by the appearance of a liquid phase. In the first moments of sintering, after the formation of a liquid phase, the movement of tungsten carbide grains occurs under the action of surface tension forces.

The microstructure of the produced specimens is formed in the form of a cobalt matrix, which contains faceted tungsten carbide grains. In specimens with a minimum cooling time, as well as cooled for 3 and 9 min, the structure is identical, no noticeable growth of tungsten carbide grains is observed (0.5–4.0 μm). During cooling for 30 and 60 min, the growth of tungsten carbide grains to 6–10 μm is observed (Figure 6). The driving force for the growth of WC grains during sintering is the minimization of interfacial energy, and therefore, it is proportional to the specific area of the WC and cobalt grain boundary. Since both fine (0.2 μm) and coarser grains (3 μm) are present in

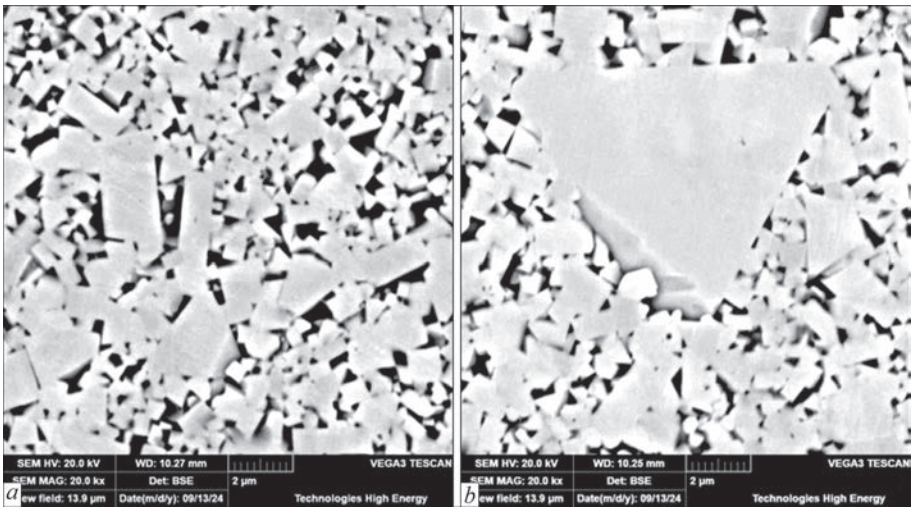

Figure 6. WC grains grown during cooling for: *a* — 30; *b* — 60 min

the source tungsten carbide powder, according to the Gibbs–Thomson effect, when a liquid phase is formed, fine WC grains dissolve in it (due to their high surface energy) with subsequent precipitation on coarse, more stable grains, which leads to their growth. Thus, the recrystallization process includes: 1 — dissolution of fine particles (transition of atoms from the particle surface into the melt); 2 — diffusion of atoms in the liquid; 3 — precipitation of the solved substance on coarse grains.

In addition to grain growth, "coalescence" of grains occurs due to their slight displacement relative to each other and fusion due to the coincidence of identical crystallographic planes.

That is, increasing the cooling time leads to an increase in the amount of coarse carbide grains and the formation of continuous contacts between them. The driving force for this stage is the reduction of the surface energy of the boundaries of carbide particles. To prevent the growth of tungsten carbide grains, growth inhibitors such as chromium and vanadium carbide are most often used, which are added to the source charge in an amount of up to 0.5 % [16].

When studying the influence of cooling time on the mechanical properties of hard alloy specimens, the hardness and crack resistance of the produced materials were determined. The research was carried out by the indentation method with a load on the indenter of 30 kg, the results are given in Table 1. Table 2 shows the properties of hard alloys from foreign manufacturers.

It is typical for the produced specimens that with an increase in the cooling time, a decrease in the hardness of the specimens and a decrease in the crack resistance are observed. This behaviour can be explained as follows: tungsten and carbon, which dissolve in the liquid phase during sintering of the hard alloy, do not have time to crystallize in the form of tungsten carbide at a high cooling rate. Then the cobalt metal matrix is essentially a solid solution, which causes additional stresses in the material and prevents the crack from propagating during indentation. As the cooling time grows, the amount of solid solution decreases, and accordingly the crack resistance decreases. To establish

Table 1. Hardness and crack resistance of hard alloys with different cooling times

Cooling time, min	*HRA*	K_{1C}, MPa·m$^{1/2}$	HV_{30}, GPa
0	89.5–90.7	18.6	15.5
3		17.2	15.6
9		18.5	15.6
30		15.2	15.7
60		16.8	14.1

Table 2. Properties of hard alloys of foreign manufacturers

Manufacturer	Binding content, %	*HRA*	K_{1C}, MPa·m$^{1/2}$	HV_{30}, GPa
Ceratizit, CTF12	6	92.1	9.9	16.2
Ceratizit, CTM17	8.5	90.4	11.3	14
Ceratizit, CTE20	10	87.6	18	11.2
Taegutec, UF10	10	92	14.7	16
Mitsubishi, GTi15	8	90	14.7	–

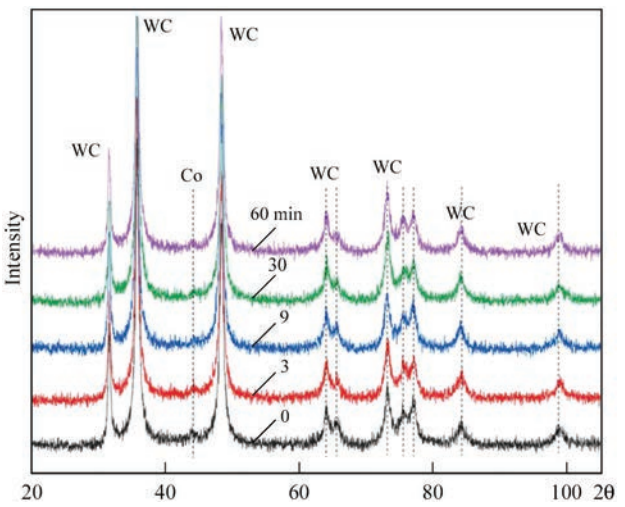

Figure 7. Diffraction patterns obtained from specimens of hard alloy of WC–8Co composition with different cooling times

the phase composition, X-ray diffraction studies were performed. The diffraction patterns of the produced specimens are shown in Figure 7.

As is seen from the obtained results, the diffraction maxima from WC for all specimens are symmetrically located relative to each other, displacement of peaks is not observed. For cobalt, a diffraction maximum is determined, corresponding to a cubic lattice. The η-phase and free carbon were not revealed by X-ray phase analysis.

CONCLUSIONS

It is shown that the use of electron beam heating provides the production of hard alloy specimens whose characteristics are not inferior to world analogues produced by hot pressing and compression sintering methods.

Microstructural examinations have shown that with an increase in cooling time, the range of tungsten carbide grain sizes grows from 0.4–4.0 to 0.4–10.0 μm.

It has been experimentally determined that variation in the cooling time of the specimens affects the micromechanical characteristics of the hard alloy. The crack resistance of the hard alloy material produced by electron beam treatment is 18.6 MPa $m^{1/2}$, while for specimens, similar in chemical and granulometric composition produced by compression sintering, it is about 14 MPa·$m^{1/2}$.

REFERENCES

1. Upadhyaya, G.S. (2001) Materials science of cemented carbides — An overview. *Materials & Design*, 22(**6**), 483–489. DOI: https://doi.org/10.1016/S0261-3069(01)00007-3
2. Zak Fang, Xu Wang, Taegong Ryu et al. (2009) Synthesis, sintering and mechanical properties of nanocrystallaine cemented tungsten carbide — A review. *Inter. J. of Refractory Metals and Hard Materials*, 27(**2**), 288–299. DOI: https://doi.org/10.1016/j.ijrmhm.2008.07.011
3. Falkovsky, V.A., Klyachko, L.I. (2005) *Hard alloys*. Moscow, Publ. House Ruda i Metally [in Russian].
4. Kharchenko, O.V., Prokopiv, M.M., Serdyuk, Yu.D. (2010) Structure of hard alloys of the WC–Co group after aggregation in a gaseous medium. *Sverkhtviordye Materialy*, **2**, 96–98 [in Ukrainian].
5. Bondarenko, V.P., Pavlotskaya, E.G. (1995) *Sintering of tungsten hard alloys in a precision-controlled gas environment.* Kyiv, Naukova Dumka [in Russian].
6. Chen, H., Zwang, D., Li, Y., Chen, J. (2001) High performance sinter — HIP for hard metals. In: *Proc. of 15 Inter. Plansee Seminar*, *Reutte, Austria*, **2**, 180–188.
7. Chongbin Wei, Xiaoyan Song, Shixian Zhao et al. (2010) In-situ synthesis of WC–Co composite powder and densification by sinter-HIP. *Inter. J. of Refractory Metals and Hard Materials*, 28(**5**), 567–571. DOI: https://doi.org/10.1016/j.ijrmhm.2010.04.002
8. Kui Liu, Zhenhua Wang, Zengbin Yin et al. (2018) Effect of Co content on microstructure and mechanical properties of ultrafine grained WC–Co cemented carbide sintered by spark plasma sintering. *Ceramics Inter.*, 44(**15**), 18711–18718. DOI: https://doi.org/10.1016/j.ceramint.2018.07.100
9. Breval, E., Cheng, J.P., Agrawal, D.K. et al. (2005) Comparison between microwave and conventional sintering of WC/Co composites. *Materials Sci. and Eng.: A*, 391(**1–2**), 285–295. DOI: https://doi.org/10.1016/j.msea.2004.08.085
10. Hwan-Cheol Kim, In-Jin Shon, In-Kyoon Jeong et al. (2007) Rapid sintering of ultrafine WC and WC–Co hard materials by high-frequency induction heated sintering and their mechanical properties. *Metals and Materials Inter.*, **13**, 39–45. DOI: https://doi.org/10.1007/BF03027821
11. Chaporova, I.N., Chernyavsky, K.S. (1975) *Structure and properties of sintered hard alloys.* Moscow, Metallurgiya [in Russian]
12. Farag, S., Konyashin, I., Ries, B. (2018) The influence of grain growth inhibitors on the microstructure and properties of submicron, ultrafine and nano-structured hardmetals — A review. *Inter. J. of Refractory Metals and Hard Materials*, **77**, 2–30. DOI: https://doi.org/10.1016/j.ijrmhm.2018.07.003
13. Atefeh, A., Javad, R.S.M., Zohreh, S., Filippo, B. (2020) A review of additive manufacturing of cermets. *Additive Manufacturing*, **33**, 101130. DOI: https://doi.org/10.1016/j.addma.2020.101130
14. Yang,Y.K., Zhang, C.Q., Wang, D.Y. et al. (2020) Additive manufacturing of WC–Co hardmetals: A review. *The Inter. J. of Advanced Manufacturing Technology*, **108**, 1653–1673. DOI: https://doi.org/10.1007/s00170-020-05389-5
15. Loshak, M.G. (1986) *Strength and durability of hard alloys*. Kyiv, Naukova Dumka [in Russian].
16. Farag, S., Konyashin, I., Ries, B. (2018) The influence of grain growth inhibitors on the microstructure and properties of submicron, ultrafine and nano-structured hardmetals — A review. *Inter. J. of Refractory Metals and Hard Materials*, **77**, 12–30. DOI: https://doi.org/10.1016/j.ijrmhm.2018.07.003

ORCID

M.O. Sysoiev: 0000-0001-7243-2388,
V.M. Nesterenkov: 0000-0002-7973-1986,
V.M. Bondar: 0009-0008-3814-214X,
H.P. Kysla: 0000-0003-0791-6903

CONFLICT OF INTEREST

The Authors declare no conflict of interest

CORRESPONDING AUTHOR

M.O. Sysoiev
E.O. Paton Electric Welding Institute of the NASU
11 Kazymyr Malevych Str., 03150, Kyiv, Ukraine.
E-mail: sysoiev.maksym@tve.com.ua

SUGGESTED CITATION

M.O. Sysoiev, V.M. Nesterenkov, V.M. Bondar, H.P. Kysla (2025) Effect of modes of electron beam treatment of powder blanks from hard alloys on formation of the microstructure and properties of sintered products. *The Paton Welding J.*, **9**, 33–38. DOI: https://doi.org/10.37434/tpwj2025.09.04

JOURNAL HOME PAGE

https://patonpublishinghouse.com/eng/journals/tpwj

Received: 28.04.2025
Received in revised form: 03.06.2025
Accepted: 16.09.2025

DOI: https://doi.org/10.37434/tpwj2025.09.05

INFLUENCE OF PULSE PLASMA TREATMENT ON WEAR RESISTANCE OF 40Kh STEEL SURFACE LAYERS

O.V. Kolisnichenko[1], V.M. Korzhyk[1], C. Senderowski[2], D.V. Strogonov[1], O.V. Hanushchak[1], O.S. Tereshchenko[1]

[1]E.O. Paton Electric Welding Institute of the NASU
11 Kazymyr Malevych Str., 03150, Kyiv, Ukraine
[2]Warsaw University of Technology, Mechanics and Printing Institute,
Narbutta 85, 02-524, Warszawa, Poland

ABSTRACT

The paper studies the effect of pulse plasma treatment on the physical and mechanical properties of 40Kh steel. The structural and phase changes were studied in the surface layers using metallographic and X-ray phase analysis. Cyclic action and high heating and cooling rates in the surface layers lead to a change in the kinetics of phase transformations, generation of inhomogeneous distortions of the crystal lattice as a result of phase strain hardening, a decrease in the dispersion of the structure, formation of an increased dislocation density, etc. Tribological tests for wear resistance were carried out under fluid friction conditions at various loads and sliding speeds. Comparative data on the extent of linear wear and wear intensity of the test samples were obtained.

KEYWORDS: pulse plasma treatment, structural alloy steel, structural phase analysis, hardness, microstructure, friction pair, wear

INTRODUCTION

One of the pressing and actively studied problems in the field of mechanical engineering is the improvement of reliability and durability of friction units. Machine components operating in friction pairs under conditions of intensive wear, cyclic loads, and vibrations are subject to special requirements for the wear resistance of the friction surface, while simultaneously ensuring high dynamic strength of the entire product. In this sense, the development of new and the improvement of existing technological methods of surface treatment of materials and machine components appears highly promising. These include various coating methods, ranging from ion-plasma to gas-thermal spraying; methods of alloying, chemical-thermal treatment, or implantation of surface layers with strengthening elements; and different methods of thermomechanical surface treatment, among others. Perhaps one of the most extensively studied directions in strengthening surface layers of different machine parts and assemblies is the treatment of materials with concentrated energy sources (CES) [1–4]. Electron beam, laser energy sources, or plasma jets are predominantly used as CES.

During exposure to concentrated energy sources, the surface is heated followed by cooling due to heat dissipation both into the material and the environment, resulting in structural-phase transformations in the surface layer. The nature of the heating source, heat flux, and exposure time of the surface affect the properties of the thermally strengthened layer (its thickness, physical and mechanical characteristics, phase composition, and dispersion). High-speed heating methods are always characterized by insufficient time for the running and completion of equilibrium structural transformations. Due to changes in the kinetics of phase transformations, grain refinement, and the formation of increased dislocation density under conditions of high-speed heat treatment of the materials, it is possible to obtain the required set of mechanical and physical properties of material surfaces (such as high hardness, wear resistance, corrosion resistance etc.). Heating using CES can be carried out in both continuous and pulsed modes [5]. Compared to conventional heat treatment methods, the pulsed CES heating mode is applied over a very short period (approximately 10^{-3}–10^{-6} s). As a result of intensive heat removal into the metal and the surrounding environment, the cooling time is also several orders of magnitude shorter (10^{-3}–10^{-6} s) than during conventional cooling in liquid quenching media.

In addition, the use of CES proves to be highly effective for carrying out thermal-cyclic treatment of metals and machine components. After such treatment, the surface layer acquires a fine-dispersed structure. It is well known that, at equal hardness, steel with a fine-grained structure has significantly better wear resistance than coarse-grained steel, since the latter demonstrates lower resistance to brittle fracture [6]. As tools for implementing pulsed thermal-cyclic treatment of parts, in addition to laser and electron beam devices, plasma generators

based on powerful pulsed electrical discharges are effectively employed [7, 8]. At the PWI, one variant of such generators was developed and is successfully applied as research equipment both in scientific laboratories [9, 10] and in industrial settings [11].

THE AIM

of this study is to investigate the effect of pulsed plasma treatment (PPT) on structural-phase changes in surface layers and on their wear resistance under lubricated friction conditions.

EQUIPMENT, MATERIALS, AND RESEARCH METHODS

Steel 40Kh (AISI 5140) was selected as the material for investigation. Its chemical composition is as follows, wt.%: C — 0.36–0.44; Si — 0.17–0.37; Mn — 0.50–0.80; Cr — 0.8–1.10, balance — Fe. Steel 40Kh is characterized by increased strength, hardness, and wear resistance. It is widely used across various industrial sectors for manufacturing components and parts operating under high loads, such as shafts, gears, axles, gear wheels, etc. Owing to its mechanical properties, 40Kh steel is also applied in the automotive, mechanical engineering, shipbuilding, and energy industries, where a reliable and durable material is required.

For the study of the structural-phase state of surface layers, a series of samples of steel 40Kh sized 15×15×10 mm was prepared. Tribological experiments were carried out on bushings (Figure 1). A disk with a diameter of 90×10 mm made of ShKh15 steel was used as a counterbody.

The hardness of steel 40Kh in its initial (as annealed) state was measured using the Brinell method and found to be 212–217 *HB*. Before PPT, the samples underwent standard heat treatment. An electric furnace was used for heating, quenching, and tempering. The heating temperature for quenching was 850 °C, which ensured maximum hardness and strength of the material. After soaking in the furnace the samples were quenched in oil, followed by low-temperature tempering at 200 °C for 1 hour.

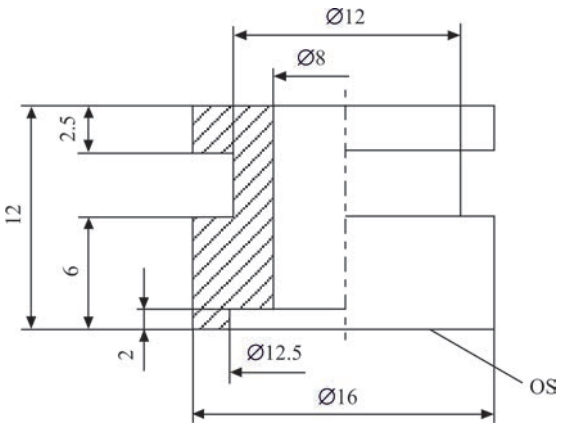

Figure 1. Test sample: bushing (40Kh); WS — working surface

The treatment of the samples was performed using a pulsed plasma generator (Figure 2), characterized by the capability of switching electric current through a partially ionized gas behind the detonation wave front. This enables generation of pulsed plasma with a frequency of 1–4 Hz and energy up to 7 kJ. PPT ensures rapid heating of the surface layer (10^{-3}–10^{-4} s heating time), followed by intensive cooling due to heat removal into the bulk of the product. The high heating and cooling rates (up to 10^7 K/s) promote the formation of fine-dispersed crystalline structures and high dislocation density. The principle of operation and technical parameters of the device are described in [12, 13].

Parameters of pulsed plasma treatment were as follows

Voltage of capacitor bank, kV	3.2
Capacitance of capacitor bank, μF	960
Inductance of discharge circuit, μH	30
Pulse repetition frequency, Hz	2
Distance to treated surface, mm	50
Effective plasma spot diameter on the surface, mm	10
Number of pulses per spot	5
Material of eroded electrode	W

For chemical etching of the microsections under investigation, a 4 % nitric acid (HNO_3) solution was used. Visual analysis of the samples was performed with a Versamet-2 optical microscope. The microstructure of the surface layers was examined using a Quanta 200 3D scanning electron microscope. Mic-

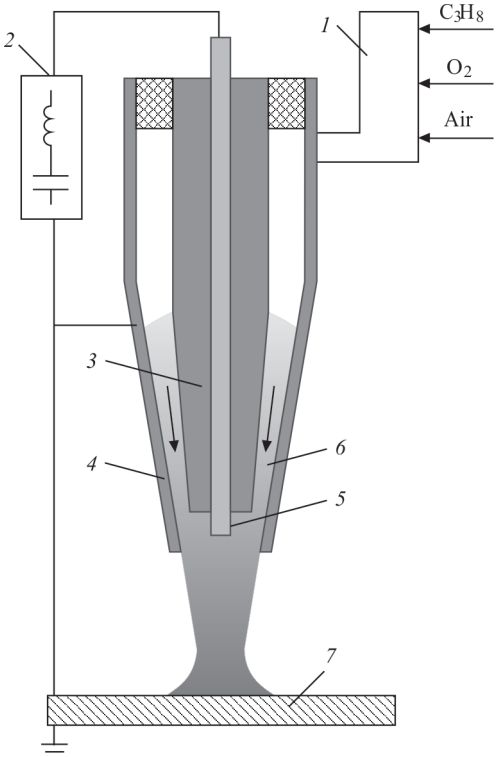

Figure 2. Pulsed plasmatron: *1* — detonation chamber; *2* — power supply; *3*, *4* — coaxial electrodes; *5* — eroded electrode; *6* — plasma; *7* — workpiece

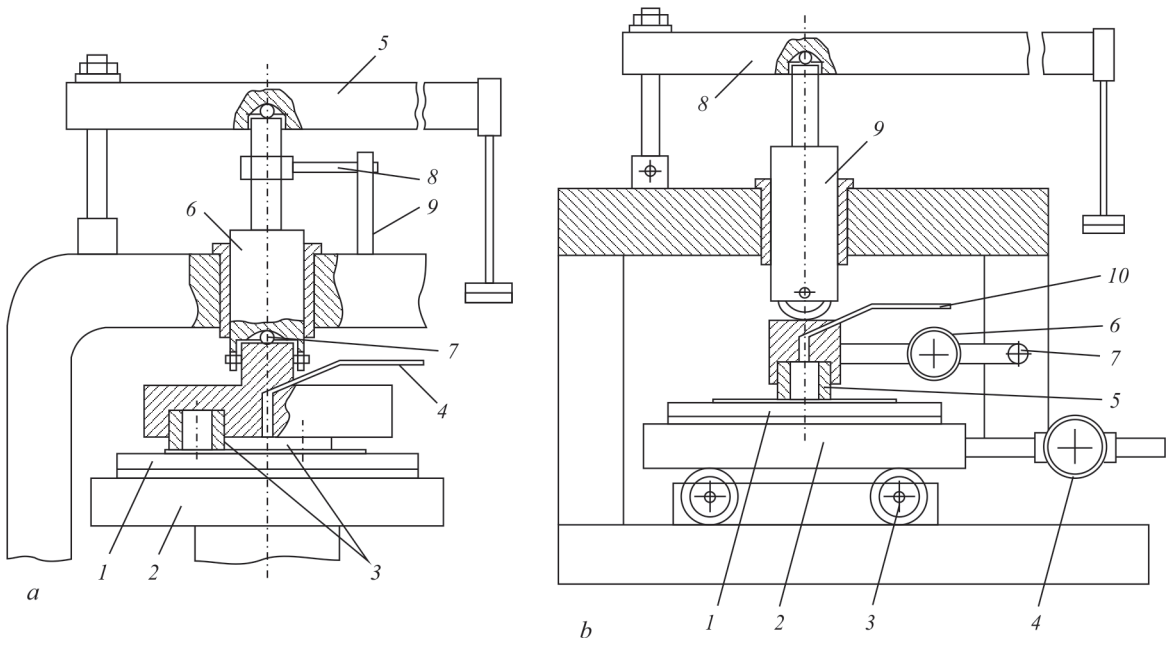

Figure 3. Schemes of the main units of friction machines: *a* — working unit of end friction machine; *b* — working unit of a reverse-friction machine

rohardness was measured in accordance with DSTU ISO 6507-1:2007 on an AFFRI DM8-B microhardness tester using the Vickers method with an indenter load of 50 g. Structural studies were carried out by X-ray diffraction analysis (filming in FeK_α radiation on a DRON-3M diffractometer).

The determination of tribotechnical characteristics of the parts was performed on end and reverse friction machines. Lubrication of the samples in the friction machines was carried out with I-50A type oil and RZh-3 water–oil emulsion, both supplied continuously to the friction zone.

The working unit of the end friction machine is shown in Figure 3, *a*. The moving sample — disk *1* — was mounted on table *2*, which rotates around the vertical axis, driven by the machine. Three stationary samples — bushings *3* — were fixed in a holder and pressed against rotating disk *1* by their end faces. Hose *4* connected to to the holder from a pump supplied lubricant into the friction zone. Lubricant was supplied from a 20 L tank by a pump with a capacity of 3 l/min, and returned to the tank by gravity after passing through the friction zone. The load on the holder with the samples was applied by lever *5* with weights, transmitted through fork *6*. A ball *7* was placed between the fork and the holder to ensure self-alignment of the holder with samples relative to the disk. During holder rotation caused by friction forces, the key of the holder engaged the slot of the fork and turned it. At the upper end of the fork, a rod *8* was rigidly fixed, pressing against a strain gauge *9*. For friction force measurement, the signal from the strain gauge was transmitted to and processed by a weight controller.

The working unit of the reverse friction machine is shown in Figure 3, *b*. The moving sample — disk *1* — was fixed on carriage *2* mounted on four rollers *3*. The carriage was connected via ring *4* to a slider driven by a crank-slider mechanism. The drive of the machine provided adjustable reciprocating motion with a stroke length of 20–70 mm and a double-stroke frequency of 95–320 per minute. The stationary sample — bushing *5* — was fixed in a hole of the holder, which was hingedly attached to shaft *7* through elastic ring *6*. Loading of the samples was achieved by lever *8* with interchangeable weights on its free end. The force was transmitted through rod *9* to the holder with the stationary sample. Lubricant was supplied from a special drop-feed system to the holder via hose *10* at a rate of 3 drops per minute. The friction force was determined using a strain gauge glued to elastic ring *6* and connected to the weight controller.

Wear of the stationary samples (bushings) was evaluated by measuring their mass loss with VLR-200 type analytical balances. Prior to weighing, the samples were washed twice in purified gasoline, then in acetone. After that, the samples were dried in a thermostat at 60 °C for 1 hour. The error in determining the sample mass using this procedure did not exceed 0.0002 g, with the average mass of one bushing being about 7 g.

RESEARCH RESULTS AND DISCUSSION

In 40Kh steel of the pearlitic class, martensite and retained austenite (5–8 vol.%) are formed as a result of quenching. The hardness of the steel after quenching reached 58 *HRC*. During low-temperature tempering (200 °C), tempered martensite is formed due

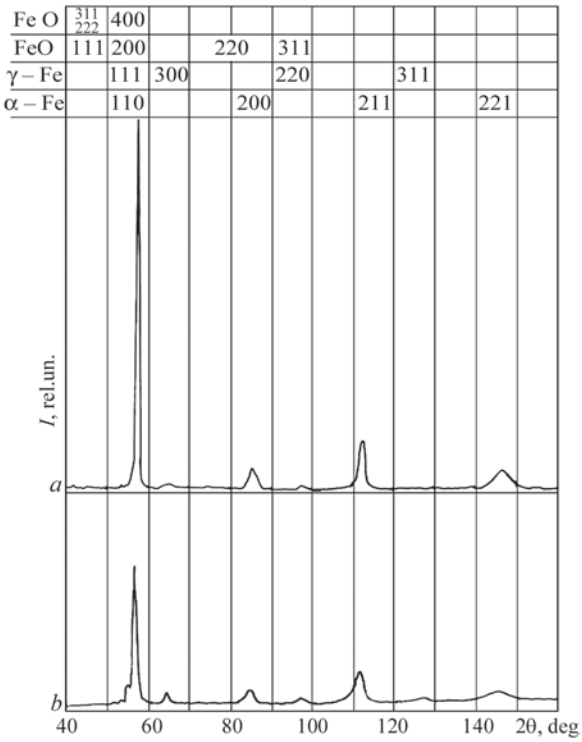

Figure 4. X-ray diffraction pattern of 40Kh steel: *a* — after heat treatment (quenching + tempering); *b* — after pulsed plasma treatment

to the transformation of retained austenite, as well as a decrease in the degree of tetragonality of martensite caused by the release of excess carbon from the α-solid solution. This leads to a slight decrease in hardness to 52 *HRC*.

A typical X-ray diffraction pattern of the sample surface after quenching and low-temperature tempering is shown in Figure 4, *a*. The phase composition of 40Kh steel is mainly tempered martensite with a small amount of retained austenite. PPT of the samples results in significant changes in the structural-phase composition in the surface layers (Figure 4, *b*).

The observed structural changes are consistent with the general concept of surface hardening using SDE (strongly non-equilibrium processes). After PPT, X-ray diffraction shows a broadening of the α-Fe lines and an increase in the intensity of the γ-Fe lines. The main contribution to line broadening comes from lattice defects caused by phase hardening during rapid quenching, as well as carbon inhomogeneity due to the high heating rate and the absence of soaking at high temperature. The broadening of the α-phase lines for this reason is associated with the heterogeneous tetragonality of martensite.

It should also be noted that despite the increase in austenite content (up to 15 vol.%) after PPT, the hardness of the surface layers (as will be shown below) increases due to phase hardening resulting from reversible α↔γ transformations under multiple pulsed impact. The diffraction pattern also shows oxide lines, the slight formation of which on the surface is related to the specifics of PPT. Firstly, oxygen is used as a component of the fuel and, accordingly, of the plasma-forming mixture. Secondly, the treatment is carried out in air.

When examining transverse microsections of the samples after PPT, the formation of a layered structure was revealed. It consists of a weakly etched band up to 35 μm thick (Figure 5) with fine-dispersed martensite of poorly pronounced optical structure, with an integral microhardness of *HV*50 = 8800–10200 MPa (Figure 6). The microhardness of this layer is 1.7 times higher than that of the base metal.

Below the hardened layer, a region up to 25 μm thick with a troostite–martensite structure is formed, where the integral microhardness decreases to *HV*50 ≈ 4500 MPa. In this case, the process of high-speed heating followed by cooling can be considered as a kind of tempering. Deeper, the hardness increases again to the hardness of tempered martensite of the base metal: *HV*50 = 5400–5700 MPa.

Tests of samples with and without PPT were carried out on a pin-on-disc friction machine at sliding speeds of 2, 3.5, and 5 m/s under loads of 0.5, 0.9, and 1.3 MPa. In each mode, the test duration was determined by wear of the samples and it lasted no less than 30 h. The results of tests with industrial oil I-50A and water-oil emulsion RZh-3 supplied into the friction zone are presented in the wear dynamics graphs (Figure 7).

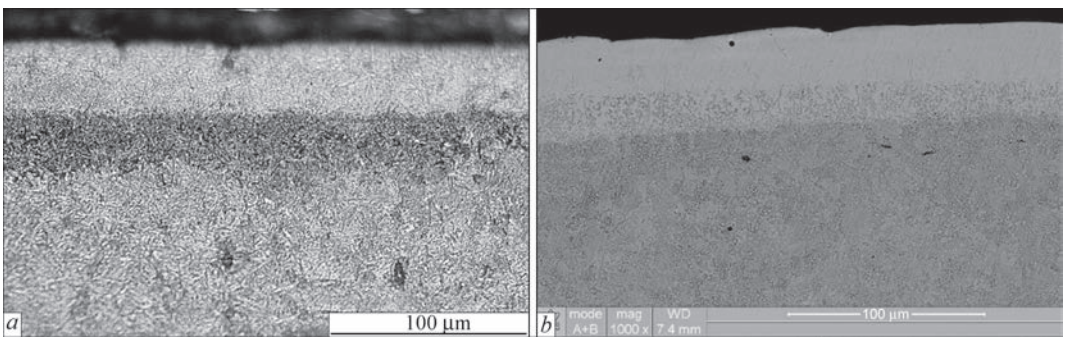

Figure 5. Microstructure of the surface layer of 40Kh steel after pulse-plasma treatment: *a* — image obtained with an optical microscope; *b* — image obtained with a scanning electron microscope

As expected, the use of industrial oil compared to water-oil emulsion significantly reduced the wear process. The minimum wear rate was observed in samples after PPT under all test conditions when using I-50A oil.

When lubricated with both I-50A oil and RZh-3 emulsion, at a constant sliding speed, wear of the samples increased with increasing load. Under fluid friction conditions, increasing the sliding speed contributed to wear reduction, even at higher loads (Figure 7).

Tests of samples on the reverse friction machine were carried out under drop lubrication with emulsion. Test modes were as follows: average sliding speeds were 0.15, 0.3, and 0.45 m/s; loads – 0.5, 0.9, and 1.3 MPa. The test results are presented in the wear dynamics graphs (Figure 8). The influence of sliding speed and load on wear intensity was similar to that observed on the end friction machine. Wear intensity increased with load growth and decreased with increasing sliding speed.

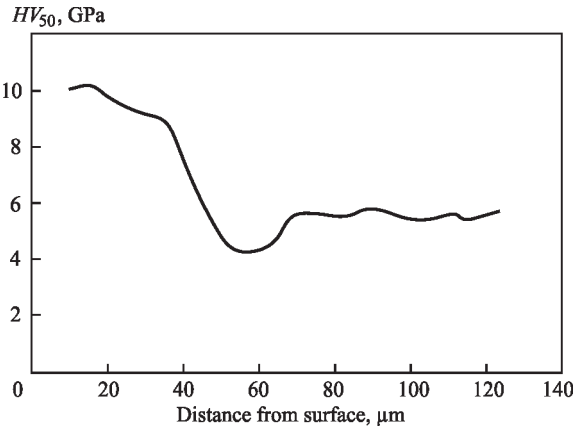

Figure 6. Change in integral microhardness in the surface layers of 40Kh steel after PPT

In most engineering calculations, the friction coefficient is assumed to be constant. However, under real conditions, especially under high loads, it may vary due to changes in contact area, phase transformations, wear, and other factors. Under fluid friction conditions, film thickness varies depending on load, which may also affect the friction coefficient. Studies

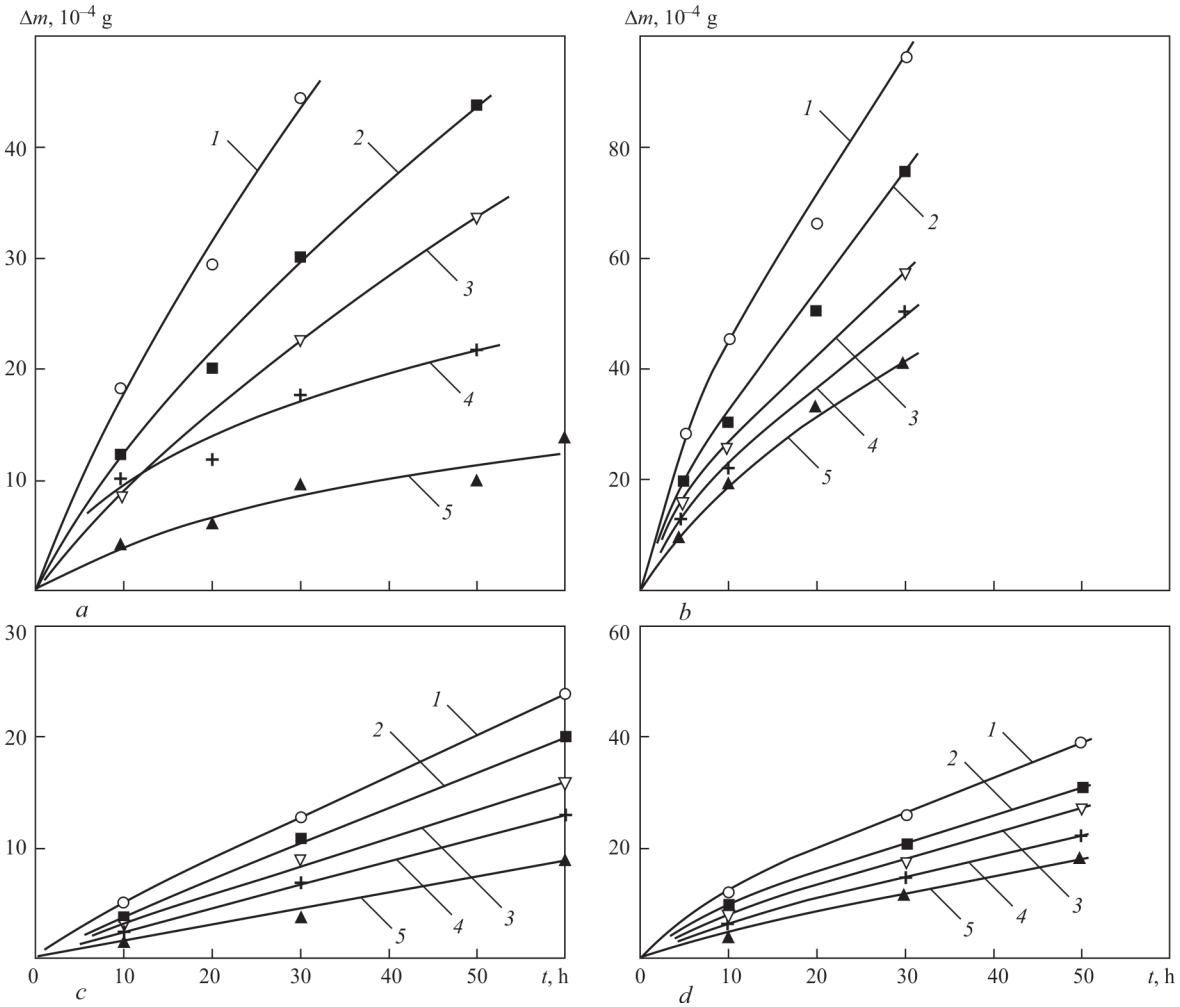

Figure 7. Wear dynamics of bushings on the end friction machine under lubrication: (*a*) with I-50A oil; (*b*) with RZh-3 emulsion; (*a*, *b*) — wear dynamics of bushings without PPT; (*c*, *d*) — wear dynamics of bushings after PPT; *1* — sliding speed 2.0 m/s, load 1.3 MPa; *2* — sliding speed 2.0 m/s, load 0.9 MPa; *3* — sliding speed 3.5 m/s, load 0.9 MPa; *4* — sliding speed 2.0 m/s, load 0.5 MPa; *5* — sliding speed 5.0 m/s, load 0.9 MPa

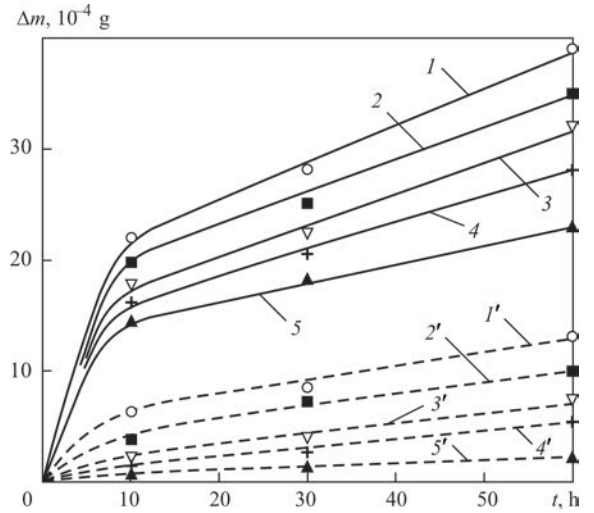

Figure 8. Wear dynamics of parts on a reverse friction machine with RZh-3 emulsion lubrication: a – wear dynamics of bushings; —— parts without PPT; – – – parts after PPT; *1*, *1′* — sliding speed 0.15 m/s, load 0.9 MPa; *2*, *2′* — sliding speed 0.30 m/s, load 0.9 MPa; *3*, *3′* — sliding speed 0.45 m/s, load 1.3 MPa; *4*, *4′* — sliding speed 0.45 m/s, load 0.9 MPa; *5*, *5′* — sliding speed 0.45 m/s, load 0.5 MPa

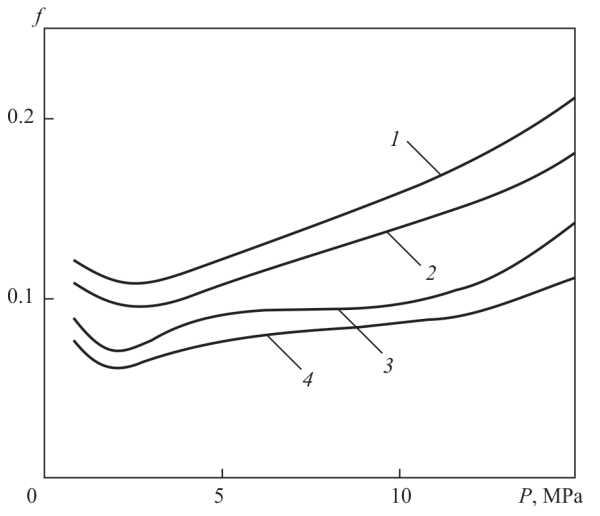

Figure 9. Dependence of the friction coefficient on the load during stepwise loading of samples on a reverse friction machine. Sliding speed 2 m/s. *1* — samples without PPT, friction with emulsion; *2* — samples after PPT, friction with emulsion; *3* — samples without PPT, friction with olive oil; *4* — samples after PPT, friction with olive oil

on both the end and reverse friction machines showed that the fluid friction coefficient changed little during testing. For samples without PPT on the end friction machine, depending on run-in time and test mode, the coefficient ranged from 0.07 to 0.12 and 0.1 to 0.13 when lubricated with I-50A and RZh-3, respectively. PPT reduced the friction coefficient by an average of 0.015. On the reverse friction machine under drop lubrication with emulsion and at the above test conditions, the friction coefficient for untreated and treated pairs was 0.12–0.16 and 0.1–0.14, respectively.

After prolonged testing of samples on the reverse friction machine at a speed of 2 m/s and a load of 1.3 MPa, burr tests were carried out on run-in samples (Figure 9). During the experiment, the load on the friction pair was stepwise increased by 1 MPa. At each stage, the pair operated for 10 minutes, after which the friction force was recorded, and the load was increased. A maximum load of 15 MPa was reached, but further load increase was not possible due to machine design limitations. As a result, burring could not be achieved.

CONCLUSIONS

1. Using the method of X-ray structural phase analysis, it was shown that after surface PPT of 40Kh steel samples, a hardened surface layer is formed, consisting of fine-dispersed martensite, retained austenite (14.8 vol.%), as well as a small amount of oxides. The increase in retained austenite at high cooling rates (up to 10^7 K/s) is associated with the suppression of high-temperature austenite decomposition during high-speed martensitic transformation.

2. Multiple thermal impact of pulse plasma enables the implementation of surface thermocyclic treatment, which contributes to the enhancement of phase hardening due to reversible α↔γ transformations, an increase in dislocation density, and grain refinement. As a result, a surface layer with a thickness of 35 μm is formed, exhibiting increased microhardness — *HV*50 = 8800–10200 MPa, which is 1.7 times higher than the microhardness of the base metal.

3. Analysis of the presented experiments shows that the tribological properties of the samples under fluid friction conditions are significantly improved as a result of their strengthening by the pulse plasma method. In particular, the strengthening provides a reduction in the wear rate of the samples by 1.2–3.7 times when lubricated with oil and by 1.4–4.3 times when lubricated with emulsion during tests on an end friction machine, and by 1.8–3 times on a reverse friction machine when lubricated with emulsion. In all cases, the strengthening ensures a reduction in the fluid friction coefficient by 0.01–0.02.

REFERENCES

1. Dinesh Babu, P., Balasubramanian, K.R., Buvanashekaran, G. (2011) Laser surface hardening: A review. *Inter. J. of Surface Sci. and Eng.*, 5(**2–3**), 131–151. DOI: https://doi.org/10.1504/IJSURFSE.2011.041398
2. Kwok, C.T., Man, H.C., Cheng, F.T., Lo, K.H. (2016) Developments in laser-based surface engineering processes: with particular reference to protection against cavitation erosion. *Surface and Coatings Technology*, **291**, 189–204. DOI: https://doi.org/10.1016/j.surfcoat.2016.02.019
3. Zou, J.X., Zhang, K.M., Hao, S.Z. et al. (2010) Mechanisms of hardening, wear and corrosion improvement of 316 L stainless steel by low energy high current pulsed electron beam surface treatment. *Thin Solid Films*, 519(**4**), 1404–1415. DOI: https://doi.org/10.1016/j.tsf.2010.09.022

4. Lashchenko, G.I. (2003) *Plasma hardening and spraying*. Kyiv, Ekotechnologiya [in Russian].
5. Maharjan, N., Zhou, W., Zhou, Y. et al. (2019) Comparative study of laser surface hardening of 50CrMo4 steel using continuous-wave laser and pulsed lasers with ms, ns, ps and fs pulse duration. *Surface and Coatings Technology*, **366**, 311–320. DOI: https://doi.org/10.1016/j.surfcoat.2019.03.036
6. Fedyukin, V.K., Smagorinsky, M.E. (1989) *Thermocyclic processing of metals and parts*. Leningrad, Mashinostroenie [in Russian].
7. Minko, L.Ya. (1970) *Generation and study of pulsed plasma flows*. Minsk, Nauka i Tekhnika [in Russian].
8. Chabak, Y.G., Fedun, V.I., Pastukhova, T.V. et al. (2017) Modification of steel surface by pulsed plasma heating. *Probl. At. Sci. Technol.*, **110**, 97–102. https://vant.kipt.kharkov.ua/ARTICLE/VANT_2017_4/article_2017_4_97.pdf
9. Yu, J., Zhang, L., Liu, K. et al. (2017) Effect of pulse detonation-plasma technology treatment on T8 steel microstructures. *J. of Materials Eng. and Performance*, **26**, 6198–6206. DOI: https://doi.org/10.1007/s11665-017-3067-y
10. Özbek, Y.Y. (2020) Surface properties of AISI 4140 steel modified by pulse plasma technique. *J. of Materials Research and Technology*, 9(**2**), 2176–2185. DOI: https://doi.org/10.1016/j.jmrt.2019.12.048
11. Tyurin, Yu.N., Kolisnichenko, O.V., Tsygankov, N.G. (2001) Pulse-plasma hardening of tools. *The Paton Welding J.*, **1**, 38–44.
12. Korzhyk, V., Tyurin, Y., Kolisnichenko, O. (2021) *Theory and practice of plasma-detonation technology of surface hardening metal products*. Kharkiv, PC Technology Center. DOI: https://doi.org/10.15587/978-617-7319-46-6
13. Tyurin, Y.N., Kolisnichenko, O.V. (2009) Plasma-detonation technology for modification of the surface layer of metal parts. *Open Surface Sci. J.*, **1**, 13–19. DOI: http://dx.doi.org/10.2174/1876531900901010013

ORCID
O.V. Kolisnichenko: 0000-0003-4507-9050,
V.M. Korzhyk: 0000-0001-9106-8593,
C. Senderowski: 0000-0002-0331-3702,
D.V. Strogonov: 0000-0003-4194-764X,
O.V. Hanushchak: 0000-0003-4392-6682,
O.S. Tereshchenko: 0009-0003-4021-0758

CONFLICT OF INTEREST
The Authors declare no conflict of interest

CORRESPONDING AUTHOR
O.V. Kolisnichenko
E.O. Paton Electric Welding Institute of the NASU
11 Kazymyr Malevych Str., 03150, Kyiv, Ukraine.
E-mail: okolis@i.ua

SUGGESTED CITATION
O.V. Kolisnichenko, V.M. Korzhyk, C. Senderowski, D.V. Strogonov, O.V. Hanushchak, O.S. Tereshchenko (2025) Influence of pulse plasma treatment on wear resistance of 40Kh steel surface layers. *The Paton Welding J.*, **9**, 39–45.
DOI: https://doi.org/10.37434/tpwj2025.09.05

JOURNAL HOME PAGE
https://patonpublishinghouse.com/eng/journals/tpwj

Received: 18.04.2025
Received in revised form: 19.06.2025
Accepted: 24.09.2025

DOI: https://doi.org/10.37434/tpwj2025.09.06

INDUSTRIAL TECHNOLOGIES OF DIRECT REDUCTION OF IRON FROM ORE RAW MATERIALS AND PROSPECTS FOR THE USE OF HYDROGEN IN REDUCTION PROCESSES

V.O. Shapovalov[1], **V.G. Mogilatenko**[2], **D.M. Zhyrov**[1], **V.R. Burnashev**[1]

[1]E.O. Paton Electric Welding Institute of the NASU
11 Kazymyr Malevych Str., 03150, Kyiv, Ukraine
[2]National Technical University of Ukraine "Igor Sikorsky Kyiv Polytechnic Institute"
37 Beresteiskyi Prosp., 03056, Kyiv, Ukraine

ABSTRACT

A significant reduction in carbon dioxide emissions in metallurgy can be achieved by using a mixture of carbon monoxide and hydrogen for iron reduction. Industrial technologies of direct reduction of iron from ore raw materials are considered. Reactions in reduction processes are analyzed. It is shown that at temperatures above 800 °C, hydrogen is a more effective reducing agent than carbon monoxide. Ways of improving the energy efficiency of existing technologies are demonstrated. It is shown that today the main technology of iron reduction from ore is reduction in shaft furnaces using a mixture of carbon monoxide and hydrogen. A generalized scheme of direct reduced iron production is presented. It is shown that in the production of direct reduced iron, the use of hydrogen makes it possible to halve carbon dioxide emissions compared to the use of natural gas, provided that electricity is generated from renewable sources or at nuclear power plants. It is concluded that a promising way to eliminate carbon emissions during the reduction of iron from ore or pellets is the use of plasma technologies.

KEYWORDS: direct reduced iron, hydrogen, shaft furnace, carbon dioxide emissions

INTRODUCTION

The production of pig iron and steel accounts for about 7 % of global carbon dioxide emissions due to the use of carbon for iron reduction from ore [1]. At present, the main route for obtaining steel from iron ore raw materials is iron reduction in blast furnaces with the production of pig iron, followed by its conversion into steel in basic oxygen converters. A significant reduction of carbon dioxide emissions in these processes cannot be achieved due to their technological schemes. In a blast furnace, layers of iron ore materials alternate with layers of coke, the main element of which is carbon. The coke layers ensure the gas permeability of the charge column, maintain the reducing potential of the gas phase in the upper part of the furnace, while coke carbon acts as a direct reducing agent in the lower part of the furnace and as the main source of energy for heating the charge and sustaining chemical reactions. In basic oxygen converters, the carbon in pig iron is oxidized until its concentration is reduced to the required level in steel. In this case, carbon combustion is the main source of energy for the process.

A significant reduction in carbon dioxide emissions in ferrous metallurgy can only be achieved by using a reducing agent that does not contain carbon. In terms of availability, cost, environmental friendliness, and reducing properties, the most appropriate option for iron reduction is the use of hydrogen.

There are many methods of hydrogen production [2]. Brown or black hydrogen is obtained by coal gasification using steam, gray hydrogen by steam reforming of natural gas (if carbon emissions are captured and stored, such hydrogen is called blue), and turquoise hydrogen by pyrolysis of natural gas with the formation of solid carbon. However, in all these methods, extraction of fossil fuels is required, and as a result, in addition to hydrogen, carbon or its oxides are formed, which must be utilized. A fundamentally different approach to hydrogen production is water electrolysis. In this case, if nuclear energy is used for electrolysis, the hydrogen is called pink; if electricity of mixed origin is used — yellow; and if electricity is derived exclusively from renewable sources it is called green. Green hydrogen is the most environmentally friendly, but also the most expensive. Therefore, it is important to ensure minimal hydrogen losses in the metallurgical process. The substitution of carbon with hydrogen as a reducing agent would allow for a significant reduction in carbon dioxide emissions in metallurgy, but it is clear that in this case a different technological scheme for producing steel from iron ore raw materials should be applied. It is also important to minimize energy consumption from both environmental and economic perspectives.

PROBLEM STATEMENT

Iron obtained through direct reduction technologies is called direct reduced iron (DRI). Its share in the

total volume of pig iron and DRI production increases every year. In 2021, it amounted to 7.2 %, in 2022 — 7.9 %, and in 2023 — 8.5 % [3]. In 2023, the volume of DRI production reached 136 mln t [4]. Of this amount, about 30 % was produced using technologies based on coal. Most often these are rotary kiln processes (for example, the SL/RN process) or rotary hearth furnaces. The majority of these facilities are located in India or South Africa, due to the developed coal industry in these countries. However, the use of coal carbon as a reducing agent makes it impossible to significantly reduce carbon dioxide emissions compared to the blast furnace process.

The most widespread group of industrial technologies for DRI production are shaft furnace reduction technologies: MIDREX (about 80 % of DRI production in shaft furnaces), Hyl/Energiron (17 %), Pered (3 %), Finmet, Circored, Fior, and others [4–8]. Today, the capacity of individual shaft furnaces can reach 2.5 mln t per year, for example, Tosyali Algérie and Algerian Qatari Steel (Algeria, MIDREX), Nucor Steel Louisiana (USA, Energiron).

In a lined shaft furnace, as in a blast furnace, there is a counterflow of iron-containing charge materials (lump iron ore or iron ore pellets), which descend under the action of gravity, and the ascending reducing gases, consisting mainly of hydrogen and carbon monoxide. The temperature in the technological process is regulated in such a way as to prevent softening and sticking of the charge materials. Therefore, there is no need for coke layers in the charge column, one of whose functions in the blast furnace is to ensure the gas permeability of the charge. In such processes, various reducing gases can be used: coke oven gas, products of coal gasification, natural gas or its conversion products, hydrogen. Most of these installations have been built in the Middle East, North Africa, and the Caribbean region, i.e., in areas rich in natural gas. Accordingly, the technological processes employed in existing installations are mostly designed for the use of natural gas or its conversion products. However, developers note the possibility of adjusting the technologies for the use of various gaseous reducing agents without carbon content.

One of the advantages of using gaseous reducing agents is their purity. Unlike coke and coal, they do not introduce additional impurities into DRI, such as sulfur, phosphorus, or arsenic. Thus, the content of harmful impurities in the product depends only on the purity of the iron ore raw materials. On the other hand, all the gangue contained in the iron ore materials remains in the DRI and enters the steelmaking furnaces, which leads to an increase in the amount of slag and energy consumption. Therefore, charge materials should contain as little gangue as possible. The optimal composition of iron ore or iron ore pellets is considered to be, % [5]: Fe = 67.0; $SiO_2 + Al_2O_3 = 3.0$; S = 0.008; P = 0.03; $TiO_2 = 0.15$.

There are few deposits of such rich iron ore. In particular, in commercial ores of the Kryvyi Rih basin, the average iron content ranges from 46.9 to 65.6 % [9]. This necessitates, as in the blast furnace process, the enrichment of relatively poor iron ores. For effective enrichment, the ore is ground, and after enrichment it is agglomerated to obtain sinter for the blast furnace or pellets for the blast furnace or for DRI production. Unlike the blast furnace, the production of direct reduced iron is possible in a fluidized bed of finely ground iron ore materials [8, 10, 11]. This is achieved through the use of gaseous reducing agents and limited heating of the iron ore raw materials. At present, such technologies have not yet found wide application, probably due to the prevention of particle sticking. However, they undoubtedly have prospects due to the elimination of the costs of agglomeration, which could significantly reduce the cost of DRI.

A shaft furnace for DRI production can be divided into zones of preliminary heating of the charge materials, reduction reactions, supply of reducing gases, and discharge of the metallized product [5, 6]. The main reduction reactions are the reactions of reducing iron from higher oxides to lower oxides and further to metallic iron by carbon monoxide and hydrogen:

$$3Fe_2O_3 + CO \rightarrow 2Fe_3O_4 + CO_2; \quad (1)$$

$$3Fe_2O_3 + H_2 \rightarrow 2Fe_3O_4 + H_2O; \quad (2)$$

$$Fe_3O_4 + CO \rightarrow 3FeO + CO_2; \quad (3)$$

$$Fe_3O_4 + H_2 \rightarrow 3FeO + H_2O; \quad (4)$$

$$FeO + CO \rightarrow Fe + CO_2; \quad (5)$$

$$FeO + H_2 \rightarrow Fe + H_2O. \quad (6)$$

Reactions (1) and (2) occur relatively easily in the upper part of the furnace. Reactions (3)–(6) require a significant excess of the reducing agent. Table 1 shows the composition of equilibrium gas mixtures for the reduction reactions depending on temperature [11].

From Table 1 it can be seen that reactions (5) and (6), i.e., the reactions of obtaining metallic iron, require the greatest excess of reducing agent. With increasing temperature, the reducing ability of hydrogen increases, while that of carbon monoxide decreases in reaction (5). At temperatures above 800 °C, hydrogen is a more effective reducing agent than carbon monoxide, and from a thermodynamic point of view, iron reduction is possible solely due to hydrogen. However, in any case, less than half of the reducing agent

Table 1. Composition of equilibrium gas mixtures for reduction reactions of H_2O/H_2 or CO_2/CO

Reaction	Temperature, °C						
	600	700	800	900	1000	1100	1200
(3)	55.2/44.8	64.8/35.2	71.9/28.1	77.6/22.4	82.2/17.8	85.9/14.1	88.9/11.1
(4)	30.1/69.9	54.2/45.8	71.3/28.7	82.3/17.7	89.0/11.0	92.7/7.3	95.2/4.8
(5)	47.2/52.8	40.0/60.0	34.7/65.3	31.5/68.5	28.4/71.6	26.2/73.8	24.3/75.7
(6)	23.9/76.1	29.9/70.1	34.0/66.0	38.1/61.9	41.1/58.9	42.6/57.4	44.5/55.5

can be used for the reduction of iron to metal under equilibrium conditions. In real industrial processes, the equilibrium is not achieved, and therefore an even greater excess of the reducing agent is required. Obviously, for the economic use of reducing agents, the off-gases from the shaft furnace must be cleaned and reused.

As a result of the reduction reactions, the degree of iron metallization in industrial technologies amounts to about 94 %.

The use of DRI is most appropriate for steelmaking in electric arc furnaces (EAF). On the one hand, the operation of an EAF does not lead to significant carbon dioxide emissions provided that electricity is generated from clean sources. On the other hand, DRI, unlike scrap metal, is characterized by a known and stable chemical composition and, given the purity of the iron ore raw materials, its use does not require significant means of steel refining.

Initially, the product of shaft furnace units consisted only of metallized pellets cooled prior to discharge — Cold Direct Reduction Iron (CDRI) [5]. However, they have a certain drawback — a tendency to oxidize and even self-ignite due to their developed surface area [11]. Therefore, for more convenient and safe transportation and storage, some plants later introduced the discharge of hot product into a roller press, where it is formed into dense pillow-shaped briquettes — Hot Briquetted Iron (HBI). In 2023, the share of HBI amounted to about 9 % of total DRI production [4].

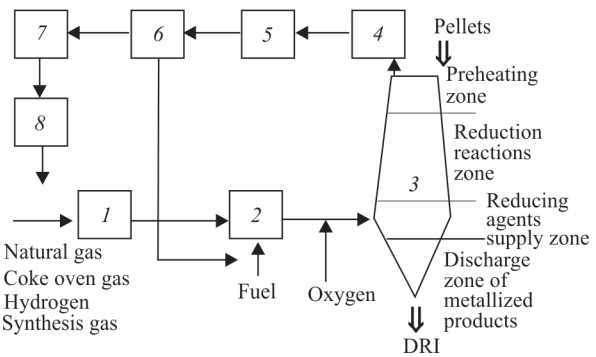

Figure 1. Technological scheme of DRI production: *1* — humidifier; *2* — heater; *3* — shaft furnace; *4* — heat exchanger; *5* — filtration system; *6* — water removal equipment; *7* — compressors; *8* — CO_2 removal equipment

Obviously, cooling DRI upon discharge from the shaft furnace and its subsequent reheating in the steelmaking furnace results in unnecessary energy, economic, and resource losses. Therefore, at some steel plants equipped with both shaft reduction furnaces and electric arc furnaces (EAF), the practice of discharging Hot Direct Reduction Iron (HDRI) has been implemented [5]. As a result, in addition to reducing the specific consumption of electricity, the productivity of steelmaking furnaces increases by up to 20 % [12]. This is because less energy and time are required to heat DRI to the melting temperature, thereby shortening the overall melting cycle. An empirical rule shows that electricity consumption decreases by approximately 20 kW·h/t of liquid steel for every 100 °C increase in DRI temperature. Thus, energy savings at DRI temperatures above 600 °C can reach up to 120 kW·h/t. Additional advantages, besides reduced electricity consumption, include lower electrode and EAF lining consumption and the possibility of using less powerful electrical equipment. Reduced energy consumption, in turn, leads to lower environmental pollution. In 2023, HDRI accounted for about 11 % of DRI production [4].

Depending on plant layout, different systems may be applied to transport HDRI to the steelmaking shop: conveyors (for distances up to 200 m), transport vessels (for distances above 100 m), or, if the distance is within 40 m, specialized systems such as HOTLINK [5]. The latter transfers HDRI at temperatures up to 700 °C directly into a neighboring EAF, enabled by positioning the MIDREX shaft furnace adjacent to the external wall of the steelmaking shop. HDRI is discharged hot into a storage bin and then fed directly into the EAF with minimal heat losses. HDRI transportation occurs by gravity. Due to the airtight design of the HOTLINK system, no re-oxidation of HDRI takes place. The HOTLINK system is designed to allow for the discharge of HBI or CDRI, in case the EAF does not require HDRI at a given moment, without stopping production [12].

A generalized flow diagram of DRI production is shown in the Figure 1.

Reducing gases (coke oven gas, coal gasification products, natural gas or its conversion products, hy-

Table 2. CO_2 emissions depending on the composition of the reducing gas mixture and the method of electricity generation, kg CO_2 per 1 t DRI [6]

Gas	100 % NG			50 % NG + 50 % H_2			20 % NG + 80 % H_2		
Source of electricity	Nuclear/ renewable	NG	Coal	Nuclear/ renewable	NG	Coal	Nuclear/ renewable	NG	Coal
Direct emissions during DRI production	495	–	–	287	–	–	200	–	–
Emissions associated with electricity use: in the reduction process in H_2 production	2 0	50 0	84 0	2 31	45 754	75 1262	2 46	42 1114	71 1864
Total emissions	495	545	579	320	1086	1624	248	1356	2135

drogen) are supplied to the humidifier *1*, where steam is used for the conversion of hydrocarbons. Subsequently, in the heater *2*, the gas mixture is heated to the required temperature. The heated gases are then introduced into the shaft furnace *3* for utilization in reduction processes. Oxygen may be added to the gas mixture prior to entering the shaft furnace in order to further increase its temperature.

The gases leaving the shaft furnace first pass through the heat exchanger *4* to ensure efficient utilization of thermal energy. They are then directed to the filtration system *5*, where the gases are cleaned primarily of iron ore dust. At the next stage *6*, cooling leads to the removal of water. Further, part of the gases can be used as fuel for heating the reducing gas mixture, while another portion, with the aid of compressors *7*, is sent to the CO_2 removal unit *8*. As a result, the gas mixture, now contains in predominantly reducing gases, and is reused in the reduction processes.

The presented scheme is generalized and may vary depending on the technological features of a specific plant. In particular, when hydrogen is used as the sole reducing agent, the stages of humidification *1* and CO_2 removal from the off-gas *8* are omitted.

As noted above, there are numerous methods for hydrogen production, with the most environmentally attractive option being the use of H_2 obtained via water electrolysis for reduction processes. However, when discussing environmental sustainability, CO_2 emissions associated with the production of electricity required for electrolysis must be considered. For example, the authors of study [6] estimated the approximate amount of CO_2 generated during DRI production under different natural gas (NG) to hydrogen ratios in the reducing gas mixture and under various electricity generation scenarios, making the following assumptions: the electricity consumption for producing 1 kg of hydrogen via electrolysis is 56 kW·h; CO_2 emissions per 1 kW·h of electricity amount to 20 g when generated from renewable sources or at nuclear power plants, 490 g when generated by natural gas combustion, and 820 g when generated by coal combustion.

The results of these investigations are presented in Table 2 [6].

Thus, the use of hydrogen as a reducing agent in shaft furnace–based DRI production allows a reduction of carbon dioxide emissions by approximately half, provided that the electricity required for hydrogen production is generated from nuclear or renewable sources — i.e., when using so-called pink or green hydrogen. On the other hand, reliance on electricity from fossil fuel–based power plants leads to a substantial increase in CO_2 emissions. It should also be emphasized that these calculations are valid for operations following the schematic process shown in the Figure 1, i.e., under the condition of reusing the gases exiting the shaft furnace.

It is evident that the reduction of CO_2 emissions in metallurgy is ensured by decreasing electricity consumption at any stage of steel production. As noted above, significant power savings can be achieved through the production of hot direct reduced iron (HDRI).

Another potential pathway for reducing CO_2 emissions in metallurgy is the application of plasma technologies. In particular, iron reduction in the molten state within plasma furnaces using reducing gases — including hydrogen [1, 13] and even the thermal decomposition of iron oxides [14] is considered feasible. The hot reducing gases discharged under such conditions from plasma furnaces could then be utilized either directly for iron reduction in shaft furnaces or for preheating the reducing gases fed into the shaft furnaces. However, these approaches still require further research, both in the field of plasma technologies proper and in the development of methods for their integration into shaft furnace–based iron reduction processes.

CONCLUSIONS

1. The primary group of technologies for direct iron reduction from ore feedstock is shaft furnace–based reduction processes. Hydrogen, as a component of reducing gases, actively participates in the reduction

reactions. From a thermodynamic perspective, even the use of pure hydrogen as an iron reducing agent is feasible in these technologies.

2. In DRI production, the use of hydrogen allows reducing CO_2 emissions by half compared with natural gas, provided that electricity is generated from renewable sources or at nuclear power plants.

3. The application of plasma-based hydrogen reduction technologies represents a promising pathway for decreasing CO_2 emissions in metallurgy. However, further research is required, both regarding the technological features of the process and the design aspects of shaft furnaces.

REFERENCES

1. Isnaldi, R. Souza Filho, Hauke Springer et al. (2022) *Green steel at its crossroads: Hybrid hydrogen-based reduction of iron ores*. https://arxiv.org/ftp/arxiv/papers/2201/2201.13356.pdf
2. Giovannini, S. (2020) *50 shades of (grey and blue and green) hydrogen puzzled by all the colours and argon? This article is for you*. Energy Cities. https://energy-cities.eu
3. Kolisnichenko, V. (2023) Global production of cast iron grew by 1.1 % in 2023. https://gmk.center/ua/news/globalne-virobnictvo-chavunu-u-2023-roci-zroslo-na-1-1-r-r/
4. (2023) *World Direct Reduction Statistics*. https://www.midrex.com/wp-content/uploads/MidrexSTATSBook2023.pdf
5. *The MIDREX Process — The world's most reliable and productive Direct Reduction Technology*. https://www.midrex.com/wp-content/uploads/MIdrex_Process_Brochure_4-12-18.pdf
6. Pauluzzi, D., Giraldo, A.H., Zugliano, A. et al. (2021) *CFD Study of an Energiron Reactor Fed With Different Concentrations of Hydrogen*. AISTech Iron & Steel Technology. https://www.energiron.com/wp-content/uploads/2021/09/MARCH-2021_AIST-IRON-STEEL-TECHNOLOGY.pdf
7. Pauluzzi, D., Martinis, A. Sustainable decrease of CO_2 *Emissions in the Steelmaking Industry by Means of the Fine Ore Direct Reduction Circored Energiron Direct Reduction Technology*. https://www.researchgate.net/publication/329059091_SUSTAINABLE_DECREASE_OF_CO2_EMISSIONS_IN_THE_STEELMAKING_INDUSTRY_BY_MEANS_OF_THE_ENERGIRON_DIRECT_REDUCTION_TECHNOLOGY
8. https://www.metso.com/globalassets/pdfs-and-other-downloads/circored---fine-ore-direct-reduction.pdf
9. Pochtariov, O.V. (2024*) Improvement of technological means of quality control of iron ore raw materials in underground mining*: Syn. of Thesis for PhD. Kryvorizh. Nats. Un-t. Kryvyi Rig.
10. Bondarenko, B.I., Shapovalov, V.A., Garmash, N.I. (2003) *Theory and technology of coke-free metallurgy.* Kyiv, Naukova Dumka
11. Gubin, G.V., Piven, V.O. (2010) *Modern commercial methods of iron coke-free metallurgy.* Kryvyi Rig.
12. Hotlink System. Benefits of Charging Hot Dri (HDRI). https://www.midrex.com/wp-content/uploads/Hot_Transport_-_HOTLINK.pdf
13. Zhyrov, D.M. (2011) *Peculiarities of the plasma-arc liquid-phase reduction of iron with gases*: Syn. of Thesis for Cand. of Tech. Sci. Degree. Kyiv, PWI.
14. Mogylatenko, V.G., Shapovalov, V.O., Biktagirov, F.K., Kozin, R.V. (2023) Thermal decomposition of hematite pellets during plasma-arc smelting in argon atmosphere. In: *Proc. of XVth Inter. Sci.-Tech. Conf. on New Materials and Technologies in Mechanical Engineering, 27–28 April 2023.* Kyiv, KPI, 23–29.
15. https://foundry.kpi.ua/wp-content/uploads/2023/06/conferenziya_2023.pdf

ORCID

V.O. Shapovalov: 0000-0003-1339-3088,
V.G. Mogilatenko: 0000-0002-6550-2058,
D.M. Zhyrov: 0000-0002-9435-8075,
V.R. Burnashev: 0000-0001-6807-3810

CONFLICT OF INTEREST

The Authors declare no conflict of interest

CORRESPONDING AUTHOR

V.G. Mogilatenko
National Technical University of Ukraine
"Igor Sikorsky Kyiv Polytechnic Institute"
37 Beresteiskyi Prosp., 03056, Kyiv, Ukraine.
E-mail: vmogilatenko@gmail.com

SUGGESTED CITATION

V.O. Shapovalov, V.G. Mogilatenko, D.M. Zhyrov, V.R. Burnashev (2025) Industrial technologies of direct reduction of iron from ore raw materials and prospects for the use of hydrogen in reduction processes. *The Paton Welding J.*, **9**, 46–50.
DOI: https://doi.org/10.37434/tpwj2025.09.06

JOURNAL HOME PAGE

https://patonpublishinghouse.com/eng/journals/tpwj

Received: 26.05.2025
Received in revised form: 05.08.2025
Accepted: 17.09.2025